

THE EVOLUTION OF BRIGHTEST CLUSTER AND DWARF GALAXIES
USING INTEGRAL FIELD UNIT SPECTROSCOPY

A Dissertation

by

JIMMY

Submitted to the Office of Graduate and Professional Studies of
Texas A&M University
in partial fulfillment of the requirements for the degree of

DOCTOR OF PHILOSOPHY

Chair of Committee,	Kim-Vy H. Tran
Committee Members,	Casey J. Papovich
	Darren L. DePoy
	William J. Murphy
Head of Department,	George Welch

May 2016

Major Subject: Physics

Copyright 2016 Jimmy

ABSTRACT

The study of galaxy formation and evolution utilizes empirical scaling relations as a tool to better understand complex physical processes that occur below the resolution of observations. New observations of galaxy populations can provide tests of the range of validity for known scaling relations. We test the following scaling relations using IFU spectroscopy of galaxies at opposite ends of the stellar-mass spectrum.

Brightest cluster galaxies undergo, on average, more mergers than a typical early-type galaxy. They also lie at the center of their host cluster’s gravitational potential well, meaning there is no preferred alignment for mergers. As such, we would expect to find that BCGs should have preferentially lower angular momentum when compared to a population of early-type galaxies. We have spatially mapped the kinematic properties of 10 nearby brightest cluster galaxies (BCGs) in the mass range $10^{10.5} M_{\odot} < M_{dyn} < 10^{11.9} M_{\odot}$. We find that 30% (3/10) of the BCGs are fast rotators as defined by the ATLAS^{3D} criteria. This is significantly lower than the ATLAS^{3D} population as a whole, however our sample is biased towards higher dynamical-mass galaxies. When controlling for dynamical-mass, we find that above $M_{dyn} \sim 10^{11.5} M_{\odot}$, both samples show the same ratio of slow rotators. This suggests that the relation between galaxy angular momentum and dynamical mass is independent of the number of mergers a galaxy has undergone.

Dwarf irregular galaxies are the local universe analogs of the young high-redshift galaxies that eventually merge to form BCGs. The mass-metallicity scaling relation (MZR) says that galaxies with higher stellar-mass have preferentially higher gas metallicity. Mergers have been suggested as a potential cause of the scatter in the

mass-metallicity relation as pristine gas is driven into a galaxy, diluting the metal content. Two different three-dimensional extensions of MZR, as a function of either HI-gas mass (FMR_{HI}) or star formation rate (FMR_{SFR}), have been suggested to account for the scatter in the MZR. We use our IFU data to study the FMR_{SFR} and FMR_{HI} across the stellar mass range $10^{6.6}$ to $10^{8.8} \text{ M}_{\odot}$. The lowest 1σ scatter of binned means is for the FMR_{HI} (0.01 dex), significantly lower than that of the MZR (0.05 dex). This leads us to conclude that inflows of pristine HI-gas is the best candidate for a physically motivated fundamental metallicity relation.

Using the same sample of dwarf irregular galaxies, we investigate the relationship between $\text{H}\alpha$ luminosity surface density ($\Sigma_{\text{H}\alpha}$) and Balmer optical depth (τ_{b}) using the added spatial information provided by IFU spectroscopy. We find a positive correlation between $\Sigma_{\text{H}\alpha}$ and τ_{b} in 8 of 11 galaxies. Our spaxels have physical scales ranging from 30 to 80 pc, demonstrating that the correlation between these two variables continues to hold down to spatial scales as low as 30 pc. The positive correlation between $\Sigma_{\text{H}\alpha}$ and τ_{b} is consistent even within the lowest mass galaxies.

Although brightest cluster galaxies are often considered special populations, we find that they are generally consistent with scaling relations derived for intermediate-mass early-type galaxies. Similarly dwarf irregular galaxies that span a stellar mass range $10^{6.6} - 10^{8.8} \text{ M}_{\odot}$ are consistent with the mass-metallicity relation derived for star forming galaxies in the stellar mass range $10^8 - 10^{11} \text{ M}_{\odot}$. From this we can conclude that these scaling relations are based on fundamental physics that act across an extraordinary range of galaxy mass scales.

DEDICATION

To Mom and Dad, for loving me into the toughest guy you ever met.

“You can’t get that tough without love.

Not ‘tough love.’ Gentle, pure love. Pure love makes tough. Unconditional love from Mommy just like it’s supposed to be. And unconditional love from Daddy. Daddy who didn’t get the memo that his love was supposed to be different. Unconditional love from both Mommy and Daddy, that’ll make you tough. That’ll make you twelve feet tall and bulletproof.”

– Penn Jillette “Sock”

ACKNOWLEDGEMENTS

My deepest gratitude to my graduate advisor Kim-Vy Tran for helping me throughout my graduate student career. I couldn't have done it without your advice and support. Also, thank you to my committee members Casey Papovich, Darren DePoy, and William Murphy for their assistance and advice throughout graduate school.

Thank you to the people that have collaborated with me throughout the years on my various scholarly works: Karl Gebhardt, Anja von der Linden, Davide Martizzi, Sarah Brough, Paola Oliva-Altamirano, Rob Sharp, Warrick Couch, Amèlie Saintonge, and Gioacchino Accurso for their valuable insight and assistance.

A special thank you to Ryan Quadri and Nick Suntzeff, both of whom I have often turned to for guidance whenever I had a particularly troubling issue to deal with, both professionally and personally. Similarly thank you to Adam Tomczak, Brett Salmon, and Leo Alcorn for their assistance reading over drafts of this dissertation.

I'd also like to thank my family, Mom, Dad, Veronica, Mike, Beth, Brent, Kathy, and both Jims for their support and more importantly understanding as I made my way through grad school in a far off and distant land.

I would like to thank the VIMOS team for their pipeline, and GitHub for hosting the code used to reduce my data. I would also like to thank Louis Abramson for assistance with GALFIT and Source Extractor. I would like to thank our referee on my first paper, Eric Emsellem, for his excellent feedback, which helped to clarify our narrative as well as our results.

The data reduction performed to obtain our results was done on the Brazos

supercomputing cluster at Texas A&M university. I would especially like to thank the Mitchell family for their continuing support and in particular the late George P. Mitchell whose vision and commitment to science and astronomy leaves a lasting legacy.

Funding for SDSS-III has been provided by the Alfred P. Sloan Foundation, the Participating Institutions, the National Science Foundation, and the U.S. Department of Energy Office of Science. The SDSS-III web site is <http://www.sdss3.org/>.

SDSS-III is managed by the Astrophysical Research Consortium for the Participating Institutions of the SDSS-III Collaboration including the University of Arizona, the Brazilian Participation Group, Brookhaven National Laboratory, Carnegie Mellon University, University of Florida, the French Participation Group, the German Participation Group, Harvard University, the Instituto de Astrofisica de Canarias, the Michigan State/Notre Dame/JINA Participation Group, Johns Hopkins University, Lawrence Berkeley National Laboratory, Max Planck Institute for Astrophysics, Max Planck Institute for Extraterrestrial Physics, New Mexico State University, New York University, Ohio State University, Pennsylvania State University, University of Portsmouth, Princeton University, the Spanish Participation Group, University of Tokyo, University of Utah, Vanderbilt University, University of Virginia, University of Washington, and Yale University.

I am very grateful to the entire ALFALFA team for the extensive work involved in observing, processing, flagging, and cataloguing the ALFALFA data, which this paper is based on. I also wish to acknowledge the important contributions of Martha Haynes, Riccardo Giovanelli, and Marco Scodeggio in devising the VIMOS-IFU follow-up project based on ALFALFA-detected dwarf galaxies.

I must also thank my fellow graduate students Brett, Mike, Ryan, Adam, Steven, Ben, Leo, Andrew, Ting, Dan, Yi, Peter, Kaitlyn, Vince, Nancy, Wenlong, and Heath

for the friendship and distractions they have provided me over all these years, I hope we keep in touch, and I wish you all the best as you complete your graduate student careers. Also thank you to Dustin Lorshbough for helping push me along, keeping me on track and in good spirits.

To anyone that I might have forgotten, my apologies, I guess I owe you a beer.

NOMENCLATURE

"	Arcseconds
Å	Angstroms
Λ CDM	Cold Dark Matter with Dark Energy
Ω_Λ	Density of Dark Energy
Ω_M	Density of Matter
2D	Two Dimensional
AGC	Arecibo General Catalog
AGN	Active Galactic Nucleus
ALFALFA	The Arecibo Legacy Fast ALFA Survey
AoN	Amplitude over Noise
BCG	Brightest Cluster Galaxy
CCD	Charge-Coupled Device
D02	Denicoló et al. 2002
DBSP	Double Spectrograph
D_L	Luminosity Distance
Dec	Declination
ESO	European Southern Observatory
FP	Fundamental Plane
FML	Fundamental Metallicity-Luminosity
FML_{SFR}	Fundamental Metallicity-Luminosity Relation as a Function of Star Formation Rate
FML_{HI}	Fundamental Metallicity-Luminosity Relation as a Function of HI-gas Mass

FMR	Fundamental Metallicity Relation
FMR _{SFR}	Fundamental Mass-Metallicity Relation as a Function of Star Formation Rate
FMR _{HI}	Fundamental Mass-Metallicity Relation as a Function of HI-gas Mass
FR	Fast Rotator
FWHM	Full Width at Half Maximum
G	Gini Coefficient
GANDALF	Gas AND Absorption Line Fitting algorithm
Gyrs	Gigayears
H ₀	Hubble Constant
HI	Neutral Atomic Hydrogen
HII	Ionized Atomic Hydrogen
HR	High Resolution
IDL	Interactive Data Language
IFU	Integral Field Unit
IGM	Intergalactic Medium
IMF	Initial Mass Function
ISM	Interstellar Medium
K	Kelvin
KPNO	Kitt Peak National Observatory
LR	Low Resolution
LZR	Luminosity-Metallicity Relation
LMC	Large Magellanic Cloud
M _☉	Solar Mass
M _*	Stellar Mass

M_{20}	2nd Moment of Brightness
M_{HI}	HI-Gas Mass
M_{dyn}	Dynamical Mass
M/L	Mass-to-Light Ratio
MAD	Median Absolute Deviation
mag	Magnitude
M_B	Absolute B-Band Magnitude
m_B	Apparent B-Band Magnitude
MCMC	Markov Chain Monte Carlo
MPA-JHU	Max Planck Institute for Astrophysics - Johns Hopkins University
Mpc	Megaparsec
MMT	Multiple Mirror Telescope
MILES	Medium-resolution Isaac Newton Telescope Library of Empirical Spectra
Myrs	Megayears
MZR	Mass-Metallicity Relation
N2	$H\alpha$ and [NII] Based Oxygen Abundance Estimation
NGC	New General Catalogue
O3N2	$H\alpha$, $H\beta$, [OIII] and [NII] Based Oxygen Abundance Estimation
pc	parsec
PP04	Pettini & Pagel 2004
pPXF	Penalized Pixel-Fitting
PSF	Point Spread Function
R23	$H\beta$, [OIII] and [OII] Based Oxygen Abundance Estimation
RA	Right Ascension
RSS	Row Stacked Spectra

S/N	Signal/Noise
SAMI	Sydney-AAO Multi-object Integral-field spectrograph
SAURON	Spectrographic Areal Unit for Research on Optical Nebulae
SDSS	Sloan Digital Sky Survey
SED	Spectral Energy Distribution
SExtractor	Source Extractor
SFR	Star Formation Rate
SHIELD	Survey of HI in Extremely Low-mass Dwarfs
SMC	Small Magellanic Cloud
SR	Slow Rotator
VIMOS	Visible Multiobject Spectrograph
VLT	Very Large Telescope
z	Redshift

TABLE OF CONTENTS

	Page
ABSTRACT	ii
DEDICATION	iv
ACKNOWLEDGEMENTS	v
NOMENCLATURE	viii
TABLE OF CONTENTS	xii
LIST OF FIGURES	xv
LIST OF TABLES	xvii
1. INTRODUCTION	1
1.1 The Curious Behavior of Baryons in Galaxies	1
1.2 A Brief Introduction to IFU Spectroscopy	3
1.3 Brightest Cluster Galaxy Angular Momentum and Mass	6
1.4 The Mass-Metallicity Relation	8
1.5 The H α -Balmer Optical Depth Relation	9
2. ANGULAR MOMENTA, DYNAMICAL MASSES, AND MERGERS OF BRIGHTEST CLUSTER GALAXIES	12
2.1 Synopsis	12
2.2 Background Information	13
2.2.1 Merger History of Brightest Cluster Galaxies	14
2.2.2 Signatures of Recent Merging in BCGs at $z < 0.1$	16
2.3 Observations	18
2.3.1 Spectroscopic Measurements	18
2.3.2 Photometric Measurements	23
2.4 Results	25
2.4.1 Kinematic Maps	25
2.4.2 Angular Momenta (λ_R)	29
2.4.3 Dynamical Mass	31
2.4.4 Photometry	36

2.4.5	Boundedness	39
2.5	Discussion	40
2.5.1	Mergers and Rotation	40
2.5.2	Companion Rotation	44
2.5.3	Angular Momentum and Dynamical Mass	44
2.5.4	Cluster Rotation	47
2.6	Conclusion	47
3.	THE GAS PHASE MASS METALLICITY RELATION FOR DWARF GALAXIES: DEPENDENCE ON STAR FORMATION RATE AND HI-GAS MASS	51
3.1	Synopsis	51
3.2	Introduction	52
3.3	Sample	56
3.3.1	Spectroscopic Observations	56
3.3.2	Photometric Observations	62
3.3.3	Stellar Masses	63
3.3.4	ALFALFA/SDSS Sample Selection	66
3.3.5	Comparison Data	67
3.4	Analysis	68
3.4.1	Oxygen Abundance	68
3.4.2	Luminosity	70
3.4.3	Star Formation Rates	71
3.4.4	ALFALFA/SDSS Analysis	74
3.5	Results	79
3.5.1	Mass-Metallicity Relation and Luminosity-Metallicity Relation	79
3.5.2	MZR/LZR with SFR and HI-gas Mass Dependence	81
3.5.3	Fundamental Metallicity Relations	84
3.6	Discussion	94
3.6.1	FMR_{HI}	95
3.6.2	FMR_{SFR}	96
3.6.3	FML_{HI}	97
3.6.4	FML_{SFR}	97
3.6.5	$H\alpha$ Line Flux Limitations	97
3.7	Conclusion	99
4.	SPATIAL CORRELATION BETWEEN DUST AND $H\alpha$ EMISSION IN DWARF IRREGULAR GALAXIES	101
4.1	Synopsis	101
4.2	Introduction	101
4.3	Observations	105

4.3.1	IFU Spectroscopy	105
4.3.2	Data Reduction	106
4.3.3	Artificial Galaxy	109
4.4	Results	110
4.4.1	Balmer Line Luminosities	112
4.4.2	Balmer Optical Depth	115
4.4.3	Correlation Between $H\alpha$ and τ_b	120
4.5	Discussion	122
4.5.1	Increasing Attenuation with Increasing $H\alpha$ Luminosity	122
4.5.2	Negative τ_b Values	125
4.6	Conclusion	127
5.	SUMMARY	130
5.1	Brightest Cluster Galaxy Mergers and Kinematics	132
5.2	Dwarf Galaxy Fundamental Metallicity Relation	133
5.3	Dust Distribution within Dwarf Irregular Galaxies	134
5.4	Future Prospects	135
5.4.1	Angular Momentum of Clusters Vs. BCGs	135
5.4.2	Upper Mass Limit to Fast Rotating Galaxies	136
5.4.3	Dwarf Galaxy Metallicity Gradients	136
	REFERENCES	138
	APPENDIX A. ABILITY TO RECOVER METALLICITY	158
	APPENDIX B. COMPARISON BETWEEN N2 AND O3N2 BASED CALI- BRATIONS	161
	APPENDIX C. SFR AND HI MASS MEAN BINS	169
	APPENDIX D. TABLE OF FLUX VALUES	172

LIST OF FIGURES

FIGURE	Page
1.1 Mass-Metallicity Relation	2
1.2 Fast Rotator and Slow Rotator Demarcation	4
2.1 Example pPXF Fit to Spectrum	22
2.2 IFU Velocity Maps of BCGs Without Companions	26
2.3 IFU Velocity Maps of BCGs With Companions	27
2.4 IFU Velocity Dispersion Maps of BCGs and Companions	28
2.5 Angular Momentum Profile of BCGs	29
2.6 Angular Momentum vs. Ellipticity at the Effective Radius	32
2.7 Angular Momentum vs. Dynamical Mass	33
2.8 Single Component de Vaucouleurs Fits to BCG Photometry	37
2.9 Merger Status and Angular Momentum at the Effective Radius	41
3.1 SDSS Images of Dwarf Galaxies	55
3.2 Example Spectra Showing Blending of Emission Lines	60
3.3 Spatial Map of H α Emission and Segmentation Map	72
3.4 Comparison Between IFU and SDSS Measurements	75
3.5 Mass-Metallicity and Luminosity-Metallicity Relations	80
3.6 Mass-Metallicity Relation Binned by HI-Mass and SFR	82
3.7 Luminosity-Metallicity Relation Binned by HI-Mass and SFR	83
3.8 Lowest Scatter in FMR_{SFR} and FMR_{HI} Relations	86

3.9	FMR _{HI} and FMR _{SFR} Relations	89
3.10	Lowest Scatter in FML _{SFR} and FML _{HI} Relations	91
3.11	FML _{HI} and FML _{SFR} Relations	93
3.12	FMR _{SFR} With IFU Observed Galaxies in Combined Bin	98
4.1	Example Result of Python-based Gaussian Fitting Routines	108
4.2	Spatial Map of H α Luminosity	113
4.3	Spatial Map of H β Luminosity	114
4.4	Spatial Map of Balmer Optical Depth	116
4.5	Integrated Star Formation Rate vs. Gini Coefficient	117
4.6	$\Sigma_{\text{H}\alpha}$ vs. τ_{b} for Individual Galaxies	118
4.7	$\Sigma_{\text{H}\alpha}$ vs. τ_{b} All Spaxels Fit	119
A.1	Example H α emission of a Simulated Galaxy	159
A.2	Details of Python Based Gaussian Fitting Routines	160
B.1	Ability to Recover Metallicities	162
B.2	Figure 3.5 Using the PP04 O3N2 Oxygen Abundance Calibration . . .	164
B.3	Figure 3.6 Using the PP04 O3N2 Oxygen Abundance Calibration . . .	165
B.4	Figure 3.7 Using the PP04 O3N2 Oxygen Abundance Calibration . . .	166
B.5	Figure 3.9 Using the PP04 O3N2 Oxygen Abundance Calibration . . .	167
B.6	Figure 3.11 Using the PP04 O3N2 Oxygen Abundance Calibration . . .	168

LIST OF TABLES

TABLE	Page
2.1 Observing Properties of BCGs and Companions	19
2.2 Kinematic Properties of BCGs and Companions	35
2.3 Photometric Properties of BCGs and Companions	38
3.1 Integrated Properties of Dwarf Galaxies	65
3.2 Linear Fits to Dwarf Galaxy IFU SFR & HI-Mass Bins	85
3.3 Best Fitting Fundamental Relation Parameters	94
4.1 Distance, Mass, and Metallicity Properties of Dwarf Galaxies	111
4.2 Correlation Between $\Sigma_{\text{H}\alpha}$ and τ_{b} in Dwarf Galaxies	119
C.1 ALFALFA/SDSS FMR Binned Mean Metallicity Values	170
C.2 ALFALFA/SDSS FML Binned Mean Metallicity Values	171
D.1 Observed Emission Line Fluxes of Dwarf Galaxies	172

1. INTRODUCTION

1.1 The Curious Behavior of Baryons in Galaxies

The study of galaxy formation and evolution can be thought of as the study of the behavior of the smallest particles on the largest scales. The formation and evolution of galaxies is dependent upon a variety of physical processes governing the behavior of baryons. The influences upon baryons include radiative transfer, morphology, environment, gravity, hydrodynamics, metallicity, mass of the host dark matter halo and feedback from stellar winds, supernovae, and active galactic nuclei. If we wish to understand how galaxies form and evolve, we must understand the movement and interactions of baryons within galaxies.

The size and sheer number of individual baryons within a galaxy makes it impossible to study or even computationally model each individual baryon. Therefore, we often rely upon empirical scaling relations which are the observable result of a combination of underlying physical processes. A well known example would be the mass-metallicity relation (Lequeux et al., 1979). In the simplest terms, the mass-metallicity relation states that as the stellar mass of a galaxy increases, the abundance of heavy elements in the interstellar medium (ISM) will also increase (Figure 1.1). Underlying this observed relation are the complexities inherent in the formation of stars and heavy elements (e.g. gas cooling, nuclear fusion, fluid motion, etc.). Absent of interpretation, these scaling laws alone are of limited value, however by comparing them to physical models and simulations, we can begin to understand the basic underlying physics that are driving the observed phenomena. Alternatively, scaling laws provide much needed checks on theoretical models which are much more probable if they properly reproduce known scaling relations.

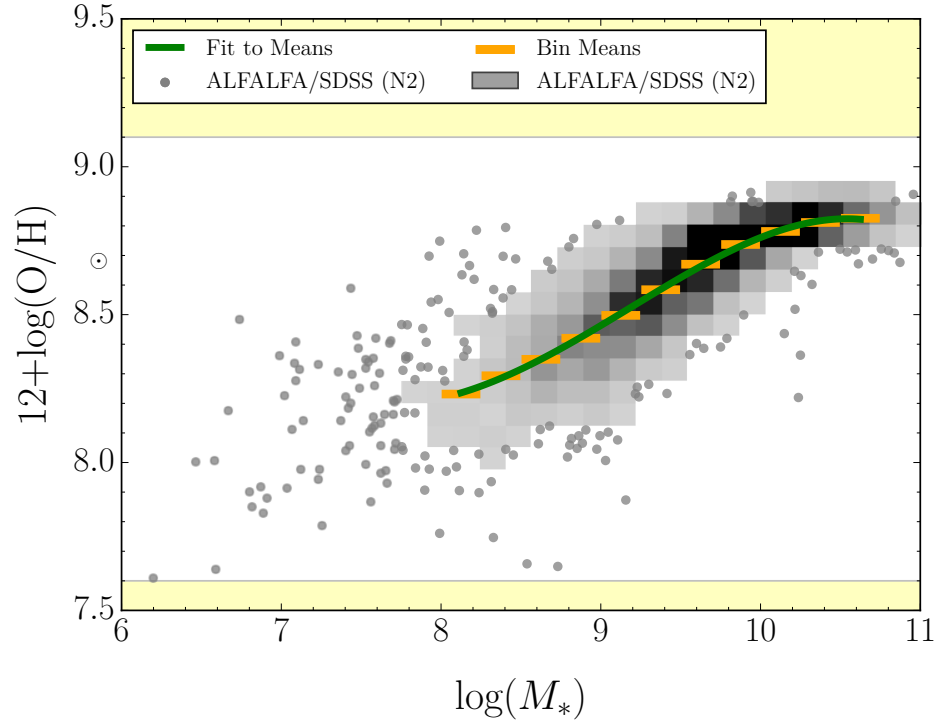


Figure 1.1: Mass-Metallicity Relation. Relation between stellar mass and gas-phase oxygen abundance for $\sim 4,000$ star-forming galaxies in the SDSS. The large orange rectangles represent the mean metallicity in bins of 0.25 dex (in mass). The green line shows a 4th degree polynomial fit to the data. Only bins that include at least 50 data points are included in the plot and the polynomial fit.

Throughout this work, we will study several empirical relations, such as the angular momentum and stellar mass relation (Chapter 2), the stellar mass and metallicity relation (Chapter 3), and the star formation and dust relation (Chapter 4). Many scaling relations are initially developed using “typical” galaxies which are the most abundant, easily observed, and well-behaved galaxies. However, it is important to study how these relationships fare in the most extreme conditions, to see if they hold across the entire spectrum of galaxies, or if they break down, in which case the scaling relationships must be modified to accommodate the new observations. We will focus our attention on two distinct galaxy populations, brightest cluster galaxies (BCGs) which are some of the most massive galaxies in the universe, and dwarf irregular galaxies, which are very low stellar-mass galaxies.

1.2 A Brief Introduction to IFU Spectroscopy

To obtain observations on both populations, we will utilize integral field unit (IFU) spectroscopy. Astronomical spectra are incredibly information dense, and can be used to measure a wide variety of parameters such as: distance, age, chemical composition, kinematics, gas and dust content, stellar mass, and star-formation rate of a galaxy given the appropriate spectral range and resolution. The added benefit of IFU spectroscopy is that it obtains a two-dimensional spatial map of the observed properties for both populations of galaxies. This allows us to spectrally observe the entire surface of a galaxy using a single pointing, whereas other observational techniques would either have to sacrifice information or use an inordinate amount of telescope time.

The first IFU spectrograph (TIGER) saw first light in 1987 (Bacon et al., 1988). Since then, IFU spectroscopy has matured such that large scale astronomical surveys are being performed primarily with IFU data. SAURON (Bacon et al., 2001)

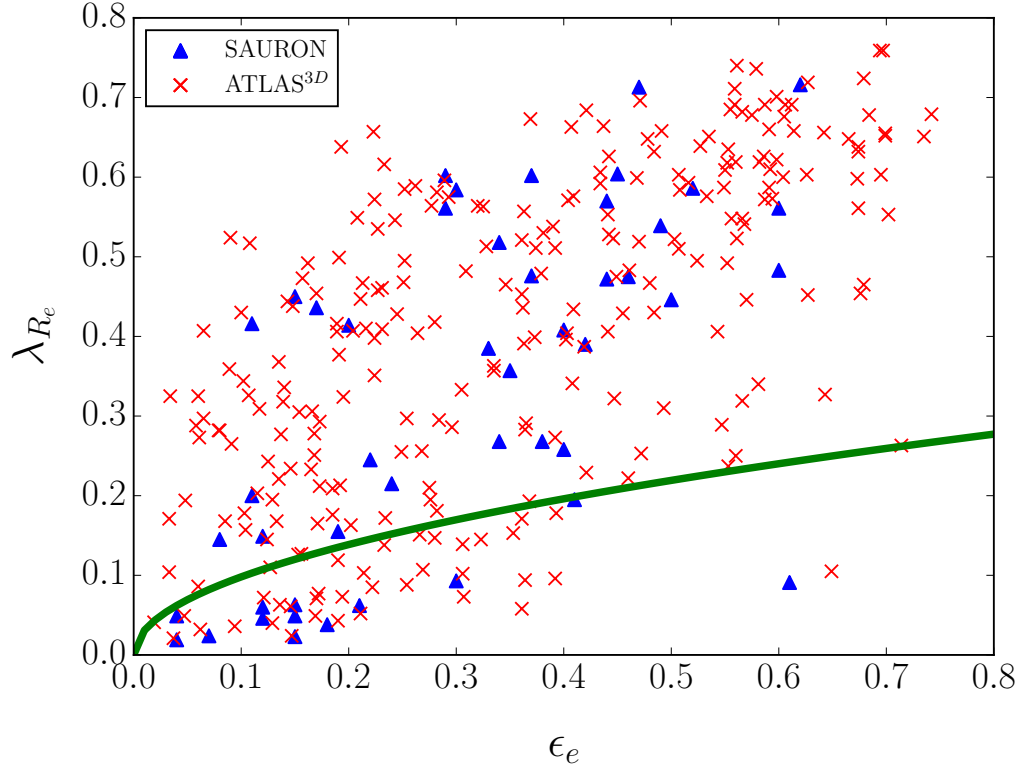


Figure 1.2: Fast Rotator and Slow Rotator Demarcation. Fast and Slow Rotators using data from Emsellem et al. (2011). The thick green line represents the demarcation line between fast and slow rotating galaxies.

and ATLAS^{3D} (Cappellari et al., 2011) were two of the first large-scale IFU surveys, targeting 48 and 260 galaxies respectively. Their initial observations focused on the kinematics of early-type galaxies, in which they reported that a surprising percentage (86%) were fast rotating (Emsellem et al., 2011), and established the accepted demarcation between fast and slowly rotating galaxies (Figure 1.2). Utilizing hydrodynamical simulations compared to the ATLAS^{3D} sample, Naab et al. (2014) classified all central galaxies into 6 archetypical classes based on their morphology, kinematics and formation histories.

Three large-scale IFU surveys are currently in progress, SAMI (Bryant et al., 2015), MANGA (Bundy et al., 2015), and CALIFA (Sánchez et al., 2012). For a comparison of the key parameters of SAMI, MANGA, CALIFA and ATLAS^{3D} see Table 1 of Sánchez (2015). These four surveys are all complimentary in that ATLAS^{3D} has the highest spatial resolution (1''), SAMI samples the widest mass range ($M_* > 10^{8.2} M_\odot$), MANGA has the largest number of objects (10,000), and CALIFA has the largest spatial field of view ($\sim 1.3 \text{ arcmin}^2$). However, none of them specifically target BCGs which are rare in the universe and likely to constitute only a small portion of any sample (e.g. only 1 BCG is in the ATLAS^{3D} sample). Dwarf galaxies will also be largely absent in these surveys due to the difficulties inherent in observing low-luminosity galaxies. Even with the relatively low mass selection of SAMI, they will still only be able to detect the largest and closest of the dwarf galaxy population.

We choose to specifically target these galaxies because they are generally under-represented in galaxy surveys. For instance, ATLAS^{3D} has only 1 BCG in their sample of 260 early-type galaxies, so by adding complimentary observations of 10 additional galaxies, we will overwhelmingly increase the sample size of BCG kinematics being studied with IFU spectroscopy. BCGs are a population of interest

because of their unique formation history and extremely large masses. Despite their large mass, they are often difficult to observe because of their low surface-brightness at large radii. Due to the rarity of BCGs, a large volume of space is necessary to observe a representative samples of BCGs.

A similar problem exists for dwarf irregular galaxies, they are low surface-brightness due to their diffuseness and low stellar-mass. Large scale surveys are likely to target the easiest to observe galaxies, which are also more likely to guarantee high signal-to-noise observations without an inordinate amount of observing time. Dwarf irregular galaxies are uniquely gas rich and metal poor, making them an interesting population because they represent the Local Universe analogs of young, high-redshift galaxies.

We will be discussing two distinct but related types of spectra, absorption-line spectra and emission-line spectra. An absorption spectrum from a galaxy contains information regarding the stellar component of a galaxy, whereas an emission line spectrum reflects the properties of the ionized gas component of a galaxy. At the distance of most galaxies we are unable to resolve individual stars within each galaxy using even the highest spatial resolution IFU spectroscopy. Therefore, we measure the aggregate effects of multiple stars within each spatial pixel. This effect allows us to use these scaling relations, which often rely upon the aggregate effects of large number statistics.

1.3 Brightest Cluster Galaxy Angular Momentum and Mass

Brightest Cluster Galaxies exist in an extreme merger environment which allows them to grow to be some of the most massive galaxies in the universe. They are typically located in the center of their cluster, near the bottom of the cluster's gravitational potential well (von der Linden et al., 2007). As a result of their location, BCGs are expected to undergo more mergers than a typical galaxy (De Lucia and

Blaizot, 2007). The hierarchical structure formation model predicts that BCGs were not formed at their current mass, however they started out smaller and have undergone many mergers throughout time to grow to their present size. Semi-analytical models of BCGs have suggested that these mergers are primarily minor mergers (with a difference in masses $< 1:3$) with on average one major merger (mass ratio $> 1:3$) throughout their formation history (De Lucia and Blaizot, 2007; De Lucia et al., 2012).

Specific features of BCGs, such as their large radii and low surface brightnesses compared to normal elliptical galaxies, are consistent with the products of major dissipationless mergers (e.g. Oegerle and Hoessel 1991; Brough et al. 2005; von der Linden et al. 2007; Lauer et al. 2007; Tran et al. 2008). The fact that multiple minor dry mergers have been shown to remove angular momentum from a galaxy when the mergers are isotropically distributed, combined with the fact that BCGs in simulations undergo a higher than average number of dry merger events, leads us to hypothesize that BCGs are likely to have a lower average angular momentum when compared to standard elliptical galaxies.

Using IFU spectroscopy, we can spatially map out the line-of-sight velocity and velocity dispersion across the surface of a sample of Brightest Cluster Galaxies, and we do not require a-priori knowledge of the rotation axis as would be needed for long-slit observations. We can use this spatial mapping of the kinematics to determine the angular momentum of a galaxy and the dynamical mass. We can compare our sample of BCGs to the larger sample of ATLAS^{3D} early-type galaxies to test whether our population is significantly offset from the general population. If a significant difference is observed, that would be evidence that isotropic mergers are at least partially responsible for removing angular momentum from galaxies. If on the other hand, there is no apparent difference, then that would suggest that despite their

similarities as a population, BCGs have a diverse formation history, and the number of mergers does not primarily determine the angular momentum.

1.4 The Mass-Metallicity Relation

Dwarf irregular galaxies can be used to understand how galaxies behave at the beginning of their lifetimes, whereas BCGs represent the later stages of galaxy evolution. The timescales that galaxies evolve on, billions of years, make it impossible for humans to study a single galaxy evolving, so instead we must study snapshots of evolution across all galaxies. Dwarf irregular galaxies are likely to be the Local Universe analogs of the galaxies that eventually merge together to form BCGs.

We use IFU spectroscopy to observe a sample of dwarf galaxies selected from the ALFALFA blind HI survey (Haynes et al., 2011). Using emission-line fluxes measured with IFU spectroscopy, we can measure the metal content of the gas in the ISM across the whole surface of the galaxy, instead of just the central core as would be obtained from a single fiber observations which would be biased by metallicity gradients within galaxies.

We use IFU spectroscopy to study the chemical abundances of the gas within the dwarf irregular galaxies and observe how the abundances vary as a function of stellar mass. This scaling relation is also known as the mass-metallicity relation (MZR). The MZR is known to exhibit scatter greater than would be expected by the uncertainties on the individual data points (Tremonti et al., 2004; Lara-López et al., 2010; Mannucci et al., 2010).

To explain this apparently enhanced scatter, it has been suggested that the MZR has a dependence on star formation rate (Lara-López et al., 2010; Mannucci et al., 2010; Andrews and Martini, 2013), which could alternatively be explained as a dependence on HI-gas content (Bothwell et al., 2013; Lara-López et al., 2013). This

three-dimensional extension of the mass-metallicity relation is known as the fundamental metallicity relation (FMR). Studies on the FMR thus far, either as a function of star formation rate (FMR_{SFR}) or HI mass (FMR_{HI}), have focused on the SDSS sample of spectroscopically observed galaxies (Lara-López et al., 2010; Mannucci et al., 2010; Bothwell et al., 2013). As such these galaxies are biased towards the intermediate to high stellar-mass galaxies that dominate the SDSS spectroscopic sample. We can test whether or not the low-mass dwarf irregular galaxy population are consistent with the intermediate stellar-mass population FMR scaling law.

Several hypotheses have been proposed for the mechanisms that guide the FMR, e.g. pristine gas inflows diluting metal abundances (Finlator and Davé, 2008; Davé et al., 2010), or the winds created in young star forming regions blowing out the metal and gas content. These two processes are tightly linked, in that a pristine gas inflow that dilutes the metals is also the fuel for star formation, so a large inflow rate of pristine gas is also likely to result in a high star-formation rate. Therefore, it is difficult to disentangle the relative influences of each phenomenon.

Using the dwarf irregular galaxy population we can test whether the FMR_{SFR} and FMR_{HI} scaling relations continue to be valid for low stellar-mass galaxies. If one relation were found to be a significantly better fit for the dwarf galaxy population, that would be an indicator that it is more closely related to the underlying physical mechanism driving the FMR, and would help decouple the degeneracy described above by favoring one physical property as the primary driver.

1.5 The $\text{H}\alpha$ -Balmer Optical Depth Relation

Young star forming galaxies such as the dwarf galaxy population used to study the mass-metallicity relation have more gas, which is typically linked to more dust in the ISM. One cannot ignore the influence of dust when studying even young metal

poor galaxies such as the dwarf irregular galaxies. There is recent evidence of an empirical scaling relation between the star formation rate and the dust mass in the ISM of galaxies (Reddy et al., 2015). The star formation rate is a component of studying the FMR, so it is important that we understand the influence of dust on star formation rate (SFR) measurements to ensure that our SFR estimations are accurate.

A spatial correlation between SFR and enhanced reddening in ionized regions has been observed in samples of larger spiral and elliptical galaxies (Kreckel et al., 2013; Roche et al., 2015). This is often assumed to be the result of dusty birth-clouds that surround young, star-forming regions. It is not yet known at which spatial scales this relationship begins to break down. IFU spectroscopy is vital to testing for a spatial correlation between dust and star forming regions, without it we would be unable to observe the entire surface of a star forming region with a single pointing.

Using the same sample of dwarf irregular galaxies used for the fundamental metallicity relation, we can investigate the spatial mapping of the $H\alpha$ emission and the Balmer optical depth, a tracer of dust content, in a sample of 11 dwarf irregular galaxies selected from the ALFALFA survey. We test to see if regions as small as $(30 \text{ pc})^2$ exhibit a correlation between higher $H\alpha$ luminosity and enhanced reddening. If the correlation between these values does continue to hold, that would suggest that we can still treat the observations in those regions the same as the integrated light of the galaxy itself, and that small number statistics have not yet begun to dominate the observations. If, however, the relationship does begin to break down, that would suggest that observations no longer follow the empirical scaling relation of the aggregate population and the physical effects of individual stars have begun to dominate.

Throughout this dissertation, we will focus on using the incredible amount of

information provided by IFU spectroscopy to study various empirical scaling laws. In Chapter 2, we will first use IFU spectroscopy to examine the relationship between angular momentum and dynamical mass in the most massive galaxies in the universe, and test to see if they behave differently when compared to other massive galaxies not located near the center of their cluster. In Chapter 3, we will transition to studying very low stellar-mass dwarf irregular galaxies, again using IFU spectroscopy to study galaxies that are very faint and difficult to detect. We will examine whether or not very low mass galaxies are consistent with the established mass-metallicity relationship, and test to see whether HI-gas mass or SFR is more favored for the fundamental metallicity relation in low stellar-mass galaxies. Finally, in Chapter 4, we will use the spatial information provided by IFU spectroscopy to examine the connection between $H\alpha$ emission indicative of star formation, and the Balmer optical depth, which traces dust content. We will test if the relationship continues to hold to small spatial scales, nearing the sizes of gas cores that form individual stars. In each chapter, we assume a Hubble constant of $H_0 = 70 \text{ km s}^{-1} \text{ Mpc}^{-1}$ and $\Omega_M = 0.3$, $\Omega_\Lambda = 0.7$.

2. ANGULAR MOMENTA, DYNAMICAL MASSES, AND MERGERS OF BRIGHTEST CLUSTER GALAXIES*

2.1 Synopsis

Using the VIMOS Integral Field Unit (IFU) spectrograph on the Very Large Telescope (VLT), we have spatially mapped the kinematic properties of 10 nearby Brightest Cluster Galaxies (BCGs) and 4 BCG companion galaxies located within a redshift of $z = 0.1$. In the hierarchical formation model, these massive galaxies ($10^{10.5}M_{\odot} < M_{dyn} < 10^{11.9}M_{\odot}$) are expected to undergo more mergers than lower mass galaxies, and simulations show that dry minor mergers can remove angular momentum. We test whether BCGs have low angular momenta by using the λ_{Re} parameter developed by the SAURON and ATLAS^{3D} teams and combine our kinematics with Sloan Digital Sky Survey (SDSS) photometry to analyze the BCGs' merger status. We find that 30% (3/10) of the BCGs and 100% of the companion galaxies (4/4) are fast rotators as defined by the ATLAS^{3D} criteria. Our fastest rotating BCG has a $\lambda_{Re} = 0.35 \pm 0.05$. We increase the number of BCGs analyzed from 1 in the combined SAURON and ATLAS^{3D} surveys to 11 BCGs total and find that above $M_{dyn} \sim 11.5M_{\odot}$, virtually all galaxies regardless of environment are slow rotators. To search for signs of recent merging, we analyze the photometry of each system and use the $G - M_{20}$ selection criteria to identify mergers. We find that $40 \pm 20\%$ of our BCGs are currently undergoing or have recently undergone a merger (within 0.2 Gyrs). Surprisingly, we find no correlation between galaxies with high angular momentum and morphological signatures of merging.

*Reprinted with permission from “Angular Momenta, Dynamical Masses, and Mergers of Brightest Cluster Galaxies” by Jimmy et al., 2013. The Astrophysical Journal, Volume 778, Issue 2, article id. 171, 12 pp., Copyright 2013 by the American Astronomical Society.

2.2 Background Information

Galaxies are expected to grow hierarchically in a Λ CDM universe. In this framework, clouds of dark matter cool down and begin to collapse, forming the structure upon which galaxies and clusters are formed (Peebles, 1969; Doroshkevich, 1970; White, 1984). Simulations of mergers of dark-matter halos have shown that major mergers (progenitor mass ratios of 1:1 or 2:1) increase the angular momentum of the combined dark-matter halo (Vitvitska et al., 2002). Other studies have shown that minor mergers either slightly increase or simply preserve the angular momentum of a dark-matter halo (D’Onghia and Burkert, 2004). Without taking into account the interactions of baryons, merger events (whether major or minor) appear to increase a dark-matter halo’s specific angular momentum.

When accounting for baryons, the connection between mergers and angular momentum changes slightly. Although the effects of baryons within 1 effective radius (R_e) are uncertain (van den Bosch et al. 2002, de Jong et al. 2004), we can examine merger simulations that include baryons to see how merging galaxies behave on a large scale. Spiral galaxies, which have a high initial angular momentum, have cold stellar discs that are fragile and easily destroyed in mergers (Naab et al., 2006). When these initially discy high angular momentum galaxies merge together, they form early-type galaxies that were expected to be dispersion-supported and not rotation-supported. However Emsellem et al. (2007) showed that early-type galaxies can still exhibit a high angular momentum, and in fact the majority of them do (86% in Emsellem et al. 2011). The mechanism by which these early-type galaxies have retained or regained their angular momentum is still uncertain.

One possible explanation for the high angular momentum observed in early-type galaxies comes from simulations of gas-rich mergers. In the early universe ($z > 2$),

before feedback mechanisms have had a significant impact on galaxy composition, galaxy mergers are expected to be gas-rich (Tacconi et al., 2010). Simulations of mergers of equal-mass, gas-rich galaxies (wet major mergers) have been shown to produce high angular momentum galaxies (Naab et al., 2006). The dissipational effect of gas appears to be an important factor in forming a high angular momentum merger remnant (Bender et al. 1992, Kormendy and Bender 1996, Faber et al. 1997, Naab et al. 2006).

However gas-rich mergers are only expected at intermediate/high redshifts. From $z = 2$ until the present, as feedback mechanisms remove gas from the galaxies, mergers are expected to be increasingly gas-poor and dissipationless. In the case of major gas-poor (dry) mergers, Bois et al. (2011) have shown that major dry mergers are capable of forming galaxies with a variety of angular momenta, depending upon the initial orbital parameters. They find little dependence of a merger remnants angular momentum on the progenitor galaxy's gas fraction. For a galaxy to transform from an initially fast rotating galaxy into a slowly rotating galaxy, said galaxy has to accrete at least half of its mass via dry minor mergers (Bournaud et al. 2007, Jesseit et al. 2009, Bois et al. 2010, Bois et al. 2011). The environment in which a galaxy exists will determine the frequency of major and minor galaxy mergers.

2.2.1 Merger History of Brightest Cluster Galaxies

Brightest Cluster Galaxies (BCGs) exist in an extreme environment. They are typically located in the center of their cluster, near the bottom of the cluster's potential well. As a result of their location, BCGs are expected to undergo more mergers than a typical galaxy. The increased frequency of merging events in BCGs should make them sensitive to the relation between galaxy mergers and angular momentum.

The large number of merging events is also likely the cause of the high mass and

early-type classification observed in a typical BCG. Observations by Lidman et al. (2012) have shown that BCGs have grown in mass since $z = 1.6$ and on average, have grown by a factor of 1.8 ± 0.3 from $z = 0.9$ to $z = 0.2$. Similarly, simulations of galaxy growth via mergers by De Lucia and Blaizot (2007) have shown that only half the mass of a BCG is in place by $z = 0.5$. The same simulations found that the majority of stars within a BCG formed very early, with 50% of the stars being formed before $z = 5$ (De Lucia and Blaizot, 2007). In this scenario, BCGs would have accumulated half of their mass in the time frame from $z = 0.5$ to $z = 0$ via gas-poor mergers.

The fact that multiple minor dry mergers have been shown to remove angular momentum from a galaxy when the mergers are isotropically distributed, combined with the fact that BCGs in simulations undergo a higher than average number of dry merger events, leads us to hypothesize that BCGs are likely to have a lower average angular momentum when compared to standard elliptical galaxies. In other studies BCGs have been shown to be remarkably uniform and exhibit special characteristics when compared to elliptical galaxies not at the center of their cluster. von der Linden et al. (2007), showed that a typical BCG is more likely to host a radio-loud AGN, is larger in size, and has higher velocity dispersion on average than a typical elliptical galaxy in the same mass range. These currently observed differences are likely the result of the combination of two effects: BCGs' large stellar masses and BCGs' location at the bottom of their host clusters' potential well, although it is uncertain which effect dominates.

Specific features of BCGs, such as their large radii and low surface brightnesses compared to normal elliptical galaxies are consistent with the products of major dissipationless mergers (e.g. Oegerle and Hoessel 1991; Brough et al. 2005; von der Linden et al. 2007; Lauer et al. 2007; Tran et al. 2008). Their sizes and velocity

dispersions may have also evolved faster than less-massive early-type galaxies since $z \sim 0.3$ (Bernardi 2009 although, c.f. Stott et al. 2011). These two factors cause the Faber-Jackson relation between luminosity and velocity dispersion to be flatter for BCGs. Similar studies of the Fundamental Plane (FP) have found differing slopes between populations of BCGs and elliptical galaxies (Desroches et al., 2007). The differing slope of the Faber-Jackson relationship and the Fundamental Plane for BCGs compared to ellipticals supports the scenario where BCGs form mainly via dissipationless mergers (Boylan-Kolchin et al., 2006).

2.2.2 *Signatures of Recent Merging in BCGs at $z < 0.1$*

By combining spectroscopic information with photometric information, we examine the recent merger history of a sample of 10 BCGs. Integral Field Unit (IFU) spectroscopy allows us to observe the kinematic properties of galaxies in two dimensions, showing whether they are largely rotation-supported or dispersion-supported. The SAURON team have developed the λ_R parameter, which utilizes the increased spatial information from IFU spectroscopy to quantify the observed stellar angular momentum in galaxies (Emsellem et al., 2007). They used this parameter to quantify the angular momentum of 48 early-type galaxies. This work was followed by the ATLAS^{3D} team, which performed a similar analysis on 260 galaxies (Emsellem et al., 2011). In both studies they classified galaxies as either Fast Rotators (FR) or Slow Rotators (SR) based on their λ_R value within 1 effective radius (R_e).

The λ_R parameter provides a quantitative method to compare the stellar kinematics of BCGs to those of other early-type galaxies, however the SAURON sample has only 4 galaxies with $M_{dyn} > 10^{11.5} M_\odot$ and only includes one BCG (M87). The ATLAS^{3D} survey studies an additional 10 galaxies with $M_{dyn} > 10^{11.5} M_\odot$. Above $10^{11.5} M_\odot$ only 23% of galaxies from the ATLAS^{3D} survey are classified as fast rota-

tors (Emsellem et al., 2011). The mass limit of $10^{11.5}M_{\odot}$ may be important as Peng et al. (2010) have shown that above $M_{*} = 10^{11.5}M_{\odot}$ the majority of galaxies have undergone a major merger after their star formation was quenched. If dry mergers preferentially remove angular momentum, then we would expect to see fewer BCGs above $10^{11.5}M_{\odot}$ with a high λ_R value.

In order to determine the recent merger history of our galaxies, we use a combination of Source Extractor (SExtractor) (Bertin and Arnouts, 1996), GALFIT (Peng et al., 2002), and PyMorph (Vikram et al., 2010) to produce photometric models of these galaxies. We then subtract our models from the original image to identify tidal tails, multiple cores, and excess intra-cluster light, which would all be signs of merging that can be identified visually. A more quantitative detection of merging comes from the $G - M_{20}$ (Gini coefficient minus the 2nd order moment of the brightest 20% of pixels) value for each galaxy. According to simulations, these parameters would tell us if there was a dry merger within the last 0.2 Gyrs (Lotz et al., 2011). After 0.2 Gyrs merger information will have been erased by dynamical friction, meaning this selection criterion is only able to inform us of very recent or currently ongoing mergers.

It is our goal to measure λ_R , dynamical mass, and recent merger history for our sample of BCGs and compare our kinematic results to the SAURON and ATLAS^{3D} results for early-type galaxies. We present targeted observations of BCG stellar kinematics and photometrics for 7 BCGs with close companions and 3 BCGs with no close companion. In our initial selection, we specifically chose BCGs with close companions to determine if the companions also have high λ_R . We also determine if morphological signatures of merging are correlated with λ_{Re} measurements.

2.3 Observations

2.3.1 Spectroscopic Measurements

In von der Linden et al. (2007), a sample of 625 BCGs ($z < 0.1$) were selected from the C4 cluster catalogue (Miller et al., 2005) of the Third Data Release of the Sloan Digital Sky Survey (SDSS; York et al. 2000). In Brough et al. (2011) BCGs with companions within $\sim 10''$ (18 kpc at $z \sim 0.1$) were chosen from the von der Linden sample. We are using the same 4 galaxies from Brough et al. (2011) as well as 7 new galaxies chosen by the same criteria as Brough et al. (2011). The redshifts of these objects are in the range $0.04 < z < 0.1$. As a matter of shorthand, we will drop the SDSS-C4-DR3 prefix from all target BCG names, and simply use the last 4 digits that are unique to each cluster. In total, our initial sample size is 7 BCGs with companions and 4 BCGs without companions within $\sim 10''$. One target, BCG 1067, will be omitted from analysis because it had excessively noisy observations and we were unable to obtain results on that BCG above our signal-to-noise cut of 10.

The first set of BCGs were observed with VIMOS (Le Fèvre et al., 2003) on the VLT from April to August of 2008 (Program ID 381.B-0728) and the second set were observed, also with VIMOS, from April to July of 2011 (Program ID 087.B-0366). VIMOS was used in IFU mode with the high-resolution blue grism and a spatial sampling of $0.67''/\text{pixel}$ (BCGs 1153 and 1067 were observed with a spatial sampling of $0.33''/\text{pixel}$). This gives a field-of-view (FOV) of $27'' \times 27''$ ($13'' \times 13''$ for 1153 and 1067). The VIMOS HR Blue grism (pre March 15th 2012 version) has a spectral range of 4150 - 6200 Å and a spectral resolution of $0.51 \text{ Å}/\text{pixel}$. Observations were made during dark time, with an average seeing of $0.9''$. Average seeing for individual galaxies can be seen in Table 2.1.

Table 2.1: Observing Properties of BCGs and Companions

Galaxy (SDSS-C4-DR3)	RA (J2000)	Dec (J2000)	Seeing (") ± 0.01	Integration Time (s)	Number of exposures	Observation Date	Cluster Velocity Dispersion σ (km s ⁻¹)
1027	12:47:43.4	-00:09:07	1.0	6900	6	04-05-08 & 06-03-08	1020
1042	15:15:18.0	+04:22:54	0.8	6000	6	05-04-11 & 05-30-11	857
1048	13:42:09.6	+02:13:38	1.0	6000	6	04-08-11 & 07-30-11	828
1050	13:44:25.8	+02:06:36	0.8	3450	3	04-27-08	514
1066	13:31:10.8	-01:43:49	0.8	3450	3	05-12-08	814
1153	16:04:13.7	+00:03:13	0.8	6800	6	04-05-08 & 06-04-08	295
1261	12:25:33.4	+09:23:29	0.8	6000	6	04-30-11	520
2001	23:24:18.0	+14:38:00	0.9	3450	3	08-09-08	695
2039	22:31:43.2	-08:24:32	1.2	10000	10	06-04-11 & 06-05-11	505
						06-29-11 & 06-30-11	
2086	23:22:56.4	-10:02:44	1.2	3450	3	08-02-08	599

Seeing is the average over all exposures for each galaxy. BCGs 1027, 1050, 1066, and 2086 were also analyzed in Brough et al. (2011). Cluster velocity dispersion is from von der Linden et al. (2007)

2.3.1.1 IFU Data Reduction

Initial IFU data reduction is achieved using the VIMOS Pipeline (Izzo et al., 2004). A VIMOS field-of-view is split into four quadrants, and initially each quadrant is reduced separately by the VIMOS Pipeline. The VIMOS Pipeline makes the necessary calibration files (master bias, arc spectrum, flat field, fiber identification, etc.). The VIMOS Pipeline also extracts the science spectrum in each fiber from the raw science frames.

The science spectra are then fed into IDL routines, where we first mask the bad fibers so that they do not interfere with the data reduction process. For each quadrant, a sky background spectrum is calculated by taking the median over the spaxels (spatial pixels) that do not contain a significant contribution of light from the target galaxy. Sky spaxels are selected by plotting the intensity in every spaxel, and looking for a sustained minimum in the intensities across several adjacent fibers. We perform a Gaussian fit to the 5577 Å [OI] skyline. This fit is used to normalize the transmission in each spaxel across the whole quadrant. Since the strength of the skyline should be the same in all spaxels, each individual spectra is scaled so that its skyline flux matches the median skyline flux across all spaxels. We then subtract the Gaussian fit from the spectra to remove the skylines. Once this has been completed for each quadrant, we combine the four quadrants into one data cube, and then renormalize transmission across the whole cube using the strength of the skylines once again (skyline information was preserved from the earlier step). This provides us with a data cube containing two dimensional spatial information, with the spectrum being the third dimension.

Each BCG observation consists of multiple dithered exposures, so we stack the multiple exposures with a 5σ clipped mean. With our stacked data cube, we then

perform a signal-to-noise cut, where we discard any spaxel with an overall S/N ratio less than 5. We use the 2-dimensional adaptive spatial binning code of Cappellari and Copin (2003) to re-bin pixels to a minimum S/N ratio of 10 per pixel. This takes the fibers that are below the final S/N cutoff and finds fibers near them to bin together so they reach our required S/N ratio.

2.3.1.2 *Stellar Kinematics*

The stellar kinematics (velocity, V , and line-of-sight velocity dispersion, σ) of the galaxy are computed from the binned spectra using a penalized pixel fitting scheme, (pPXF; Cappellari and Emsellem 2004) and the MILES (Medium-resolution Isaac Newton Telescope Library of Empirical Spectra; Sánchez-Blázquez et al. 2006) evolutionary stellar population templates. This method determines the stellar kinematics by fitting templates to the absorption line features in the spectra. We choose 10 templates of stars in the range of G6 to M1 (luminosity classes III, IV, and V) from the MILES library and convolve them using the quadratic difference between the resolution of the library and the observations. The pPXF fits are performed in the region around the observed G-band and Calcium H and K absorption features (4200 - 4900 Å). The MILES templates cover a similar wavelength range to VIMOS and have a similar spectral sampling (FWHM = 1.8 Å).

Velocity dispersion for a galaxy as a whole is found by co-adding all fibers within the effective radius of a galaxy into one bin, and performing a pPXF fit on the binned spectrum as in Cappellari et al. (2006). As an alternative method for calculating the velocity dispersion of the whole galaxy, we also tried calculating the luminosity weighted mean of each individual bin's velocity dispersion. These results were often not in agreement with the effective spectrum method. However, by integrating (preliminary) inclination information as described in Eq. 29 of Cappellari et al. (2013),

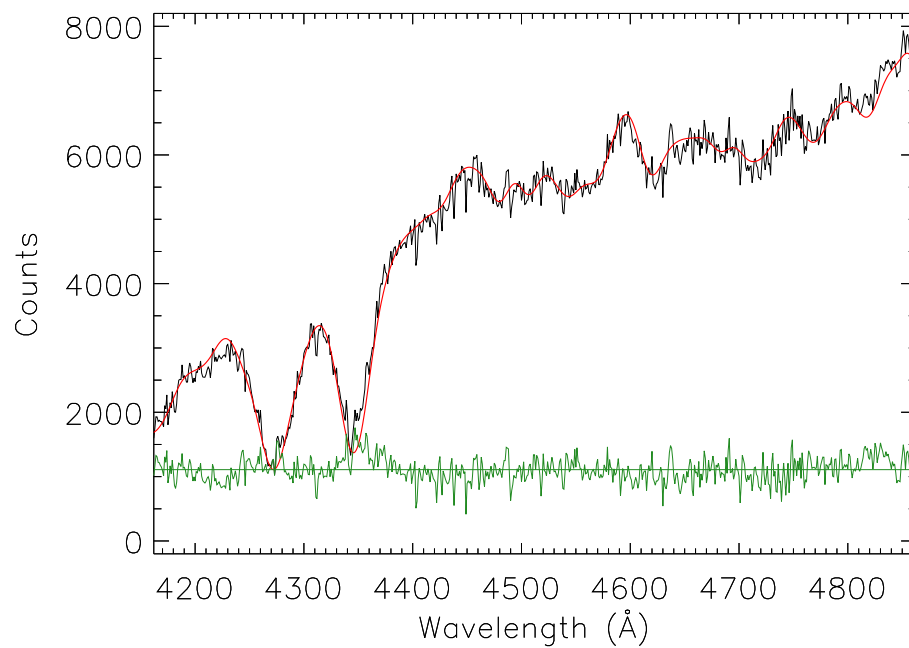


Figure 2.1: Example pPXF Fit to Spectrum. The spectrum pictured here is the result of co-adding every spaxel within the effective radius of the BCG 1050. The black line is the science spectrum, and the red line is the best fit produced by pPXF. The green line is the residual from the best fit.

the two velocity dispersion measuring methods appear to be in agreement. We choose to use the effective spectrum method instead of the weighted mean method because of the higher S/N ratio afforded by binning many spaxels together. The effective spectrum method also simulates an observation with a single aperture of radius R_e .

We perform 100 Monte Carlo realizations on each observation to estimate the uncertainty in our results. This process involves adding random noise on the order of the background noise to each binned spectrum, and performing the pPXF fit again on the noisy data. We repeat this process 100 times, then take a weighted mean of all the fits with the random noise added. The standard deviation of all the fits is our uncertainty for our velocity and velocity dispersion results. Typical uncertainties of both values are on the order of 20 km/s. Errors on M_{dyn} and λ_R are propagated from these errors using standard Taylor series error propagation techniques.

The IDL code described above to reduce our data is publicly available¹.

2.3.2 Photometric Measurements

Photometric observations are taken from SDSS Data Release 3. For our analysis we use only the r-band images of each galaxy. Each galaxy is modeled twice, once using a combination of Source Extractor (Bertin and Arnouts, 1996) and GALFIT (Peng et al., 2002) with a single component de Vaucouleurs profile, and a second time using PyMorph (Vikram et al., 2010) to obtain the Gini and M_{20} coefficients. The de Vaucouleurs profile is used to find the effective radius of each galaxy.

Effective radius measurements are found by first feeding the SDSS r-band image into Source Extractor to obtain a catalog of all sources identified in the image. We use the objects catalog to determine the centers of the galaxies we wish to model in GALFIT. We also invert the segmentation map produced by Source Extractor

¹<http://galaxies.physics.tamu.edu/index.php/Jimmy#Code>

(non-zero pixels are set to zero, and pixels that were originally zero are set to one) to generate the bad pixel mask that will be used with GALFIT. The default values and keyword searches were used as inputs to Source Extractor except the following: MAG_ZEROPOINT = 25.61, BACK_SIZE = 256, and PIXEL_SCALE = 0.396. The original SDSS r-band images are then fed into GALFIT using the position, magnitude, effective radius, axis ratio, and position angle found by Source Extractor as initial assumptions. We model each galaxy using a single component de Vaucouleurs profile in GALFIT. We generate our Point Spread Function (PSF) by using a 2-4 gaussian fit in GALFIT to model a point source near each galaxy. Residual maps are inspected by eye to determine if the fit appears to be reasonable, and if not, initial parameters are adjusted until a reasonable fit is found.

PyMorph combines Source Extractor, GALFIT, and other added analysis routines in a python wrapper in order to automate the photometric analysis process. It is used to determine the merger properties of our sample of galaxies. We use it to make two component models for each galaxy. We then perform a visual inspection of the residual image to check for the goodness of the fit.

PyMorph also reports the Concentration, Asymmetry, Clumpiness, Gini Coefficient, and M_{20} for each galaxy that is modeled. We use the relation between the Gini Coefficient and M_{20} to search for recent mergers. The Gini coefficient measures uniformity of the distribution of a galaxy's light (Abraham et al., 2003) and M_{20} measures the distribution of the brightest 20% of pixels. The relation between these two properties tells us if there are irregularities in the galaxy's light distribution, signaling some type of violent interaction. We can rule out the possibility that anomalies in these parameters are due to projection effects because we can measure the redshift of each galaxy to confirm that they are indeed located near each other in physical space.

2.4 Results

2.4.1 Kinematic Maps

We begin our spectroscopic analysis with the velocity maps seen in Figures 2.2 & 2.3. Our first goal is to search for visual signs of galaxy rotation. Figure 2.2 shows the velocity maps of the galaxies without companion measurements. This sample contains three of our control galaxies, BCGs 1042, 1050, and 1153, which were selected to not have any companions within $10''$. The S/N on the companion galaxies of BCGs 2001, 2039, and 2086 was below 10 after binning, meaning we were unable to achieve accurate measurements of the companion's kinematic properties.

By visual inspection of Figure 2.2, we see that 5 of the BCGs (1042, 1050, 2001, 2039, and 2086) appear to have little to no rotation. They have a uniform velocity across the entire BCG and the velocities measured in each spaxel of the BCG are very near 0 km/s. These observations are consistent with a dispersion-supported early-type galaxy. Two of the BCGs (1153 and 1261) in Figure 2.2 appear to have velocity gradients across their surface, with BCG 1261 being the most obvious example.

Figure 2.3 shows velocity maps of the BCGs that have bright enough companions to measure the companion's kinematic properties. In each collapsed IFU field-of-view, the BCG is labeled with the letter A, and then brightest companion is labeled B, and so on. BCG 1048 appears to have one side very red-shifted and the opposite side very blue-shifted, suggesting rotation. Note also that all the companions in Figure 2.3 appear to exhibit rotation.

The velocity dispersion map (Figure 2.4) shows very high dispersions in BCG 1048, suggesting a possible ongoing interaction. We also see in Figure 2.4 a peak in the dispersion near the center of BCG 1261. This peak could be the result of seeing both the positive and negative velocities on either side of the axis of rotation in the

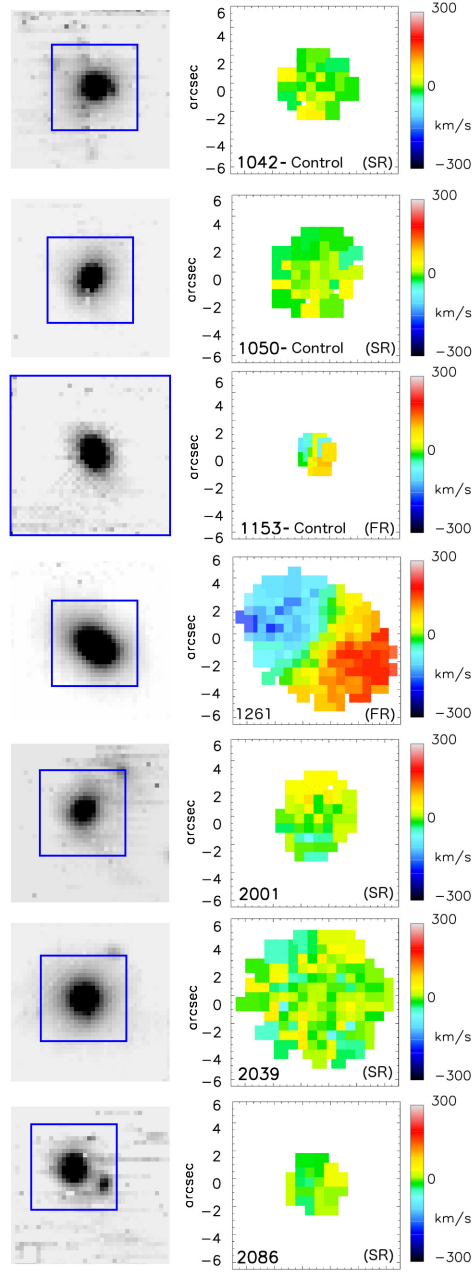


Figure 2.2: IFU Velocity Maps of BCGs Without Companions. Left: Collapsed IFU images showing the full VIMOS FOV with the $12'' \times 12''$ boundary of the velocity maps highlighted in blue. Right: Velocity maps of BCGs scaled to $12'' \times 12''$. Only spaxels with a $S/N > 10$ are shown. BCGs 1050 (SR), 1042 (SR), and 1153 (FR) were chosen as control galaxies with no companions within $10''$. Slow rotating galaxies (1042, 1050, 2001, 2039, 2086) exhibit very little change in velocity across the galaxy, suggesting that these are either completely face-on or dispersion-supported galaxies. In the fast rotating galaxies (1261, 1153) there is a velocity gradient across the major axis, showing evidence of rotation.

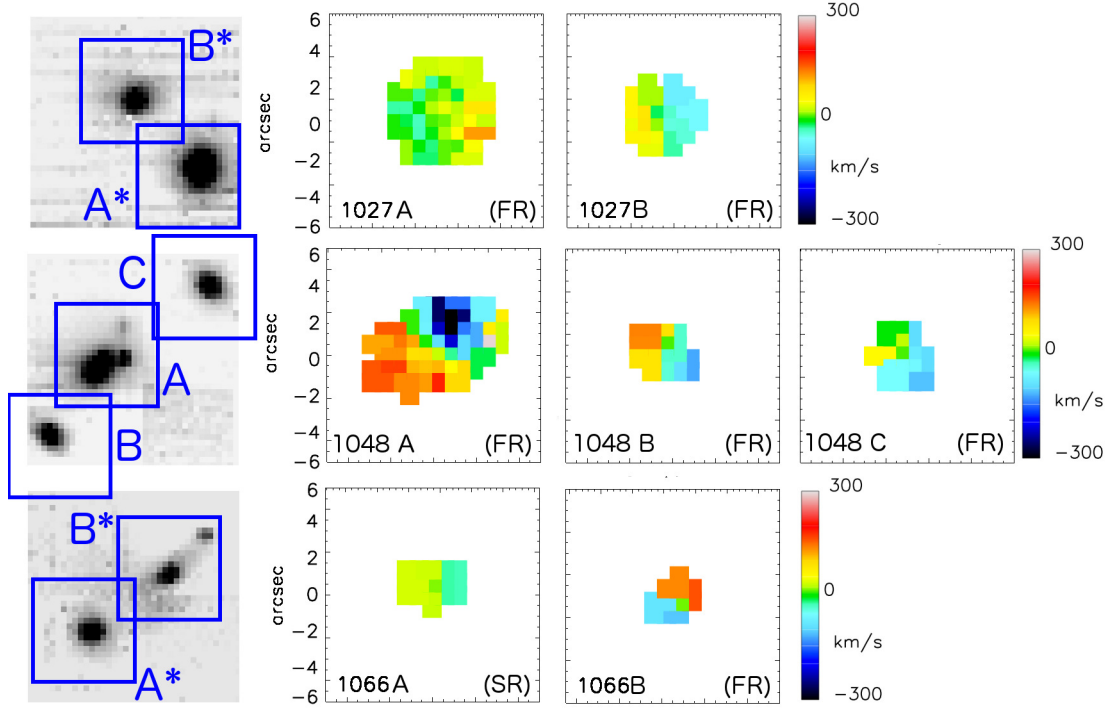


Figure 2.3: IFU Velocity Maps of BCGs With Companions. Left: Collapsed IFU images showing the full VIMOS FOV with the $12'' \times 12''$ boundary of the velocity maps highlighted in blue. Right: Velocity maps of BCGs scaled to $12'' \times 12''$. BCGs are labeled with the letter A, the brightest companion is labeled B, and so on. BCG 1048, as well as the companions of the BCGs in clusters 1027, 1048, and 1066 all show signs of rotation. Both companions of 1066 and 1027 were shown to be bound to their BCG neighbor in Brough et al. (2011) However neither outer companions are gravitationally bound to BCG 1048. Bound systems are indicated with a star in collapsed IFU images. Velocities shown for each galaxy are relative to the individual galaxy's redshift, and not absolute across the whole system.

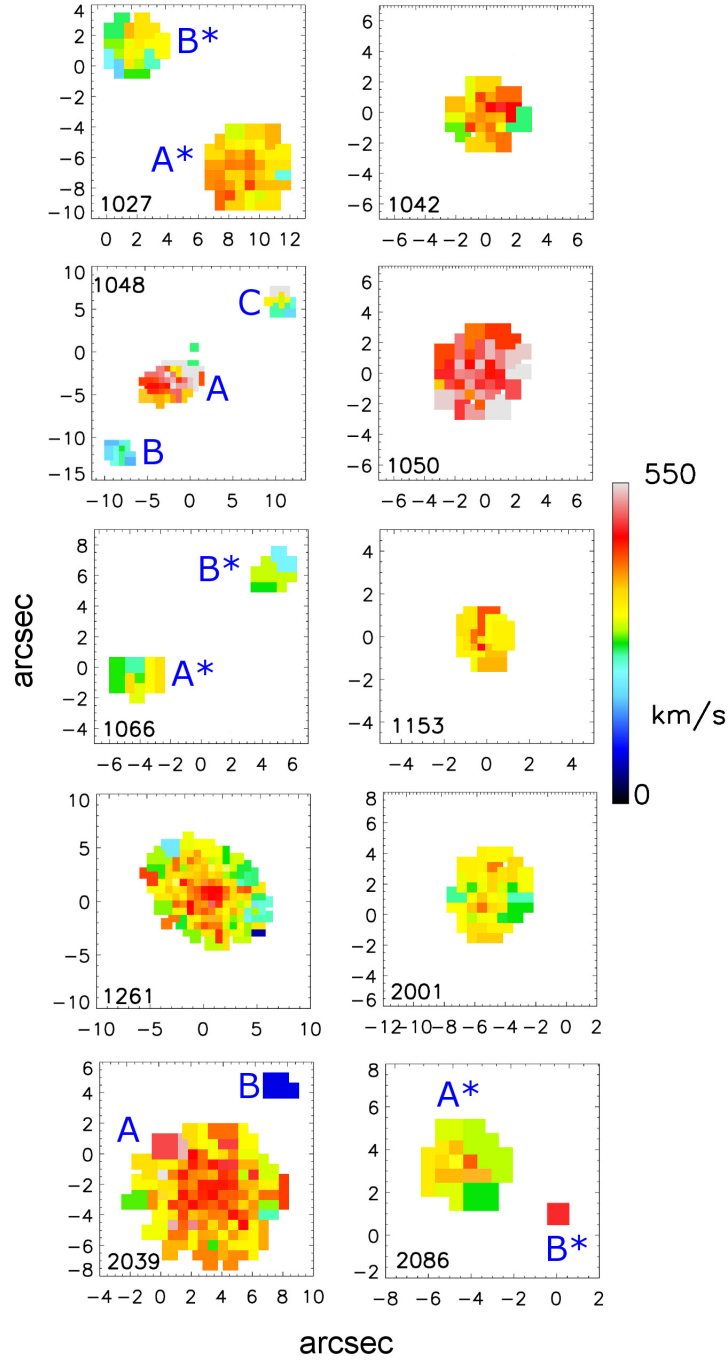


Figure 2.4: IFU Velocity Dispersion Maps of BCGs and Companions. BCGs are labeled with the letter A, the brightest companion is labeled B, and so on. Bound systems are indicated with a star. In BCG 1261 there is a rise in the dispersion in the center of the BCG, suggesting that the velocity gradient seen in the velocity maps is due to rotation.

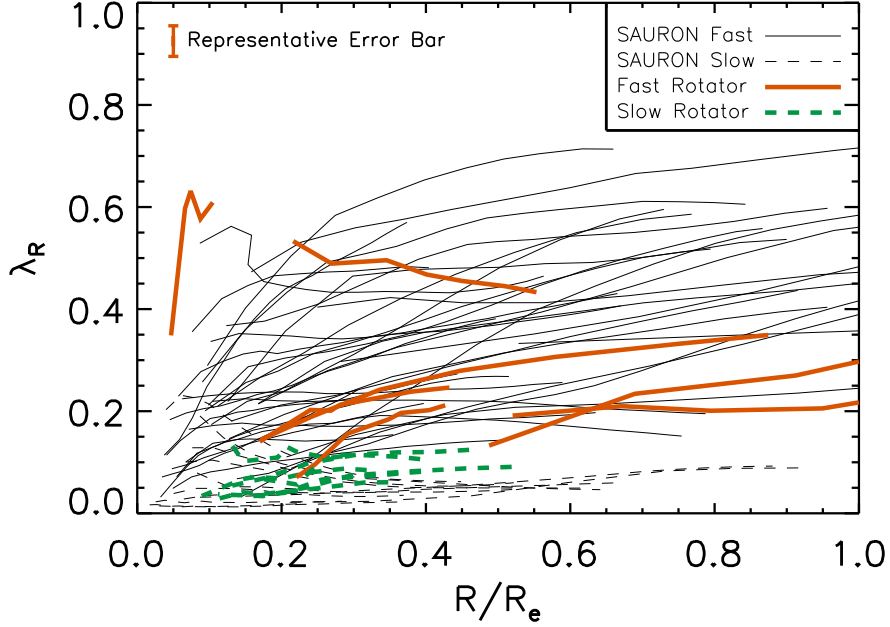


Figure 2.5: Angular Momentum Profile of BCGs. Our sample of galaxies are plotted with thick orange and green lines. The SAURON sample is plotted in grey. We choose not to plot the full ATLAS^{3D} sample of 260 galaxies in order to keep the plot legible. Fast rotators are plotted as solid lines and slow rotators are plotted as dashed lines. Fast rotators have a convex profile, and slow rotators have a concave profile.

same fiber, enhancing the observed dispersion.

2.4.2 Angular Momenta (λ_R)

In order to quantify the rotation seen in some of the BCGs mentioned above, we use the λ_R parameter developed by the SAURON team (Emsellem et al., 2007). This parameter acts as a proxy for angular momentum, and is defined as

$$\lambda_R \equiv \frac{\langle R|V| \rangle}{\langle R\sqrt{V^2 + \sigma^2} \rangle} \quad (2.1)$$

where R is the distance of the spaxel to the galaxy center, V is the velocity of the spaxel, and σ is the velocity dispersion. The numerator acts as a surrogate for the angular momentum, and the denominator acts as a mass normalization. The brackets in the numerator and the denominator denote a luminosity weighted average.

The λ_R profile for each BCG and companion galaxy, plotted along with the SAURON results, can be seen in Figure 2.5. A higher λ_R value indicates higher angular momentum. As expected angular momentum tends to increase with radius, especially in galaxies classified as fast rotators. Galaxies that fit into the Fast Rotator (FR) category appear to have a convex profile as λ_R increases with radius, whereas most Slow Rotator (SR) galaxies have a concave profile. Most of our BCGs appear to have profiles consistent with the slow rotator category.

λ_{Re} is the measured angular momentum at the effective radius. In cases where S/N of our measurements drops below 10 before we reach $1R_e$, we assume that value of λ_{Re} is the furthest measured λ_R in that galaxy. This likely gives a minimum value for λ_{Re} because λ_{Re} tends to increase with radius within $1R_e$ as observed in the SAURON results in Figure 2.5.

The SAURON survey was followed by the ATLAS^{3D} survey, which refined the definition of a fast rotating galaxy to take into account the ellipticity of the galaxy, which the original SAURON definition does not. According to the ATLAS^{3D} definition, the threshold for a fast rotator is

$$\lambda_{Re} > (0.31 \pm 0.01) \times \sqrt{\epsilon_e} \quad (2.2)$$

(Emsellem et al., 2011), where ϵ_e is the ellipticity at the effective radius (R_e). Epsilon is measured by the IDL routine `find_galaxy.pro` written by Michele Cappellari and

available as part of the `mge_fit_sectors` package².

The λ_{Re} vs. ϵ_e plot in Figure 2.6 shows our quantitative determination of galaxy rotation. Using the ATLAS^{3D} definition, all galaxies above the blue line are classified as fast rotators. We find that 3 BCGs and all 4 companions are fast rotators. Seven of our BCGs are within 1 standard deviation of the dividing line, causing us to doubt their classification. For them we consider their λ_R profiles to see if they are concave or convex in order to make our determinations. By the curve criteria, we consider 6 of these ambiguous galaxies to be slow rotators. Giving us a final total of 3 fast rotating BCGs (30%) and 4 fast rotating companion galaxies (100%).

2.4.3 Dynamical Mass

Next we examine the relation between a galaxy's dynamical mass and its λ_{Re} measurement. We determine the dynamical mass of the galaxy by using the equation provided by Cappellari et al. (2006):

$$M_{dyn} = \frac{5R_e\sigma_e^2}{G} \quad (2.3)$$

R_e is the effective radius, σ_e is the aperture corrected velocity dispersion at the effective radius, and G is the gravitational constant. The factor of five is a parameter that scales between the virial and Schwarzschild M/L estimates. According to theory it should be 5.953, however those calculations assume perfect one-component isotropic spherical systems, whereas 5 is found to be a good fit for observed galaxies (Cappellari et al., 2006). In order to compensate for the fact that most of our velocity dispersions reported are measured at $R < R_e$, we have applied the aperture correction from Eq. 1 of Cappellari et al. (2006) to our velocity dispersion results.

Dynamical mass results for each galaxy are listed in Table 2.2. In Figure 2.7 we

²<http://www-astro.physics.ox.ac.uk/~mxc/idl/>

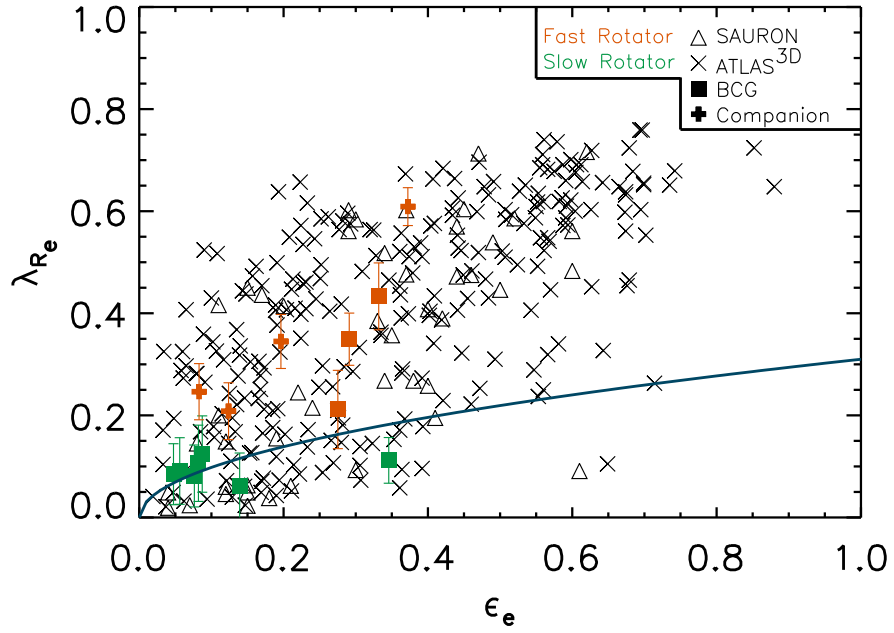


Figure 2.6: Angular Momentum vs. Ellipticity at the Effective Radius. SAURON galaxies are plotted as triangles, ATLAS^{3D} galaxies are plotted as crosses, BCGs from this study are plotted as squares, and Companion galaxies from this study are plotted as plus symbols. The blue line indicates the division between fast rotating and slow rotating galaxies. We find that three BCGs (1048, 1153, 1261) and four companions (1027, 1066, 1048) are classified as fast rotators.

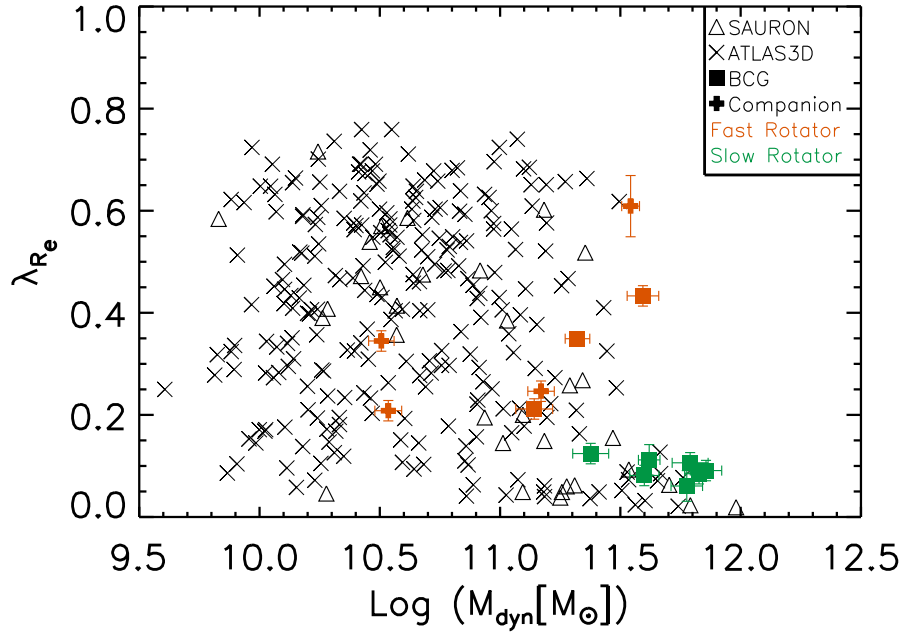


Figure 2.7: Angular Momentum vs. Dynamical Mass. SAURON galaxies are plotted as triangles, ATLAS^{3D} galaxies are plotted as crosses, BCGs from this study are plotted as squares, and Companion galaxies from this study are plotted as plus symbols. The galaxies presented here are amongst the most massive studied. An upper mass limit to fast rotating galaxies can be seen in all samples around approximately $M_{dyn} = 10^{11.5} M_{\odot}$.

have plotted λ_{Re} as a function of dynamical mass. We also plot dynamical masses from the SAURON survey (Emsellem et al., 2007) and derived dynamical masses from the reported ATLAS^{3D} velocity dispersions (Cappellari et al., 2013). Figure 2.7 shows that the majority of the galaxies reported in this study fall on the high mass end of the ATLAS^{3D} survey sample. Eight galaxies in our sample have dynamical masses above $10^{11.5}M_{\odot}$. In the SAURON and ATLAS^{3D} results there appears to be a ceiling at approximately $M_{dyn} = 10^{11.5}M_{\odot}$ at which point galaxies were much less likely to be classified as fast rotators (3/13 (23%) in Emsellem et al. (2011)). In agreement with the findings of the ATLAS^{3D} survey, we find that only 25% of galaxies in our sample above $10^{11.5}M_{\odot}$ are classified as fast rotating.

Table 2.2: Kinematic Properties of BCGs and Companions

Galaxy	R_e (") ± 0.01	Redshift ± 0.0001	σ_e (km s $^{-1}$)	Log(M) (Log(M_\odot)) ± 0.01	ϵ_e ± 0.01	λ_{Re}	FR/SR
1027 BCG*	6.98	0.0900	227 ± 7	11.79	0.08	0.12 ± 0.08	SR
1027 Comp*	4.39	0.0909	190 ± 6	11.17	0.08	0.24 ± 0.06	FR
1042 BCG	7.22	0.0947	227 ± 7	11.83	0.05	0.08 ± 0.06	SR
1048 (A4) ¹ BCG*	5.17 (3.40) ¹	0.0774	319 ± 7	11.59	0.33	0.46 ± 0.06	FR
1048 Comp	1.08	0.0801	167 ± 3	10.51	0.20	0.34 ± 0.05	FR
1048 Comp	1.24	0.0746	124 ± 3	10.54	0.12	0.21 ± 0.06	FR
1050 BCG	8.43	0.0722	291 ± 11	11.78	0.14	0.07 ± 0.07	SR
1066 BCG*	5.07	0.0838	186 ± 9	11.62	0.35	0.12 ± 0.05	SR
1066 Comp*	11.25	0.0836	176 ± 13	11.55	0.37	0.60 ± 0.04	FR
1153 BCG	2.39	0.0591	226 ± 7	11.14	0.28	0.21 ± 0.08	FR
1261 BCG	5.76	0.0371	271 ± 1	11.32	0.29	0.35 ± 0.05	FR
2001 BCG	5.84	0.0415	200 ± 4	11.38	0.09	0.13 ± 0.07	SR
2039 BCG	8.82	0.0829	248 ± 6	11.86	0.06	0.10 ± 0.07	SR
2086 BCG*	4.83	0.0839	203 ± 7	11.60	0.08	0.09 ± 0.06	SR

Kinematic results from a combination of IDL routines. R_e is derived from photometric results, but listed here as it is relevant to many values calculated in this table. (*) Galaxies with an asterisk next to their name are gravitationally bound to their neighboring galaxy.

¹ The effective radius reported in parenthesis for BCG 1048 is for component A4 only, and not the entire BCG.

2.4.4 Photometry

In order to perform our analysis of the spectroscopic data, we have to also examine the photometric data in order to determine the effective radius of each galaxy. The single component de Vaucouleurs models produced by GALFIT and residual images can be seen in Figure 2.8. In Figure 2.8 one can also see the tidal tails (BCG 1027) and multiple cores (BCG 1048) which motivated us to search for a quantifiable way to measure recent and ongoing mergers. We find that a single de Vaucouleurs profile is unable to properly model BCG 1048, and the residual image shows multiple hidden cores. To properly model BCG 1048, we instead use 4 spatially separated de Vaucouleurs profiles. We report both the single de Vaucouleurs results as well as the results for component A4, brightest of the 4 profiles, in parenthesis in Tables 2.2 and 2.3.

2.4.4.1 $G - M_{20}$ Analysis

The $G - M_{20}$ analysis searches for irregularities in the distribution of light which correlate to morphological signatures of merging. Our $G - M_{20}$ analysis is performed using PyMorph. For a galaxy to be classified as a merger candidate it must have

$$G > -0.14M_{20} + 0.33 \quad (2.4)$$

(Lotz et al., 2008). As can be seen in Table 2.3, BCG 1048 (FR) is confirmed to be a merger case by the $G - M_{20}$ selection criteria, as is BCG 2086 (SR). The other merging candidates are companions to BCGs 1027 (SR), 1066 (SR), and 2086 (SR).

BCG 1261, our fastest rotating galaxy, shows no signs of merging in the $G - M_{20}$ classification. According to Lotz et al. (2011), for our gas-poor galaxies, this suggests no recent mergers within the last 0.2 Gyrs by the $G - M_{20}$ classification. That would

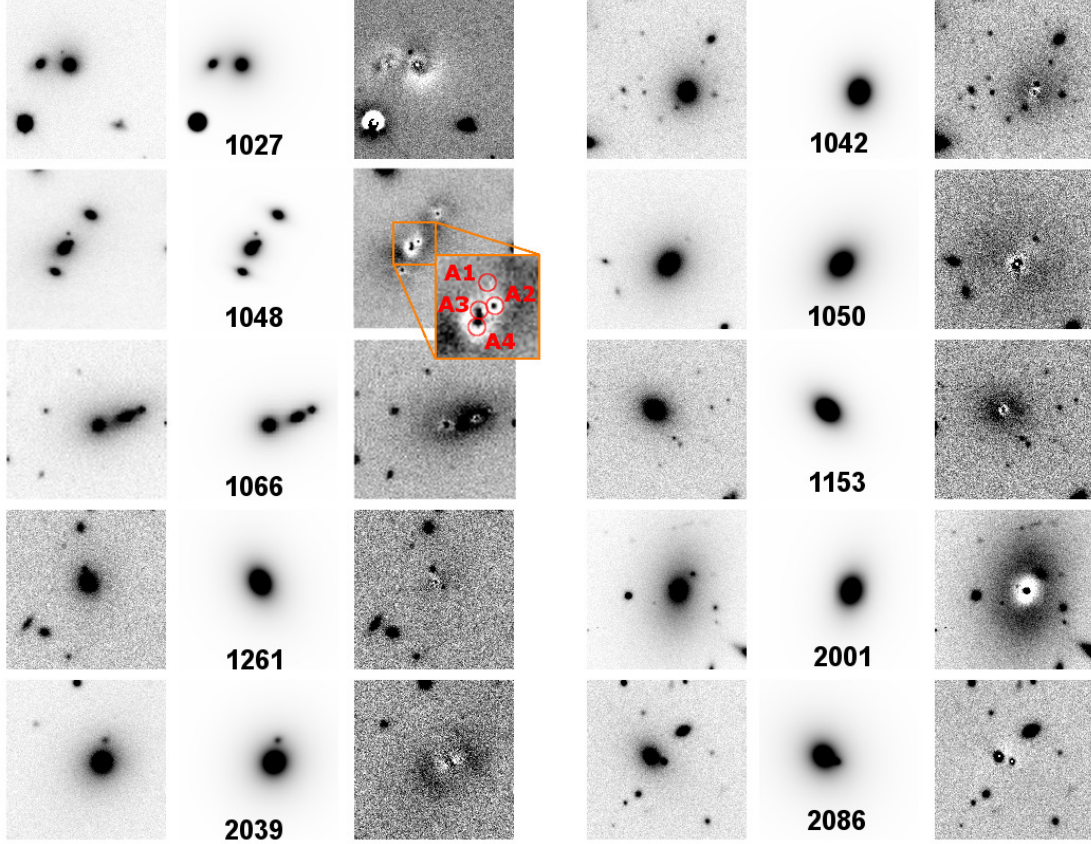


Figure 2.8: Single Component de Vaucouleurs Fits to BCG Photometry. Photometric SDSS r-band images of each galaxy is shown on the left hand side for each set. The middle image is the best fitting de Vaucouleurs model produced by GALFIT, and the right hand side of each set shows the residuals after the GALFIT model has been subtracted from each galaxy. Each image is $60'' \times 60''$. BCG 1048 (FR) is shown modeled by 4 de Vaucouleurs profiles labeled A1-A4 with the center of each profile indicated by the red circles. Excess light can be seen between components A3 and A4. Excess light can also be seen in the outskirts of BCGs 1027 (SR), 1048 (FR), 1066 (SR), and 2001 (SR), suggesting on-going or very recent merger event.

Table 2.3: Photometric Properties of BCGs and Companions

Galaxy	R_e (") ± 0.01	Integrated Magnitude ± 0.01	G ± 0.01	M_{20} ± 0.01	Merging?
1027 BCG*	6.98	16.11	0.568	-1.80	n
1027 Comp*	4.39	17.38	0.574	-1.69	y
1042 BCG	7.22	16.47	0.602	-2.26	n
1048 (A4) ¹ BCG*	5.17 (3.40) ¹	16.47 (17.07) ¹	0.609	-1.85	y
1048 Comp	1.08	18.10	0.593	-2.11	n
1048 Comp	1.24	17.60	0.604	-2.03	n
1050 BCG	8.43	15.31	0.616	-2.40	n
1066 BCG*	4.95	16.95	0.617	-2.21	n
1066 Comp*	11.95	17.05	0.613	-1.83	y
1153 BCG	2.39	17.22	0.626	-2.35	n
1261 BCG	5.76	17.36	0.576	-2.38	n
2001 BCG	5.84	15.75	0.527	-2.20	n
2039 BCG	8.82	15.63	0.559	-2.17	n
2086 BCG*	4.83	16.95	0.652	-1.37	y

Photometric results from Source Extractor, GALFIT, and PyMorph. The effective radius and integrated magnitude come from the de Vaucouleurs fits, where as the Gini and M_{20} values come from PyMorph. (*) Galaxies with an asterisk next to their name are gravitationally bound to their neighboring galaxy.

¹The effective radius reported in parenthesis for BCG 1048 is for component A4 only, and not the entire BCG.

suggest that any mergers with this $z = 0.04$ galaxy would have had to happen before $z = 0.06$.

Therefore, 40% (4/10) of the systems in our sample show morphological signs of current or very recent mergers. Based on the original unbiased sample of 625 BCGs from von der Linden et al. (2007), we find a lower limit of $0.64 \pm 0.32\%$ of BCGs are currently undergoing or have undergone a merger within the last 0.2 Gyrs. Although this subsample is biased towards merging galaxies and not representative of the entire BCG sample, we consider it significant that it is consistent with simulations of BCGs from De Lucia and Blaizot (2007) that showed a 1.47% merger rate within the same 0.2 Gyrs time period (assuming a constant merger rate from $z = 0.5$ to $z = 0$) as well as observational results from Liu et al. (2009) that showed a 0.63% BCG major

merger rate within 0.2 Gyrs (assuming a constant merger rate from $z = 0.12$ to $z = 0.03$).

2.4.5 Boundedness

By utilizing the information from both the photometric and the kinematic results, we are able to determine whether the companion galaxies are likely to be bound to the BCG. The criteria for being gravitationally bound is

$$V_r R_p \leq 2GM \sin^2 \alpha \cos \alpha \quad (2.5)$$

(Beers et al., 1982). V_r is the radial velocity offset between the two galaxies, R_p is the projected radial separation between the two galaxies, M is the dynamical mass, G is the gravitational constant, and α is the angular separation between the two galaxies. By integrating over all possible values of α , we can find the probability that a companion galaxy will be gravitationally bound to the BCG.

The same analysis was performed by Brough et al. (2011) for BCGs 1027, 1066, and 2086, in which they found that systems 1027 and 1066 were likely to be bound, but 2086 was not. In performing our analysis, we find that indeed the companion to BCG 1027 has a 65% chance of being bound, the companion to BCG 1066 has a 94% chance of being bound, and the companion to BCG 2086 has a 56% chance of being bound. We also find in addition that the two outer companions to BCG 1048 (1048 B and 1048 C) never cross the threshold outlined in Equation 2.5 and are therefore unlikely to be bound to BCG 1048 A. As seen in Figure 2.8, BCG 1048 A is comprised of 4 components, the most massive being 1048 A2, A3, and A4 which together make up the galaxy which we call BCG 1048. We find that component 1048 A3 has an 80% chance of being bound to 1048 A4.

2.5 Discussion

Since the formation history of BCGs is not completely understood, and is in some places contradictory, this research provides vital clues to solving this mystery. If BCGs form via mostly dry minor mergers where up to half of their mass is accreted isotropically, then most of the initial angular momentum will be removed and we would not expect to see very massive BCGs with high values of λ_{Re} . If however there are many major merger events with similar orbital parameters to cause a higher angular momentum in the newly formed galaxy despite the lack of gas, then large scale rotation could still be present today. A third possibility is that there is no connection between merger history and a galaxy's classification as a fast or slow rotator, in which case we would have to look for an outside cause to remove angular momentum.

2.5.1 Mergers and Rotation

From the combination of kinematic and photometric results, it appears that BCGs have diverse recent merging histories. This is unexpected considering their similarities in luminosities and stellar population. BCGs 1261, 1048, and 1153 are our highest λ_{Re} BCGs and it appears that their high λ_{Re} values come from different sources. Simulations show that very gas-rich major mergers (Cox et al. 2006, Robertson et al. 2006) and certain gas-poor major mergers (Bois et al., 2011) produce fast rotating galaxies. Since we do not see any evidence for gas emission lines in any of the galaxies in our sample, we assume that they are still gas-poor. Below we will discuss specific examples of the various combinations of merging and angular momentum, demonstrating that there is little correlation between the two observables (Figure 2.9).

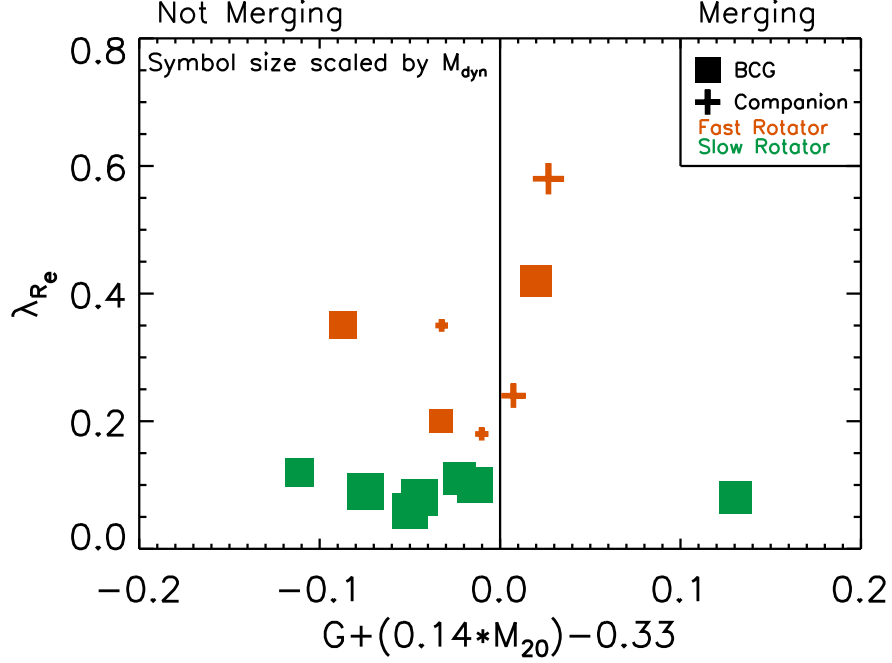


Figure 2.9: Merger Status and Angular Momentum at the Effective Radius. BCGs are plotted as squares, and companions are plotted as crosses. Plot symbols are scaled according to galaxy mass, with a larger symbol indicating a higher dynamical mass. Plot symbols are also color coded, with orange indicating a fast rotating galaxy, and green indicating a slow rotating galaxy. Galaxies plotted on the negative side of the x-axis are classified as not merging by the $G - M_{20}$ criteria, galaxies on the positive side of the x-axis are classified as merging. There appears to be no correlation between Merging and λ_{Re} .

2.5.1.1 *Fast Rotators with No Mergers*

BCGs 1261 & 1153 are both fast rotators with no evidence of recent mergers. The photometry for these fast rotating galaxies as measured by $G - M_{20}$ indicates a quiet recent merger history, i.e. no major dry merger events within the last ~ 0.2 Gyrs (Lotz et al., 2011), and no currently occurring mergers. With our limited timescale we do not have enough information to determine how these fast rotating but very massive BCGs formed. An analysis of these merger quiet fast rotating BCGs' stellar population would determine whether or not these BCGs are indeed dominated by old stellar populations.

2.5.1.2 *Fast Rotators with Mergers*

The counterpoint to our fast rotating, quiet history BCGs is BCG 1048 (FR), which is currently undergoing a minor merger. The multiple cores (A1-A4) present in BCG 1048 (Figure 2.8) suggest an ongoing dry minor merger event, which is coincident with the high λ_{Re} value we measure. This is further supported by the $G-M_{20}$ selection of BCG 1048 A1-4 as a merging system and the high likelihood that the system is bound. It is uncertain whether or not the high λ_{Re} value observed in BCG 1048 is the result of actual stellar rotation, or merely the result of having a slightly blue shifted core located near a slightly redshifted core as we do not see the same clear velocity gradient as observed in BCG 1261 (FR).

In order to properly model BCG 1048 (FR) in GALFIT, we require 4 spatially separated components. By summing the light coming from each model component and assuming that the M/L ratio is the same across the entire BCG, we find evidence for a minor 1:8 merger taking place between A3 and A4. The other two inner companions, A1 and A2, have mass ratios of approximately 1:8 (A2) and 1:30 (A1) as compared to the central brightest core (A4). We also find that neither of the outer

companion galaxies cross the threshold to be bound to the central merging BCG system for any value of α , and they are unlikely to merge in the future. Despite the fact that the two outermost companions will not merge, the excess light between components A2, A3, and A4 in the central core still shows that this system is actively merging and accreting matter.

For close merging galaxies such as BCG 1048, it is reasonable to question whether the observed kinematic properties, such as velocity dispersion, are artificially inflated by the ongoing merger. Considering this complication, it is likely that determinations of λ_{Re} for merging systems would not be a robust quantity, and that it may change throughout the merging process. The measured ellipticity is also likely to be affected during the merging process, causing the BCG to appear to be more elliptical because we are observing two galaxies superimposed upon each other. However artificially inflating the ellipticity would only serve to increase the threshold for it to be considered a fast rotating galaxy, and would not accidentally classify a slow rotating galaxy as a fast rotating galaxy.

2.5.1.3 Slow Rotators without Mergers

Our slow rotating galaxies have a similarly mixed merging history. We see that BCGs 1042, 1050, 2001, and 2039 are slow rotators with no evidence of a recent merging event in the $G - M_{20}$ classification, although BCGs 2001 (SR) and 2039 (SR) show a significant amount of enhanced intra-cluster light. As our results are limited to within $1R_e$, we are uncertain if it is just the core that is slowly rotating, or if the outer halo is similarly slowly rotating. IFU measurements of the extended discs seen in BCGs 2001 (SR) and 2039 (SR) could help confirm the results of Bournaud et al. (2004) in which they found that mergers tend to redistribute angular momentum to the outer regions of a galaxy.

2.5.1.4 *Slow Rotators with Mergers*

BCGs 1027, 1066, and 2086 are slow rotating galaxies currently undergoing a minor merging event according to the $G - M_{20}$ criteria. All three companions were found to have a more than 50% chance of being bound to the BCG, adding evidence to the possibility of a minor merger in the future. Although we do not have enough spaxels with S/N over 10 to determine the rotation of the companion galaxy to BCG 2086, both BCGs 1027 and 1066 are slow rotating BCGs with a fast rotating companions. BCG 1027 (FR) exhibits tidal tails in the residual photometry, a slight velocity gradient seen in the BCG, and more extreme rotation seen in the companion. The companion to BCG 1066 (SR) is also a fast rotating galaxy, and appears under visual inspection of the residuals to have two cores, much like the case of BCG 1048 (FR).

2.5.2 *Companion Rotation*

Companions of BCGs 1066, 1027, and 1048 show clear signs of rotation, both visually and in their λ_R results. Every BCG companion that we have sufficient data to measure λ_R is a fast rotating galaxy. Although we have a limited number of spaxels to measure the rotation in BCG 1066, the analysis presented in Brough et al. (2011) provides more spaxels, showing that both companions of 1066 and 1027 are fast rotators. Our data indicates that all elliptical galaxies near BCGs are fast rotators, however we have an admittedly small sample size of only 4 companion galaxies to make that determination.

2.5.3 *Angular Momentum and Dynamical Mass*

The presence of fast rotating BCGs in our sample was quite unexpected considering our initial assumption that BCGs should be mostly dispersion supported.

Although, when comparing our measurements of λ_{Re} and M_{dyn} in BCGs to the SAURON and ATLAS^{3D} samples of early-type galaxies (Figure 2.7), we find that our sample is generally consistent with their results. There appears to be a limit around $M_{dyn} = 10^{11.5} M_{\odot}$ above which there are virtually no galaxies with a high angular momentum, independent of whether they are BCGs or not. The two galaxies that we do find slightly above this limit are both within 1σ , and both currently in the process of merging, causing some doubt that they are actually as massive as measured.

In observing these very massive galaxies, in extreme environments, at distances further than what had been measured before, our results suggest that λ_{Re} would be influenced more by a galaxy’s dynamical mass than its location within a cluster, and that this is consistent across samples of galaxies that were selected using differing criteria. The SAURON and ATLAS^{3D} surveys focused on early-type galaxies in general and measured only one BCG, whereas we examined a sample of 10 BCGs at higher redshift. Larger galaxies likely formed as a result of more mergers than smaller galaxies, therefore they have a higher likelihood of losing their initial angular momentum. Peng et al. (2010) have also shown that above $M_{*} = 10^{11} M_{\odot}$ there is a change in the ratio of galaxy mass assembled via post quenched galaxy mergers, also suggesting that these dry merging events could be responsible for removing the angular momentum.

Conversely, Martizzi et al. (2012) have used simulations to show that AGN are a possible mechanism for removing angular momentum from large galaxies. Having shown in our sample examples of dry mergers that exhibit a high λ_{Re} measurement, it is possible that a different process, such as AGN, are responsible for turning fast rotating galaxies into slow rotators. It would be interesting and relatively straightforward to test for the presence of the $M_{dyn} = 10^{11.5} M_{\odot}$ limit for fast rotators observed

within these samples using such simulations, and to see if the presence of AGN in simulations has any effect on the reproducibility of this limit.

In a further study using higher resolution photometry, we would like to measure which galaxies are cuspy and which are cored as in Lauer (2012). It is possible that AGN are responsible for both building the core, as well as removing angular momentum at the same time. Initial results suggest that our sample of galaxies follow the same relationship seen in the ATLAS^{3D} sample, in that all cored galaxies are slow rotators, but not all slow rotators are cored. However higher resolution photometry than the SDSS imaging is needed in order to properly make the cuspy/cored determination.

Also in Lauer (2012) they discuss the possibility that the division between fast and slow rotators should be set at a constant $\lambda_{Re/2} = 0.25$. Using this alternative selection criteria, we would find 2 fast rotating BCGs (20%), and 2 fast rotating companion galaxies (50%). Under this higher threshold, the main message of our results would change little. The majority of the BCGs that we studied would be slow rotating, however we would still find fast rotating BCGs. Similarly, 25% of the galaxies we studied above $M_{dyn} = 10^{11.5} M_{\odot}$ would continue to be fast rotators.

Another possible issue to consider is that in some cases, such as BCG 1048 and the companion to BCG 1066, the galaxies contain multiple cores from ongoing mergers, which could cause the λ_{Re} measurements to be artificially inflated. This would also artificially increase our measurements of M_{dyn} . It is also possible that our measurements for λ_{Re} for these galaxies will shift as they become dynamically relaxed post-merger. An examination of λ_{Re} values pre-merger, peri-merger, and post-merger in simulations may shed light on how much of an effect dry mergers would have on λ_{Re} results. In our analysis, we consider these merging systems, such as BCG 1048 and Companion 1066 to be one galaxy because they are currently in the process of

merging.

2.5.4 Cluster Rotation

Another factor to consider would be the angular momentum of the cluster as a whole. If the angular momentum of a BCG at the kinematic center of a cluster coincides with the average angular momentum of the entire cluster, then infalling galaxies merging with the BCG would likely contribute to the angular momentum of the BCG instead of subtracting from it. It would be interesting to study the angular momentum of the whole cluster of our best example of a fast rotating BCGs, such as 1261, to see if the angular momentum of the cluster aligns with the angular momentum of the BCG. Such measurements would require new observations with a much wider field-of-view. An instrument such as SAMI (Croom et al., 2012) with deployable fiber bundles would allow us to collect IFU observations of spatially separated objects across a much wider field of view, e.g. to observations beyond $1R_e$ for many of the galaxies in our sample.

We have observed that BCGs are surprisingly diverse in their photometric and kinematic properties. We intend to continue our study of these BCGs by conducting an analysis of their stellar populations in order to further understand their merger history.

2.6 Conclusion

In this study we present 2D kinematic and photometric maps of Brightest Cluster Galaxies, ranging in redshift from $z = 0.04$ to $z = 0.09$ (Figures 2.2, 2.3, and 2.8). BCGs are expected to undergo more dry minor mergers than a typical elliptical galaxy, and dry minor mergers have been shown in simulations to decrease a galaxy's angular momentum (Bournaud et al. 2007, Jesseit et al. 2009, Bois et al. 2010, Bois et al. 2011). As the result of many dry minor mergers, we do not expect BCGs to

be fast rotating galaxies (as defined by ATLAS^{3D}; Emsellem et al. 2011). We use our sample of 10 BCGs (selected from the SDSS-C4-DR3 catalogue (Miller et al., 2005) of BCGs with companions within $10''$) and their companions to search for a connection between angular momentum, dynamical mass, and very recent merger history.

Using observations from the VIMOS IFU spectrograph (Le Fèvre et al., 2003) on the VLT we calculate the λ_R values that act as a proxy for angular momentum (Emsellem et al., 2007) (Figure 2.5). We measure λ_{Re} , λ_R at $1R_e$, and find λ_{Re} values ranging from 0.07 ± 0.07 to 0.60 ± 0.04 out of a possible range 0.0 to 1.0 (Figure 2.6). We have shown that 30% (3/10) of BCGs show signs of galaxy scale rotation and fit the ATLAS^{3D} definition of a fast rotating galaxy and the other 70% of our BCGs are slow rotating galaxies. We find the rather surprising result that 100% (4/4) of our companion galaxies are fast rotating.

Using velocity dispersion (Figure 2.4) derived from Equation 2.3, we calculate M_{dyn} for our sample of galaxies, finding dynamical masses up to $M_{dyn} = 10^{11.9} M_\odot$. BCGs are some of the most massive galaxies in the universe, and the BCGs in our sample are among the most massive galaxies to have their angular momentum calculated using λ_R (Figure 2.7).

While we do find a small number of fast rotating BCGs (Figure 2.7), we find fewer fast rotating galaxies above $M_{dyn} = 10^{11.5} M_\odot$, consistent with the previous limit for fast rotating galaxies in the SAURON and ATLAS^{3D} sample (Emsellem et al. 2007, Cappellari et al. 2013). There appears to be an upper limit to how massive a galaxy can be while still maintaining a high angular momentum. The consistency between our results and that of the ATLAS^{3D} survey suggests that a galaxy's mass may be more significant than its position inside a cluster halo in determining angular momentum.

Next we examine the ongoing and recent merging history of the galaxies in our sample using the $G - M_{20}$ merger selection criteria (Lotz et al., 2008). We see that 40% (4/10) of systems in our sample are currently undergoing or have undergone a merger within the last 0.2 Gyrs (Figure 2.9). Although our sample selection is biased towards BCGs that have companions, based on the original unbiased sample of 625 BCGs (von der Linden et al., 2007), we find that at least $0.64 \pm 0.32\%$ of BCGs are undergoing a merger, consistent with observations of BCGs by Liu et al. (2009). We use these merging results to examine the connection between λ_{Re} and $G - M_{20}$.

We find no correlation between λ_{Re} and $G - M_{20}$. We find in 1 BCG that the minor merger event is likely responsible for the high λ_{Re} value observed in the BCG and its companions. Conversely we find 2 BCGs that are fast rotating without any recent or ongoing merger events. In the slow rotating BCG category we find 3 mergers connected to a slow rotating BCG, and 4 examples of slow rotating BCGs without any mergers.

These diverse characteristics suggest that there is no strong connection between recent dry mergers and the λ_{Re} classification as a fast or slow rotator. It is possible that complications from an unrelaxed dynamical system have skewed λ_{Re} measurements in merging systems, or that the removal of angular momentum is due to some other physical process (such as AGN; Martizzi et al. 2012) and not predominately due to mergers. Increased resolution photometry would allow us to measure the cores of these galaxies to see if they are either cusp or cored in order to test the hypothesis of Lauer (2012).

These surprising results provide clues as to the formation history of Brightest Cluster Galaxies. It would be beneficial to have an increased sample of BCGs to add to our results, especially BCGs with companions, and more measurements of the companions to determine the probability of a bound BCG companion being a

fast rotator. A larger sample size would also allow us to investigate the possible limit above which fast rotating galaxies do not exist. Further studies of the ages of the stellar population of seemingly merger quiet galaxies would assist us in understanding their merger histories beyond 0.2 Gyrs. Our observations lead us to conclude that there is much diversity in the measurements of a BCG's angular momentum, dynamical mass, and merger history (Figure 2.9).

3. THE GAS PHASE MASS METALLICITY RELATION FOR DWARF GALAXIES: DEPENDENCE ON STAR FORMATION RATE AND HI-GAS MASS*

3.1 Synopsis

Using a sample of dwarf galaxies observed using the VIMOS IFU on the VLT, we investigate the mass-metallicity relation (MZR) as a function of star formation rate (FMR_{SFR}) as well as HI-gas mass (FMR_{HI}). We combine our IFU data with a subsample of galaxies from the ALFALFA HI survey crossmatched to the Sloan Digital Sky Survey to study the FMR_{SFR} and FMR_{HI} across the stellar mass range $10^{6.6}$ to $10^{8.8} M_{\odot}$, with metallicities as low as $12+\log(\text{O}/\text{H}) = 7.67$. We find the 1σ scatter of binned means in the MZR to be 0.05 dex. The 1σ scatter of binned means in the FMR_{SFR} (0.02 dex) is significantly lower than that of the MZR. The FMR_{SFR} is not consistent between the IFU observed galaxies and the ALFALFA/SDSS galaxies for SFRs lower than $10^{-2.4} M_{\odot} \text{ yr}^{-1}$, however this could be the result of limitations of our measurements in that regime. The lowest scatter of binned means (0.01 dex) is found in the FMR_{HI} . We also find that the FMR_{HI} is consistent between the IFU observed dwarf galaxies and the ALFALFA/SDSS crossmatched sample. We introduce the fundamental metallicity luminosity counterpart to the FMR, again characterized in terms of SFR (FML_{SFR}) and HI-gas mass (FML_{HI}). We find that the FML_{HI} relation is consistent between the IFU observed dwarf galaxy sample and the larger ALFALFA/SDSS sample. However the 1σ scatter for the FML_{HI} relation is not improved over the FMR_{HI} scenario. This leads us to conclude that the FMR_{HI}

*Reprinted with permission from “The Gas Phase Mass Metallicity Relation for Dwarf Galaxies: Dependence on Star Formation Rate and HI-Gas Mass” by Jimmy et al., 2015. The Astrophysical Journal, Volume 812, Issue 2, article id. 98, 21 pp., Copyright 2015 by the American Astronomical Society.

is the best candidate for a physically motivated fundamental metallicity relation.

3.2 Introduction

The mass-metallicity relation (MZR) is an important tool for understanding the underlying processes of galaxy formation. A galaxy’s metal content provides insights into the history of star formation within a galaxy. Lequeux et al. (1979) and Kinman and Davidson (1981) first reported on the correlation between galaxy stellar-mass and gas-phase metallicity. Later studies confirmed the relation using the Sloan Digital Sky Survey (SDSS) for large number statistics (Tremonti et al., 2004; Kewley and Ellison, 2008; Michel-Dansac et al., 2008; Salim et al., 2014). Other studies have focused on the redshift evolution of the MZR (Savaglio et al., 2005; Erb et al., 2006; Cowie and Barger, 2008; Liu et al., 2008; Maiolino et al., 2008; Panter et al., 2008; Rodrigues et al., 2008; Hayashi et al., 2009; Mannucci et al., 2009; Pérez-Montero et al., 2009; Cresci et al., 2012).

The luminosity-metallicity relation (LZR) has also been proposed as a relation of merit (Skillman et al., 1989; Garnett, 2002; Pérez-González et al., 2003; Pilyugin et al., 2004; Lee et al., 2006). The advantage of the LZR is that reliable luminosity measurements are generally easier to obtain than reliable stellar mass estimations. The disadvantage of the LZR is that it is dependent upon the bandpass being used, and could be affected by dust extinction (Salzer et al., 2005). The LZR is observed to hold over a range of 10 magnitudes in galaxy optical luminosity (Zaritsky et al., 1994; Tremonti et al., 2004; Lee et al., 2006). The MZR and the LZR reveal that some physical mechanism must be driving a correlation between stars, metals, and gas flows across a vast range of scales. However, the exact physical mechanism(s) responsible for forming this relation are still uncertain.

Recent studies have investigated the mass-metallicity relation with a particular

focus on low stellar-mass or low-luminosity systems (Berg et al., 2012; Nicholls et al., 2014; Haurberg et al., 2015; McQuinn et al., 2015; James et al., 2015), which is the population of galaxies of interest to this work. The MZR is known to exhibit scatter greater than would be expected by the uncertainties on the individual data points (Tremonti et al., 2004; Lara-López et al., 2010; Mannucci et al., 2010).

To explain this apparently enhanced scatter, it has been suggested that the MZR has a dependence on Star Formation Rate (SFR; Lara-López et al., 2010; Mannucci et al., 2010; Andrews and Martini, 2013), which could alternatively be explained as a dependence on HI-gas content (Bothwell et al., 2013; Lara-López et al., 2013). This 3 dimensional extension of the mass-metallicity relation is known as the fundamental metallicity relation (FMR). The FMR has been shown to be consistent, with little evolution, up to a redshift of 2.5 (Lara-López et al., 2010; Mannucci et al., 2010). It is currently uncertain as to which observable (HI-gas mass or SFR) better explains the scatter in the MZR, or if some other unknown parameter is responsible.

Several hypotheses have been proposed for the mechanisms that guide the FMR, such as pristine gas inflows diluting metal abundances (Finlator and Davé, 2008; Davé et al., 2010). Inflows of pristine gas would cause a galaxy to exhibit lower gas-phase metallicity than would be predicted by the FMR. Recent evidence suggests that infall of pristine gas is the more dominant component at high redshift (Agertz et al., 2009; Bournaud and Elmegreen, 2009; Brooks et al., 2009; Dekel et al., 2009).

As argued in Mannucci et al. (2010) infalling pristine gas must eventually ignite star formation, which will create strong supernova winds that will expel metals. Gas outflows expelling metal-rich gas into the interstellar medium provide an alternative explanation for the observed gas-phase metallicity being lower than the MZR prediction (Edmunds, 1990; Lehnert and Heckman, 1996; Garnett, 2002; Tremonti et al., 2004; Kobayashi et al., 2007; Scannapieco et al., 2008; Spitoni et al., 2008).

Studies on the FMR thus far, either as a function of SFR (FMR_{SFR}) or HI-gas mass (FMR_{HI}), have focused on the SDSS sample of spectroscopically observed galaxies (Lara-López et al., 2010; Mannucci et al., 2010; Bothwell et al., 2013). As such these galaxies are biased towards the intermediate to high stellar-mass galaxies that dominate the SDSS spectroscopic sample. However it is important to understand the low-mass galaxy population as well and to test whether or not they fall onto the same FMR.

Dwarf galaxies are the most common type of galaxies in the Universe, comprising $\sim 85\%$ of the objects in the volume within 10 Mpc (Karachentsev et al., 2004). Even though they are not as widely studied as their more massive counterparts, they may hold the answers to several fundamental questions concerning the processes of galaxy formation and evolution.

The data presented here consists of integral field unit (IFU) observations of a sample of 11 dwarf galaxies selected from the ALFALFA survey. ALFALFA is a blind HI survey of the local universe ($cz < 18,000 \text{ km s}^{-1}$; Haynes et al. 2011). The IFU observations were taken using the VIMOS IFU spectrograph on the Very Large Telescope (VLT).

To compliment the IFU observed dwarf galaxy dataset, we utilize a larger ALFALFA/SDSS cross-matched sample of spectroscopically observed galaxies. In addition we also include samples from the literature of low-mass/low-luminosity galaxies such as the Berg et al. (2012), long-slit spectroscopic observations of low-luminosity galaxies, the SHIELD survey of ALFALFA dwarf galaxies (Haurberg et al., 2015; McQuinn et al., 2015) and the James et al. (2015) long-slit morphologically selected survey of dwarf irregular galaxies.

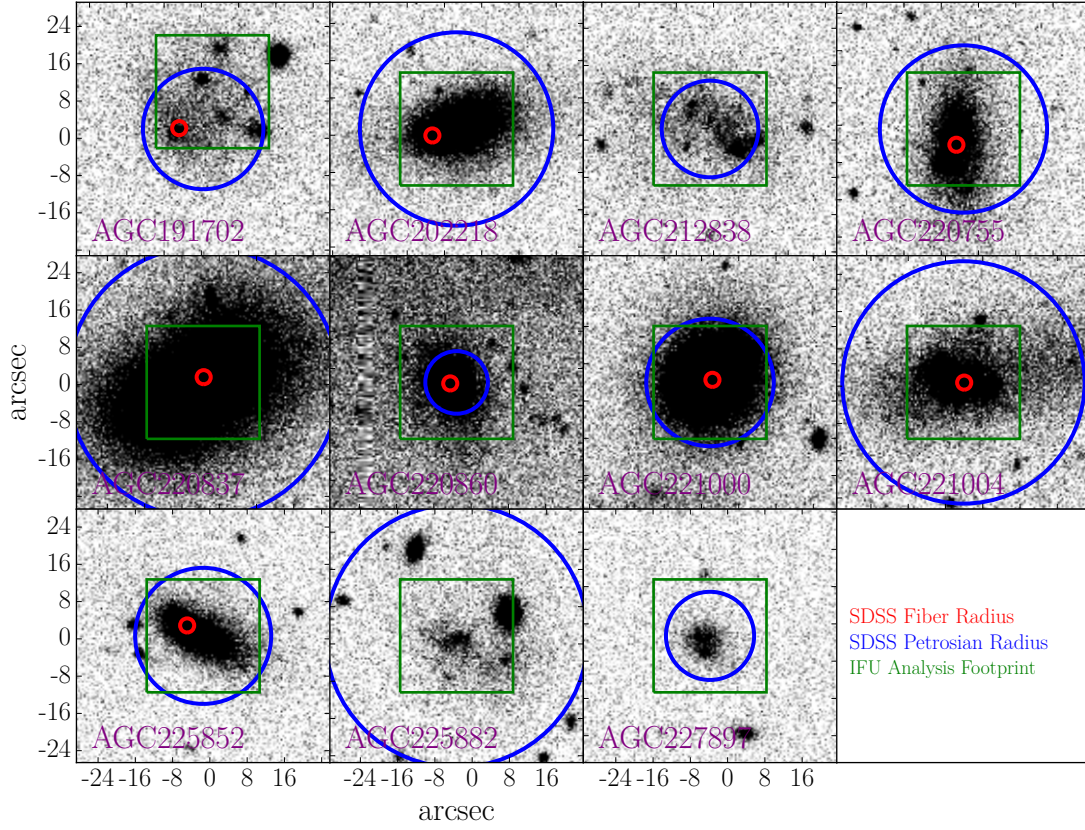


Figure 3.1: SDSS Images of Dwarf Galaxies. SDSS Images of Dwarf Galaxies. SDSS r -band images of the 11 galaxies presented in this study, demonstrating the need for IFU spectroscopy. The red circle indicates the location of the $3''$ SDSS fiber which would be used to obtain spectral information without IFU observations. The SDSS fiber often misses a considerable amount of light from the clumpy star-forming regions of these nearby dwarf galaxies. Shown in blue is the Petrosian radius as determined by the SDSS automated data reduction procedure. The SDSS photometry pipeline visibly overestimates or underestimates the flux in galaxies from this sample. Each thumbnail image is the size of the full VIMOS low resolution multiplexed field-of-view ($54'' \times 54''$). The green boxes indicate the subset of this field-of-view that our IFU analysis focuses on.

3.3 Sample

The IFU observed dwarf galaxy sample includes nearby ($D < 20\text{Mpc}$), low HI-gas mass ($M_{\text{HI}} < 10^{8.2}$), low surface brightness dwarf galaxies, selected to study the mass-metallicity relation on the low stellar-mass end. Due to the nature of observing nearby dwarf galaxies, IFU spectroscopy is vital to capture the properties of the entire galaxy. As can be seen in Figure 3.1, for the galaxies in our sample that have Sloan Digital Sky Survey (SDSS) fiber observations, the single SDSS fiber only captures a small portion of the galaxy’s flux, and the fiber may miss bright star forming regions (e.g. Richards et al. 2014), this would cause star formation rate estimations of nearby dwarf galaxies such as these to be inaccurate.

IFU observations also have the advantage of not requiring additional photometric observations to identify bright HII regions to target. Performing such observations using long-slit spectroscopy would require *a-priori* knowledge of the positions of HII regions which can be obtained from narrow-band $\text{H}\alpha$ images, introducing an optical bias in the otherwise HI-selected sample. The most metal poor galaxies are also likely to have the faintest HII regions, making them barely detectable in narrow-band images. Integrating over a larger surface area allows us to target fainter galaxies. Because the dwarf galaxies that we are trying to observe are so faint, only 6 galaxies in this sample have reliable SDSS spectroscopy. A purely SDSS based study, or a long-slit spectroscopy study are both likely to preferentially exclude the faintest dwarf galaxies.

3.3.1 Spectroscopic Observations

Spectroscopic data of 28 dwarf galaxies were initially taken using the VIMOS (Le Fèvre et al., 2003) IFU spectrograph on the Very Large Telescope (VLT) located at Paranal Observatory. Of the 28 observed galaxies, 11 have $\text{H}\alpha$ emission lines

greater than our amplitude over noise (AoN) cut of 5 for more than 20 spaxels and therefore are included in this study. Integration times for the remaining 17 galaxies were insufficient to reach our target depth. The data was obtained starting on April 11, 2008 and ending on May 19, 2010 under program IDs 081.B-0649(A) and 083.B-0662(A). Data was obtained using the VIMOS Low Resolution Blue Grism which has a wavelength range of 4000-6700 Å and a spectral resolution of 5.3 Å pixel⁻¹ (R \sim 1000).

Using the LR Blue grism provides the full 54"x54" field of view possible with VIMOS which allows us to obtain in a single pointing spectra across the complete stellar disk of each galaxy. Each object was observed using a 3 dither pattern, with each dither being integrated for 20 minutes. Average seeing across all observations is 1.05" FWHM.

The LR blue grism provides both a wider spectral range, and a wider field of view when compared to the HR blue grism. The LR grism wavelength range allows for simultaneous observations of the emission lines from H β ($\lambda = 4861$) to [NII] ($\lambda = 6583$). The major drawback to using the low-resolution spectra (~ 5.3 Å pixel⁻¹) is that we are unable to measure gas kinematics from the emission lines and the instrumental dispersion causes the H α and [NII] $\lambda\lambda = 6549, 6583$ Å emission lines to blend together.

The spectroscopic data obtained with the VIMOS IFU is reduced from its raw form using the Reflex environment for ESO pipelines (Freudling et al., 2013). The standard VIMOS template is used within the Reflex environment to produce the master bias and calibration frames containing the fiber traces and wavelength solution. Many of the raw data and calibration frames contain a bright artifact across the surface of the chip, identified to be an internal reflection within the instrument. This contamination interferes with the wavelength calibration routine within Reflex

because it is often misidentified as a skyline, causing the spectrum to be shifted incorrectly. In order to compensate, we disable the skyline shift in the calibration steps. The wavelength solution provided by the ESO pipeline proved to be accurate without using the skyline shift. We also use the flux standardization routine within the Reflex VIMOS pipeline. We then apply the calibrations frames to the science frames to produce the fully reduced Row-Stacked Spectra (RSS).

The final output of the Reflex pipeline is four quadrants per observation. We input these individual RSS quadrants into routines written in IDL and Python¹. These routines fit Gaussian curves to the skylines and subtract the sky background while retaining the flux information from each skyline to normalize the transmission of each spaxel across the entire field of view. After the normalization and sky subtraction steps are completed, the two dimensional RSS are converted into three dimensional data cubes. These data cubes consist of two spatial dimensions with the wavelength axis being the third dimension. Further details of the process these scripts follow can be found in Jimmy et al. (2013).

Once the data cubes have been built, the individual dithers (typically 3 per galaxy) are stacked using a 5σ clipped mean. We use the AoN to select for spaxels containing sufficient emission line flux for oxygen abundance estimations. AoN is defined as the amplitude of the emission line divided by the noise after the linear offset is subtracted. An AoN threshold of 5 is used to identify spaxels which contain emission lines for gas-phase metallicity analysis. Only spaxels which pass the AoN cut in all of the three following lines are included in the integrated spectrum for oxygen abundance estimations: $H\beta$ $\lambda = 4861$, $[OIII]$, $\lambda = 5007$, $H\alpha$ $\lambda = 6563$. We do not require $[NII]$ $\lambda = 6583$ to be separately detected because it is blended with $H\alpha$ (Figure 4.1).

¹Available publicly: <http://jimmy.pink/#code>

All spaxels which pass our AoN cut are then fed into Python based Gaussian fitting routines to measure the emission line flux ratios for gas-phase metallicity estimations. To obtain the integrated spectrum used to derive oxygen abundances, we sum the spectra from each spaxel that passes the AoN cut to produce a single spectrum that we perform this analysis upon. We chose to write our own routines instead of using a publicly available program such as GANDALF (Sarzi et al., 2006). Because GANDALF fits the stellar continuum and emission lines simultaneously, GANDALF is unable to fit robustly the weak stellar continuum in the dwarf galaxies.

Using an AoN cut is necessary because a significant fraction of the spaxels in the data cubes are excessively noisy, and including them in the integrated spectrum would significantly reduce the signal-to-noise ratio. Unfortunately the AoN cut causes us to discard a number of spaxels containing $H\alpha$ flux, resulting in an underestimate of the SFR. In order to ensure that we capture all of the $H\alpha$ flux, we use the segmentation images described in Section 3.3.2 to select spaxels belonging to a galaxy. We rescale and rotate the segmentation map to match the VIMOS data cube using the IDL routine HASTROM.PRO³. The integrated spectra obtained using the segmentation map selection is used to measure $H\alpha$ flux for the purposes of determining the SFR for each galaxy.

3.3.1.1 *Emission Line Fitting*

The basic procedure that our Python based Gaussian fitting routines follows is as such: First a linear fit to the spectrum continuum is performed using the `optimize_curve` routine to fit a line using a least squares optimization. The fitting window around each emission line is approximately 400 Å (~ 75 pixels) with nearby emission, sky lines, and internal reflections regions being masked out. After the con-

³Available as part of the IDL Astronomy User's Library

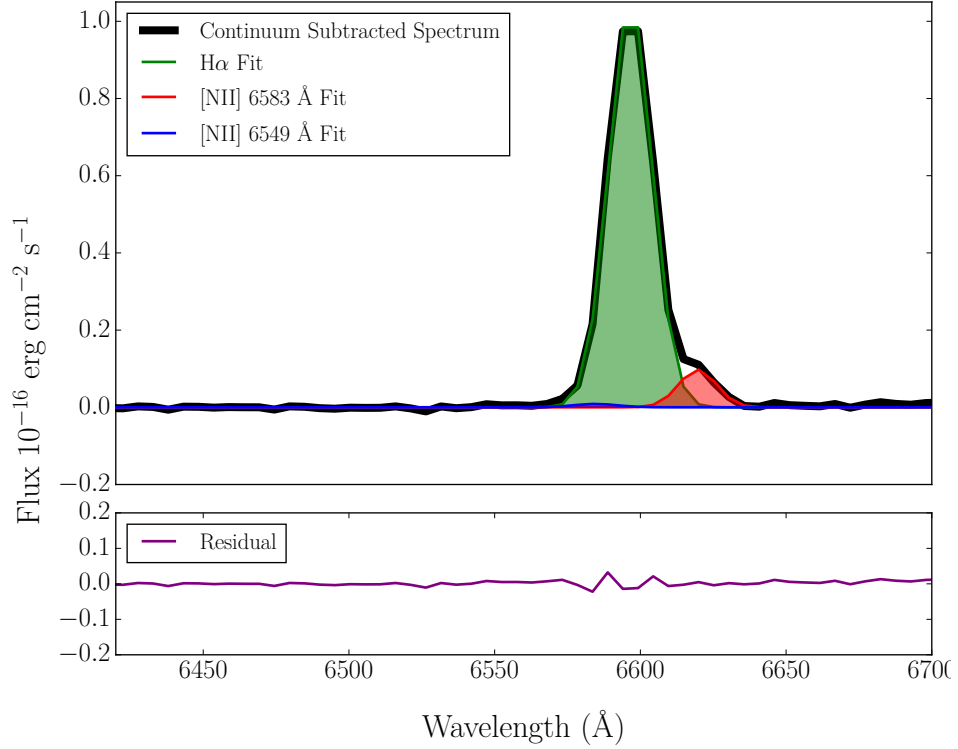


Figure 3.2: Example Spectra Showing Blending of Emission Lines. Demonstrating the blending within the [NII] and H α emission lines due to the instrumental resolution (5.3 Å). Our Python based Gaussian fitting routines are able to deconvolve the three emission lines into their constituent parts, as can be seen by the three Gaussian curves plotted in red, green, and blue. The flux in the blue [NII] 6549 Å emission line is negligible. Details of our ability to recover the three emission line fluxes can be found in Appendix A. Our oxygen abundance estimations rely upon measurements of the H α and [NII] emission lines.

tinuum has been subtracted, the [NII] and H α emission lines are fit using `gaussfitter`² to fit 3 Gaussian curves simultaneously. This allows us to separate the individual components of the 3 blended emission lines.

The output measurements of `gaussfitter` are not heavily dependent upon initial input parameters assumed, therefore we provide it an initial input intensity of 0.5 erg cm⁻²s⁻¹, an initial input peak position of the redshift corrected expected peak for each line, and an initial input dispersion of 7.5 Å, equal to the instrumental dispersion of the observations. No line flux ratios are assumed within our fits. The `gaussfitter` bounds are set up such that each Gaussian fit is limited to a maximum 10% variation from its expected peak position and FWHM. Because the instrumental dispersion dominates the width of the emission lines, we do not expect line widths to vary widely across spaxels.

We do not include a fit to the Balmer absorption in our procedures. Our observations are insufficient to reliably estimate the stellar continuum for accurate absorption measurements. However it is likely that Balmer absorption effects are negligible and well within our uncertainties (Rosa-González et al., 2002). Further details about the emission line flux fitting code and our ability to recover the blended emission lines can be found in Appendix A.

Uncertainties on our flux measurements are estimated using a Monte Carlo Markov chain (MCMC) technique with 1000 iterations. For each iteration, random noise is added to the spectrum on the order of the residuals to the linear fit. Then the emission line fluxes are remeasured. The 1 σ width of the Gaussian distribution of flux values provided by 1000 iterations provides the uncertainties in our line fluxes. These uncertainties are then propagated using standard Taylor series error propagation methods in order to determine the uncertainties in our derived quantities.

We perform the linear and Gaussian fits on the blue and the red end of the

spectrum separately, with the blue end containing the $H\beta$ and [OIII] lines, and the red end containing the $H\alpha$ and [NII] lines. The results of our fitting routine on the red end of an integrated spectrum can be seen in Figure 4.1.

3.3.2 Photometric Observations

To obtain stellar mass estimations for our galaxies, we utilize the stellar mass estimation procedure outlined in West et al. (2010). Doing so requires accurate photometric observations from the Sloan Digital Sky Survey (SDSS; Eisenstein et al. 2011) Data Release 12 (Alam et al., 2015) which is the final data release of SDSS-III. The automated SDSS photometric pipeline (Lupton et al., 2002) is optimized for small, well resolved objects and is known to be unreliable for clumpy and diffuse objects such as dwarf galaxies, mostly due to the SDSS algorithm’s aggressive parent-child splitting routines. As can be seen in Figure 3.1, Petrosian flux measurements could possibly be an inaccurate representation of the flux of our galaxies. West et al. (2010) found that roughly 25% of SDSS galaxies have less than 90% of their flux contained in the brightest child. Therefore, to obtain more accurate stellar mass estimations, we have chosen to run Source Extractor (Bertin and Arnouts, 1996) manually on each of the SDSS bandpass image frames for each of the 11 galaxies within our IFU sample.

To ensure that the SDSS images are aligned properly, we first use HASTROM.PRO to align each individual bandpass fits image to the r-band image coordinates. We stack all 5 photometric bands to create a higher signal/noise detection image. We run Source Extractor in dual image mode with the detection image and each of the individual frames. The default values and keyword searches are used as inputs to Source Extractor except the following: MAG_ZEROPOINT = 22.5, BACK_SIZE

²written by Adam Ginsburg <http://www.adamginsburg.com/pygaussfit.htm>

= 256, and PIXEL_SCALE = 0.396. Additionally for every galaxy we begin with the following parameters: DEBLEND_NTHRESH, DETECT_THRESH, ANALYSIS_THRESH set to 1.0, and then adjust them accordingly to ensure that each dwarf galaxy is detected as a single source in the segmentation map, and that the full flux is being captured when viewing the residuals map. This segmentation map is also used to select the spaxels to be summed for SFR estimation.

3.3.3 *Stellar Masses*

Stellar masses are estimated according to the color-derived M/L ratio of West et al. (2010). The West et al. (2010) stellar mass estimation is a modification of the work done by Bell et al. (2003). The Bell et al. (2003) mass estimation assumes a “Diet Salpeter” IMF, however the West et al. (2010) estimation modifies the Bell et al. (2003) estimation to a Kroupa IMF. This stellar mass estimation technique has been shown to be accurate within 20% of the actual stellar mass (Bell et al., 2003). Photometric data for the IFU observed dwarf galaxies are derived from the Source Extractor measurements of the SDSS g , r , and i filters as detailed in Section 3.3.2. With proper SDSS photometric measurements obtained, we utilize the West et al. (2010) stellar mass to light estimation:

$$\log(M_*/L_i) = -0.222 + 0.864(g - r) + \log(0.71) \quad (3.1)$$

Assuming a solar i -band absolute magnitude of 4.57 (Sparke and Gallagher, 2000), we then convert the i -band photometry into stellar mass estimations using the conversion outlined in West et al. (2010) along with the M/L ratio defined in Equation 3.1.

$$M_* = (M_*/L_i) \times 10^{-((M_i - 4.57)/2.51)} \quad (3.2)$$

Because these stellar mass estimations rely upon *i*-band absolute magnitudes, we require accurate distance estimations. For the local universe dwarf IFU observed galaxies, we cannot rely upon the redshift to provide accurate distances due to gravitational interactions within the local universe. Therefore, we utilize the distance estimations from the ALFALFA catalog for all galaxies below a redshift of 6,000 km s⁻¹ ($z < 0.02$) where the errors on the distance estimates become comparable to those of Hubble flow estimations (Haynes et al., 2011). The ALFALFA catalog distances are calculated using the local universe peculiar velocity model of Masters et al. (2004) derived from the SFI++ catalog of galaxies (Springob et al., 2007) and published literature values are adopted as appropriate. See Haynes et al. (2011) for a full explanation of the model used. Above a redshift of 6,000 km s⁻¹ we calculate the luminosity distance (D_L) from the SDSS redshift assuming the motions of galaxies are dominated by the Hubble flow.

Using this method, stellar masses for each of the 11 galaxies presented here are calculated to be in the range $6.58 \leq \log(M_*) \leq 8.78$. The full list of stellar masses can be found in Table 3.1. Uncertainties in our stellar masses are derived from propagating the Source Extractor provided photometric uncertainties through the standard Taylor series technique.

Table 3.1: Integrated Properties of Dwarf Galaxies

Galaxy AGC#	RA hh:mm:ss.s	Dec \pm hh:mm:ss	Distance ^a Mpc (\pm 2.43)	HI-gas Mass ^a log(M _⊙)	Stellar Mass log(M _⊙)	Luminosity B Band mag	Metallicity 12+log(O/H)	SFR log(M _⊙ yr ⁻¹)
AGC191702	09:08:36.5	+05:17:32	8.7 \pm 2.43	7.74 \pm 0.18	6.67 \pm 0.61	-12.09 \pm 0.63	7.94 \pm 0.13	-2.76 \pm 0.34
AGC202218	10:28:55.8	+09:51:47	19.6 \pm 2.43	7.75 \pm 0.50	8.12 \pm 0.38	-14.95 \pm 0.28	8.22 \pm 0.11	-1.72 \pm 0.29
AGC212838	11:34:53.4	+11:01:10	10.3 \pm 2.43	7.60 \pm 0.19	6.94 \pm 0.56	-12.68 \pm 0.53	8.05 \pm 0.14	-2.73 \pm 0.32
AGC220755	12:32:47.0	+07:47:58	16.4 \pm 2.43	7.18 \pm 1.20	7.76 \pm 0.43	-13.94 \pm 0.33	8.49 \pm 0.16	-2.51 \pm 0.64
AGC220837	12:36:34.9	+08:03:17	16.4 \pm 2.43	7.41 \pm 0.54	8.78 \pm 0.46	-16.11 \pm 0.33	8.56 \pm 0.13	-2.20 \pm 1.28
AGC220860	12:38:15.5	+06:59:40	16.4 \pm 2.43	7.22 \pm 1.39	7.57 \pm 0.42	-13.92 \pm 0.33	7.82 \pm 0.13	-2.14 \pm 0.14
AGC221000	12:46:04.4	+08:28:34	16.5 \pm 2.43	7.46 \pm 0.83	8.35 \pm 0.44	-15.44 \pm 0.33	8.35 \pm 0.05	-1.65 \pm 0.08
AGC221004	12:46:15.3	+10:12:20	16.7 \pm 2.43	7.66 \pm 0.55	7.98 \pm 0.30	-14.61 \pm 0.22	8.35 \pm 0.16	-2.23 \pm 0.22
AGC225852	12:59:41.9	+10:43:40	16.6 \pm 2.43	7.68 \pm 0.53	7.57 \pm 0.42	-13.89 \pm 0.33	8.27 \pm 0.22	-2.53 \pm 0.38
AGC225882	12:03:26.3	+13:27:34	23.6 \pm 2.43	8.15 \pm 0.30	7.06 \pm 0.35	-13.66 \pm 0.25	7.95 \pm 0.18	-2.33 \pm 0.05
AGC227897	12:50:04.2	+06:50:51	16.6 \pm 2.43	7.44 \pm 0.89	6.58 \pm 0.45	-12.08 \pm 0.35	7.67 \pm 0.42	-2.88 \pm 0.24

^a Values obtained from the ALFALFA α .40 catalog (Haynes et al., 2011). Uncertainties in the distance are dominated by the local velocity dispersion measured by (Masters et al., 2005).

3.3.4 ALFALFA/SDSS Sample Selection

To compliment the IFU observed dwarf galaxy results, we compare this sample to galaxies selected from the ALFALFA HI survey. The ALFALFA team has cross-matched their HI detections to the SDSS database in order to associate the radio HI detection to optical photometric galaxy detections. We cross reference the ALFALFA $\alpha.40$ database (15,855 objects) with the SDSS DR12 spectroscopic database and find 7,773 ALFALFA galaxies with SDSS spectroscopic observations. We first remove the 6 galaxies from the IFU observed dwarf galaxy sample that overlap with the ALFALFA/SDSS sample in order to ensure that they are not counted twice within our combined sample. We remove AGN contamination from our sample with the Kauffmann et al. (2003) selection criteria, leaving us with 6,151 galaxies. We remove galaxies for which the aperture correction is exceedingly large by cutting those galaxies for which the difference between the Petrosian r -band magnitude and the fiber r -band magnitude exceeds 5 mag, bringing our sample down to 6,137 galaxies. We also select for galaxies with a redshift $z < 0.05$, bringing our sample to 5,759 galaxies. We then perform a cut to ensure that the SDSS spectra contain $H\alpha$ emission at a S/N greater than 3 leaving 5,751 galaxies. After performing a final cut to exclude galaxies for which the Petrosian stellar mass estimations disagree with the MPA-JHU catalog stellar mass estimations by more than 0.5 dex, we have 5,436 galaxies in our final crossmatched ALFALFA/SDSS sample. In comparison, Bothwell et al. (2013) perform similar cuts, although they specify $H\alpha$ S/N > 25 and remove galaxies for which their two oxygen abundance estimations disagree, leaving them with a sample containing 4,253 galaxies.

3.3.5 Comparison Data

To provide additional galaxies in the low stellar-mass/low luminosity regime that is poorly constrained by the ALFALFA/SDSS sample, we also include in our MZR/LZR analysis data from similar surveys found in the literature of low stellar-mass/low luminosity galaxies. We will utilize data from the following surveys:

- Saintonge (2007) - Observations of 25 low HI-mass ALFALFA dwarf galaxies observed using long-slit spectroscopy from the Double Spectrograph (DBSP; Oke & Gunn 1982) at Mount Palomar’s Hale 5m telescope. Stellar masses are derived from B and V band photometry using the simple stellar population models from Bell et al. (2003). These are galaxies very similar in nature to those of the IFU observed dwarf galaxy sample, except that narrow-band H α imaging had revealed the presence of at least one bright HII region per galaxy making long-slit spectroscopy possible.
- Berg et al. (2012) - A sample of low-luminosity galaxies selected from the Spitzer Local Volume Legacy survey and observed using MMT long-slit spectroscopy. Stellar masses are derived from B and K band photometry using models from Bell and de Jong (2001).
- James et al. (2015) - A morphologically selected survey of 12 SDSS dwarf irregular galaxies, observed using MMT long-slit spectroscopy. Stellar masses are derived from Bell et al. (2003) g and r band photometry.
- Survey of HI in Extremely Low-mass Dwarfs (SHIELD; Haurberg et al., 2015) - An ALFALFA derived survey of 8 galaxies observed using long-slit spectroscopy from the Mayall 4m telescope at KPNO. Stellar mass estimations come from

IR (3.6 and 4.5 μm) photometric colors using the method from Eskew et al. (2012). B-band magnitudes come from WIYN 3.5m observations.

Due to offsets between oxygen abundance calibrations (Kewley and Ellison, 2008), it is necessary to perform oxygen abundance estimations consistently in order to obtain meaningful comparisons between samples. Therefore, for each of the comparison samples from other studies, we have recalculated oxygen abundance estimations (as described in Section 3.4.1) using the emission line fluxes reported within each survey.

Similarly stellar mass estimations from all of the above surveys have been rescaled onto a Kroupa initial mass function (IMF) to match the stellar mass estimations that we perform on both the dwarf IFU observed sample and the larger crossmatched ALFALFA/SDSS sample in Section 3.3.3.

3.4 Analysis

3.4.1 Oxygen Abundance

As a proxy for the gas-phase metallicity of a galaxy, we estimate the oxygen abundance using strong emission line based measurements. Due to the low surface brightness of the IFU observed dwarf galaxy sample, we are unable to detect any of the faint auroral lines required for direct (T_e based) oxygen abundance measurements. We are also limited by our wavelength range to using the [OIII], [NII], and Balmer hydrogen emission lines to perform our oxygen abundance estimations. We attempted to edit the VIMOS pipeline source code to extend the wavelength range which would allow us to capture the [OII] feature required for R23 ($R23 = ([\text{OII}]\lambda 3727 + [\text{OIII}]\lambda 4958, 5007) / \text{H}\beta$) based estimations, however issues with interference between overlapping pseudo-slits on the CCD proved to be a hinderance to accurate [OII] emission line measurements.

Ideally we would use the full range of emission lines within our spectrum. The

O3N2 based oxygen abundance estimation technique of Pettini and Pagel (2004) (hereafter PP04) is calculated using the flux of the emission lines in [OIII] λ 5007, H β λ 4861, H α λ 6563, and [NII] λ 6583. Unfortunately, the calibration of the PP04 O3N2 based estimations becomes unreliable near or below $12+\log(\text{O}/\text{H}) = 8.09$ (Pettini and Pagel, 2004). For completeness, we include in Appendix B a parallel analysis utilizing the O3N2 oxygen abundances and find that our conclusions would not change.

N2 based estimations rely only on the H α λ 6563 and [NII] λ 6583 features and are defined as

$$N2 = \log \left\{ \frac{[\text{NII}]\lambda 6583}{\text{H}\alpha} \right\}. \quad (3.3)$$

N2 based oxygen abundance estimations have the benefit of being less sensitive to the ionization parameter (although not completely independent; see Morales-Luis et al. 2014). The PP04 N2 estimation was calibrated down to metallicities as low as $12+\log(\text{O}/\text{H}) = 7.48$ (Pettini and Pagel, 2004).

Throughout this paper we will utilize the N2 oxygen abundance estimation as calibrated by Denicoló et al. 2002; hereafter D02 which was targeted towards low gas-phase metallicity galaxies, calibrated over a range $7.2 \leq 12+\log(\text{O}/\text{H}) \leq 9.1$, and is well behaved at the low metallicity regime. In the D02 system the oxygen abundance is defined as:

$$12 + \log(\text{O}/\text{H}) = 9.12 + 0.73 \times N2. \quad (3.4)$$

The blending of the emission lines due to instrumental resolution in the dwarf IFU observed galaxy sample causes N2 based oxygen abundance estimations to become less accurate in low flux spaxels. However, when we use the integrated AoN selected spaxels for the entire galaxy, the integrated flux is of sufficient quality to reliably

deblend the three Gaussian components that compromise [NII] and H α as demonstrated in Figure 4.1. For our dwarf galaxy IFU observed sample, we calculate oxygen abundance estimations in the range $7.67 < 12+\log(\text{OH}) < 8.56$, indicating that our low stellar mass sample does indeed exhibit low gas-phase metallicity. Uncertainties in our oxygen abundance estimations are derived from Taylor series propagation of the uncertainties in the emission line fluxes measured in the IFU observed dwarf galaxy sample. The full list of oxygen abundances calculated for each IFU observed dwarf galaxy can be found in Table 3.1.

3.4.2 Luminosity

The B-band Luminosity-Metallicity Relation (LZR) has been claimed to be as strong of a gas-phase metallicity indicator as the MZR when reliable distance measurements and appropriate photometry are used (Berg et al., 2012). Throughout this work, we will perform a parallel analysis to the FMR using luminosity in place of stellar mass. We calculate the B-band absolute magnitudes (M_B) from SDSS photometry using the relation from Lupton (2005).

$$m_B = g + 0.3130 * (g - r) + 0.2271. \quad (3.5)$$

We calculate B-band luminosities for the IFU observed dwarf galaxy population in the range $-16.11 < M_B < -12.08$. As detailed in Section 3.3.3, this requires accurate luminosity distances, therefore we follow the same procedure and utilize ALFALFA catalog distances for $cz < 6,000$ and assume a Hubble flow for $cz > 6,000$. Uncertainties in our B-band luminosities are derived from propagating the Source Extractor provided photometric uncertainties through the standard Taylor series technique. The full list of luminosities and their uncertainties can be found in Table 3.1.

3.4.3 Star Formation Rates

Star Formation Rates (SFRs) for each galaxy are derived from the integrated flux of $H\alpha$ emission within the segmentation map selected spaxels of each galaxy. Spatial maps of the stellar continuum and $H\alpha$ emission for each galaxy can be seen in Figure 4.2. The SFR for each galaxy is determined by first integrating the flux of every spaxel selected by the segmentation map selection criteria (the gray shaded regions in Figure 4.2). We use the integrated flux because, at the average distance of our galaxies, each spaxel subtends 25 pc on a side and $H\alpha$ based SFR estimations have been shown to be unreliable on scales less than 100-1000 pc (Kennicutt and Evans, 2012), or when the luminosity drops below 10^{38} - 10^{39} erg s $^{-1}$ (which corresponds to an SFR of ~ 0.001 - 0.01 M $_{\odot}$ yr $^{-1}$). This would mean that several galaxies (AGC220837, AGC221004, AGC225852, and AGC228882) have unreliable SFR estimates on a spaxel by spaxel basis as can be seen in Figure 4.2.

To convert the $H\alpha$ emission line measurements into SFR estimations, we convert our $H\alpha$ emission line flux ($H\alpha$) into luminosity ($H\alpha_L$) using the luminosity distance (D_L) as

$$(H\alpha_L)_{\text{obs}} = 4\pi H\alpha D_L^2. \quad (3.6)$$

where the subscript “obs” denotes the observed $H\alpha$ luminosity.

We need to correct for reddening to obtain the intrinsic $H\alpha$ luminosity $(H\alpha_L)_{\text{int}}$ where

$$(H\alpha_L)_{\text{int}} = (H\alpha_L)_{\text{obs}} 10^{0.4A_{H\alpha}}. \quad (3.7)$$

The attenuation at a specific wavelength (A_{λ}) is defined as

$$A_{\lambda} = \kappa(\lambda)E(B - V) \quad (3.8)$$

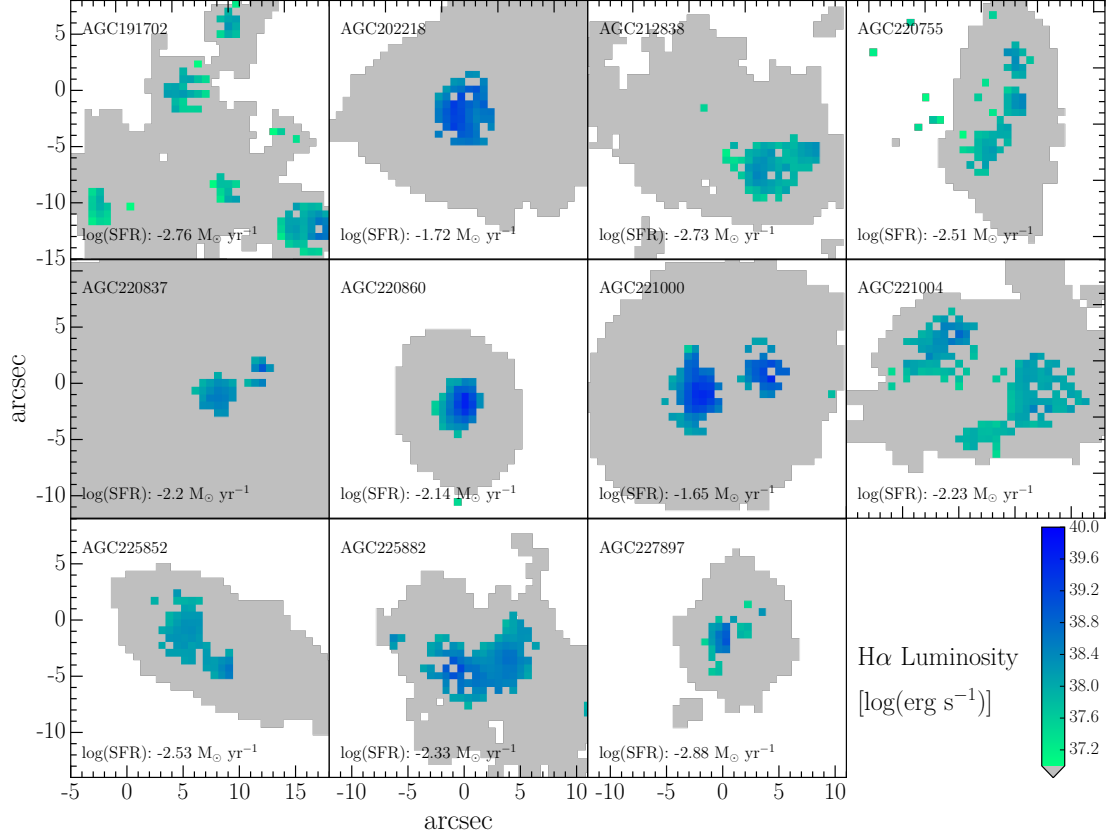


Figure 3.3: Spatial Map of H α Emission and Segmentation Map. Spatial mapping of the H α emission line flux within a subset of the IFU field-of-view (Figure 3.1). The gray regions indicate the stellar continuum as selected by the segmentation maps. The blue-green pixels indicate the spaxels which pass the AoN of 5 cut. The intensity of the flux varies widely between galaxies, and even within galaxies the flux intensity appears to be quite patchy. Also shown for each galaxy is the SFR for each galaxy calculated using the flux integrated over the entire gray region showing that our galaxies cover a range of approximately 1.5 dex in SFR.

where $E(B-V)$ is the broadband color excess and $\kappa(\lambda)$ is the value of an attenuation curve at wavelength λ . In order to obtain the reddening for each galaxy based on the intrinsic value of the Balmer decrement, we will utilize the color excess between the $H\alpha$ and $H\beta$ emission lines. This can be found by substituting the wavelengths of $H\alpha$ and $H\beta$ into Equation 3.8 to find

$$A(H\beta) - A(H\alpha) = \kappa(H\beta)E(B-V) - \kappa(H\alpha)E(B-V). \quad (3.9)$$

Equation 3.9 could alternatively be defined as $E(H\beta - H\alpha)$, which is analogous to $E(B-V)$ such that

$$A(H\beta) - A(H\alpha) = E(H\beta - H\alpha) = 2.5 \times \log_{10} \left\{ \frac{H\alpha/H\beta}{2.86} \right\} \quad (3.10)$$

in which we have used the fact that the intrinsic $H\alpha$ to $H\beta$ ratio is 2.86 for Case B recombination with a temperature $T = 10^4\text{K}$ and an electron density $n_e = 10^2 \text{ cm}^{-3}$ (Osterbrock, 1989)

By setting the right hand sides of Equations 3.9 & 3.10 equal to each other and rearranging, we find that

$$E(B-V) = \frac{2.5}{\kappa(H\beta) - \kappa(H\alpha)} \log_{10} \left\{ \frac{H\alpha/H\beta}{2.86} \right\}. \quad (3.11)$$

Which can then be used in Equation 3.8 to find the color excess at the wavelength for $H\alpha$. We use the reddening curve from Calzetti et al. (2000) to obtain $\kappa(H\alpha) =$

3.33 and $\kappa(\text{H}\beta) = 4.60$ for the attenuation correction:

$$\begin{aligned} A(\text{H}\alpha) &= \frac{2.5 \times \kappa(\text{H}\alpha)}{\kappa(\text{H}\beta) - \kappa(\text{H}\alpha)} \log_{10} \left\{ \frac{\text{H}\alpha/\text{H}\beta}{2.86} \right\} \\ &= 6.56 \times \log_{10} \left\{ \frac{\text{H}\alpha/\text{H}\beta}{2.86} \right\}. \end{aligned} \quad (3.12)$$

Once we have our dust corrected $\text{H}\alpha$ luminosity values, we apply the Hao et al. (2011) conversion

$$\text{SFR} = \log((\text{H}\alpha_L)_{\text{int}}) - 41.27 \quad (3.13)$$

We calculate star formation rates for the IFU observed dwarf galaxy population in the range $-2.88 < \log(\text{M}_{\odot} \text{ yr}^{-1}) < -1.65$. The full list of star formation rates can be found in Table 3.1. Uncertainties in our star formation rates are propagated using standard Taylor series error propagation techniques from the $\text{H}\alpha$ flux measurement uncertainties obtained via 1000 MCMC iterations.

3.4.4 ALFALFA/SDSS Analysis

In order to compare results derived for the IFU observed dwarf galaxy sample with the larger ALFALFA/SDSS sample, we must ensure that the ALFALFA/SDSS data is reduced in a manner as similar as possible to the IFU observed dwarf galaxy data. HI-gas masses between samples are obtained from the same ALFALFA database, therefore we are confident that all HI-gas masses are derived similarly between the two samples. For the stellar-mass, luminosity, gas-phase metallicity, and SFR calculations, we detail the similarities and differences between analysis of the two datasets in the following subsections. Figure 3.4 displays a comparison of the observables for 6 galaxies that overlap between the IFU observed dwarf galaxy sample and the larger ALFALFA/SDSS sample. In general we find that they agree within 1 standard deviation, and outlying data points can be explained. This leads us to conclude that

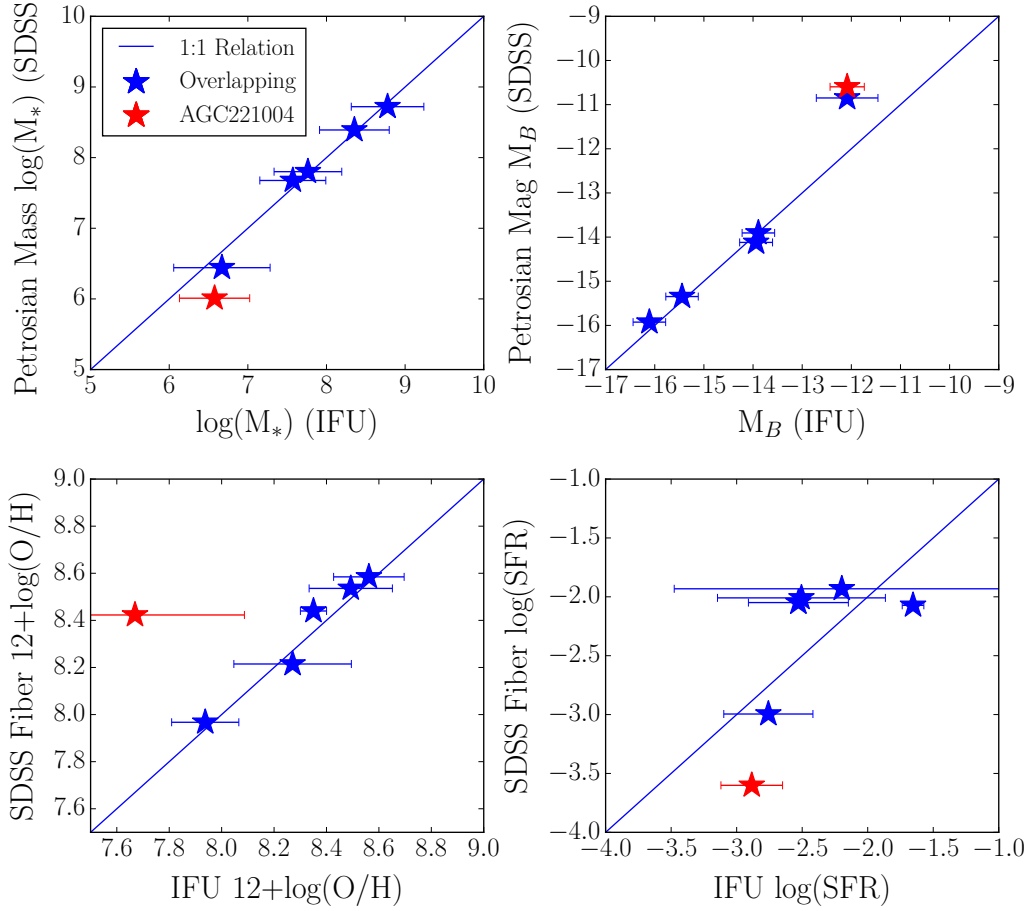


Figure 3.4: Comparison Between IFU and SDSS Measurements. Comparison between the measured values in galaxies that overlap between the IFU observed dwarf galaxy sample and the larger ALFALFA/SDSS sample, showing the consistency between the data used to calculate observables for each of the two data sets. Discrepancies in the stellar-mass and luminosity values can be explained by the issues with SDSS Petrosian magnitude measurements. The poor correlation between SFR estimations can be explained by the patchy dwarf galaxy star formation being observed with a single SDSS fiber. Galaxies in blue have passed the selection criteria show reasonable agreement between both samples, galaxies in red would be rejected from the ALFALFA/SDSS sample using the selection criteria outlined in Section 3.3.4.

comparisons between the samples are valid, however the outliers noted highlight the need for IFU observations and careful analysis in the low stellar-mass/luminosity regime. The sample selection criteria outlined in Section 3.3.4 is used to remove these outlier galaxies from our ALFALFA/SDSS sample.

3.4.4.1 *Stellar Mass*

Following the procedure in Section 3.3.3, we perform the same calculations as in Equations 3.1 & 3.2 to obtain stellar-mass estimations. However, we use Petrosian magnitudes from the SDSS public database in place of Source Extractor derived photometry. Although it would be ideal to perform the same Source Extractor procedure, doing so would be prohibitively time consuming for the entire ALFALFA/SDSS sample. For the crossmatched ALFALFA/SDSS sample we utilize ALFALFA catalog model distances for galaxies where $cz < 6,000 \text{ km s}^{-1}$ and cosmological distances otherwise. In Figure 3.4 we find that 5 of the 6 galaxies that exist in both samples are within 1 standard deviation of the 1:1 correlation, with one significant outlier (AGC221004).

To relieve this tension, we examine the MPA-JHU value added catalog (Kauffmann et al., 2003; Brinchmann et al., 2004; Tremonti et al., 2004) which has stellar mass estimations based on spectral energy distributions (SED) fits to the SDSS fiber spectroscopy. These stellar-mass estimations utilize Bruzual and Charlot (2003) stellar templates and assume a Kroupa IMF (Kauffmann et al., 2003). We find that for galaxies which overlap between the IFU observed dwarf galaxy sample and the ALFALFA/SDSS sample, the Source Extractor based stellar-mass estimations agree within 7% with the MPA-JHU SDSS spectroscopic fiber derived total stellar mass estimates, suggesting that the SDSS Petrosian photometry is inaccurate for AGC221004.

As outlined in West et al. (2010), roughly 25% of Petrosian fluxes for the SDSS population are inaccurate due to issues with parent-child splitting in the SDSS algorithms, this is consistent with what we have observed in Figure 3.4. The MPA-JHU catalog also contains a significant number of outliers, so would not be a complete replacement for the SDSS petrosian magnitudes, instead we have implemented a quality control cut on the ALFALFA/SDSS data in which we exclude galaxies from our sample for which the stellar mass estimates disagree by more than 0.5 dex between the Petrosian and MPA-JHU stellar mass estimations. With this quality control check in place, we continue to use the West et al. (2010) based mass estimations for the IFU observed dwarf galaxies and the ALFALFA/SDSS population in order to keep the analysis as consistent as possible between the two samples.

3.4.4.2 Luminosity

Following the procedure in Section 3.4.2, we once again utilize the Petrosian magnitudes provided by the SDSS catalog in order to derive B-band luminosities using Equation 3.5. When we compare the results of the Petrosian magnitude derived luminosities to the Source Extractor derived luminosities in Figure 3.4, once again we find that AGC221004 exists considerably offset from the expected 1:1 correlation. As observed in Section 3.4.4.1, this is likely due to the known issues with the SDSS pipeline aggressively splitting up the photometry of irregular HII regions. This demonstrates the need for careful analysis of dwarf galaxies in the low-luminosity regime. Errant galaxies such as AGC221004 are removed from the ALFALFA/SDSS sampled by the quality control cuts outlined in Section 3.3.4.

3.4.4.3 Gas-phase Metallicity

To derive the gas-phase metallicity estimations for the larger ALFALFA/SDSS sample, we rely upon emission line fluxes from SDSS single fiber spectroscopy. We

apply the same D02 oxygen abundance estimation (Equation 3.4) as was performed for the IFU observed dwarf sample. In Figure 3.4 we find good agreement between both samples. This is somewhat expected considering that the SDSS fibers target the brightest part of a galaxy, and the integrated IFU fluxes are dominated by the same bright areas. It is worth noting that this lends credence to our emission line de-blending because the SDSS spectroscopy is higher spectral resolution and not significantly blended.

3.4.4.4 *Star Formation Rate*

To determine SFRs for the larger ALFALFA/SDSS sample, we use the $H\alpha$ flux reported in the SDSS 3'' single fiber spectroscopy database. We correct for dust using the same procedure as with the IFU observed dwarf galaxy sample. In addition, we perform an aperture correction to our SFR calculations. As can be seen in Figure 3.1, the SDSS fiber often misses a significant amount of flux in the emission regions of nearby galaxies. Therefore, to more accurately compare our IFU observations which cover the entire star forming region to the SDSS observations, we apply the aperture correction technique outlined in Hopkins et al. (2003)

$$A = 10^{-0.4(r_{\text{petro}} - r_{\text{fiber}})} \quad (3.14)$$

where r_{petro} denotes the SDSS r -band Petrosian flux, and r_{fiber} denotes the SDSS r -band flux within the fiber.

As observed in Figure 3.4, the calculated star formation rates may vary by as much as 0.5 dex in SFR between the two samples, emphasizing the need for IFU observations to collect all of the $H\alpha$ flux. This is to be expected considering the patchy star forming nature of the IFU observed dwarf galaxy sample. The patchy nature of star formations also means that this aperture correction is imperfect, as

seen in Figure 3.4. These facts indicate that ALFALFA/SDSS SFRs are likely to be unreliable for galaxies requiring a large aperture correction. This necessitates the sample selection cut where we exclude galaxies for which the difference between the Petrosian r -band magnitude and the fiber r -band magnitude differ by more than 5 mag as described in Section 3.3.4.

3.5 Results

3.5.1 Mass-Metallicity Relation and Luminosity-Metallicity Relation

The mass-metallicity relation (MZR) can be seen in Figure 3.5 along with homogenized observations from earlier dwarf/low luminosity galaxy surveys. Similar to the process outlined in Mannucci et al. (2010), we bin the ALFALFA/SDSS cross-matched sample by stellar mass, into bins 0.25 dex wide. We then fit a 4 degree polynomial to the mean values of the bins and find the following relationship:

$$12 + \log(O/H) = 8.756 + 0.219 \times m - 0.119 \times m^2 - 0.052 \times m^3 - 0.003 \times m^4 \quad (3.15)$$

where $m = \log(M_*) - 10$. The MZR is fit to data from the literature collected samples, the ALFALFA/SDSS crossmatched sample, and the IFU observed dwarf galaxy sample. In order to ensure robust results, we require that there are at least 21 galaxies per stellar mass bin. We use the limit of 21 galaxies per bin in order to be consistent with the analysis performed in Bothwell et al. (2013). In total there are 15 stellar-mass bins covering the stellar-mass range $7.25 < \log(M_*) < 11.0$. The residual 1σ scatter of every galaxy to the MZR fit in Equation 3.15 is 0.11 dex, similar to the 0.1 dex scatter reported for the MZR of Tremonti et al. (2004). The 1σ scatter of the mean values in each stellar-mass bin is 0.05 dex. The 1σ scatter of the means is the metric that we will use to compare scatter between various metallicity relations.

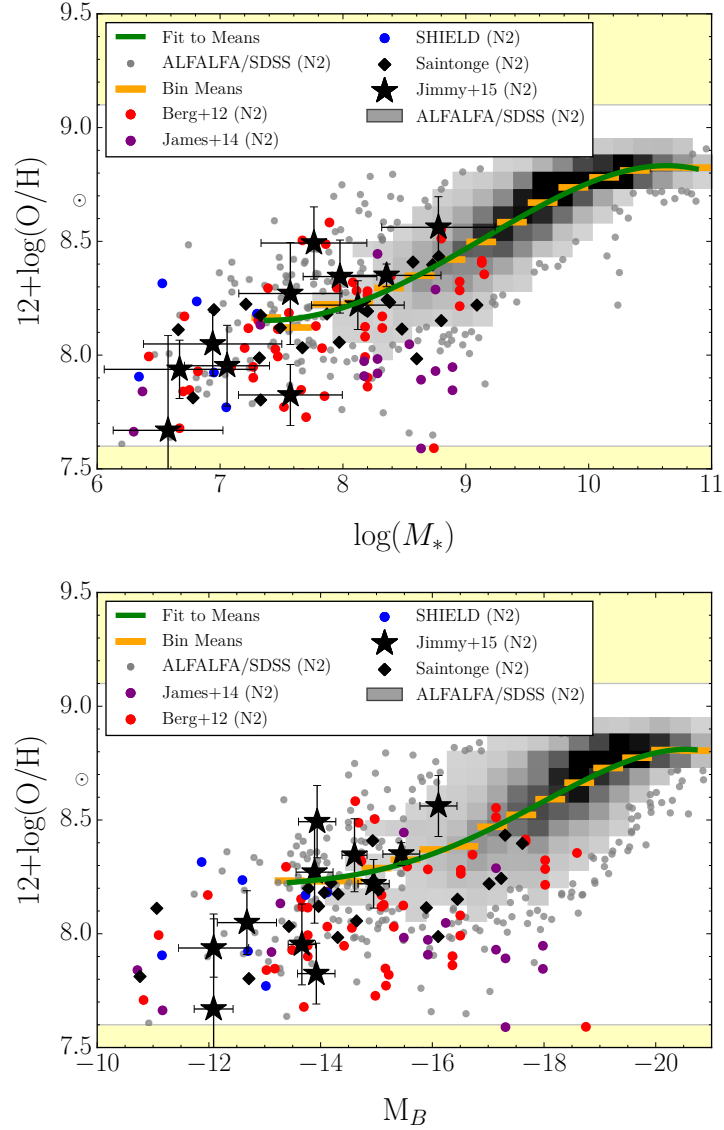


Figure 3.5: Mass-Metallicity and Luminosity-Metallicity Relations. The mass-metallicity relation (top) and the luminosity-metallicity relation (bottom) for the IFU observed dwarf galaxy sample, along with several low stellar mass galaxy observations and the ALFALFA/SDSS sample. The scatter in both the MZR (LZR) fit around the bin means is 0.05 dex (0.03 dex). For reference we plot a sun symbol at solar metallicity, showing that all of the IFU observed dwarf galaxy oxygen abundances are below solar. The yellow regions indicate the calibration limits of the D02 N2 oxygen abundance estimation. We have used the published emission line fluxes from other authors to estimate the oxygen abundance in the same D02 system. The MZR appears to hold down to the lowest stellar masses observed ($\log(M_*) = 7.25$).

The LZR can also be seen in Figure 3.5 along with homogenized observations from similar dwarf/low luminosity galaxy surveys. We bin the combined literature, ALFALFA/SDSS, and IFU observed sample into bins 0.52 dex wide. We then fit a 4 degree polynomial to these mean values and find the following relationship:

$$12 + \log(O/H) = -18.6 - 7.23 \times M_B - 0.724 \times M_B^2 - 0.032 \times M_B^3 - 0.0005 \times M_B^4. \quad (3.16)$$

The LZR is fit to 15 luminosity bins over a range $-13.7 < M_B < -21.0$ in order to ensure that there are at least 21 galaxies per luminosity bin. The residual 1σ scatter of every galaxy to the LZR fit in Equation 3.16 is 0.14 dex. The residual 1σ scatter of the mean values to the LZR in each luminosity bin is 0.03 dex. Again, this is the metric that we will use to compare scatter between various metallicity relations.

3.5.2 MZR/LZR with SFR and HI-gas Mass Dependence

We test whether or not a fundamental metallicity relation explains the enhanced scatter of the MZR and LZR by following a similar procedure as Mannucci et al. (2010) and Bothwell et al. (2013). We bin the crossmatched ALFALFA/SDSS data into SFR bins of $0.85 \log(M_\odot \text{ yr}^{-1})$ and HI-gas mass bins of $0.85 \log(M_\odot)$. We use larger HI-gas mass and SFR bins than Bothwell et al. (2013) to ensure that we have at least 21 objects per bin in our lower stellar mass/luminosity regimes. Figures 3.6 & 3.7 show the result of binning the MZR and the LZR in terms of both SFR and HI-gas mass. A clear separation exists between the HI-gas mass bins shown in the top of Figures 3.6 & 3.7, as well as the SFR bins in the bottom of Figures 3.6 & 3.7. The numerical values of the means used to produce the solid lines in Figures 3.6 & 3.7 can be found in Appendix C. Using these larger HI-gas mass and SFR bins, we are able to extend the ALFALFA/SDSS means relation down to stellar mass bins as

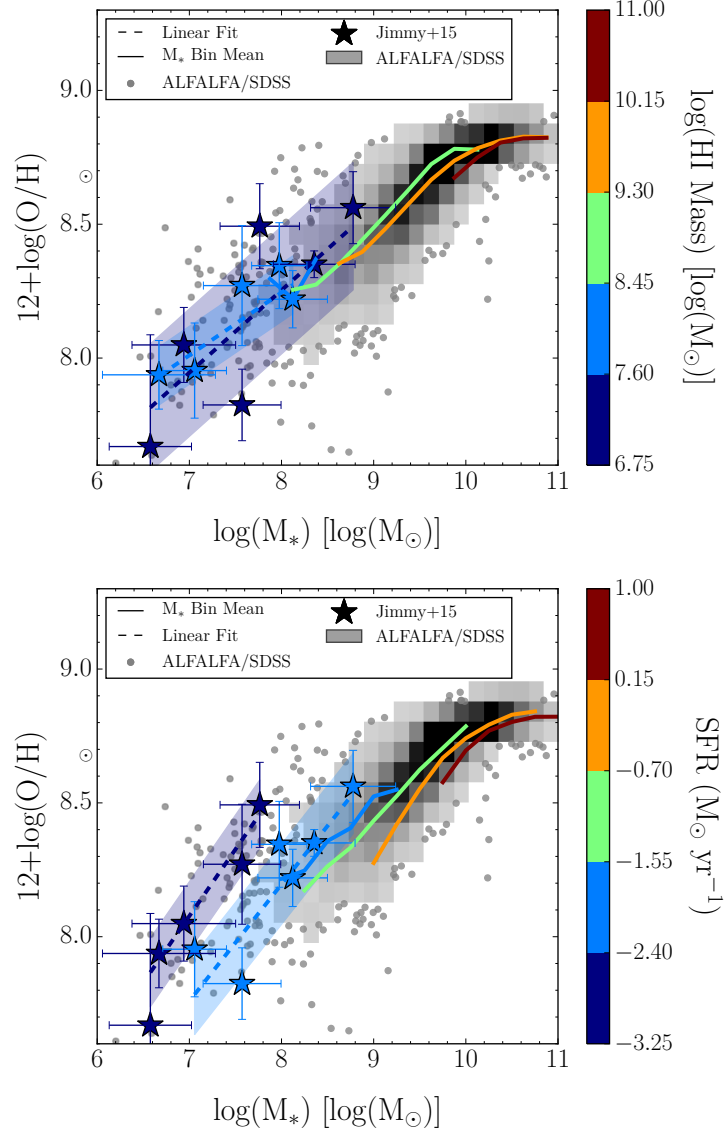


Figure 3.6: Mass-Metallicity Relation Binned by HI-Mass and SFR. The mass-metallicity relation as seen in Figure 3.5 color-coded by HI-gas mass (top) and SFR (bottom). The stars indicate individual observations within our IFU observed sample of dwarf galaxies. The dashed lines indicate linear least squares fits to these points, and the shaded regions indicate the 1σ standard deviations to these fits. The solid curves indicate the mean values of the ALFALFA/SDSS sample, separated into HI-gas mass bins (top) and SFR bins (bottom). Shown in the background are the ALFALFA/SDSS points which are binned to produce the color-coded means. We find little overlap between the HI-gas mass bins (top) and SFR bins (bottom).

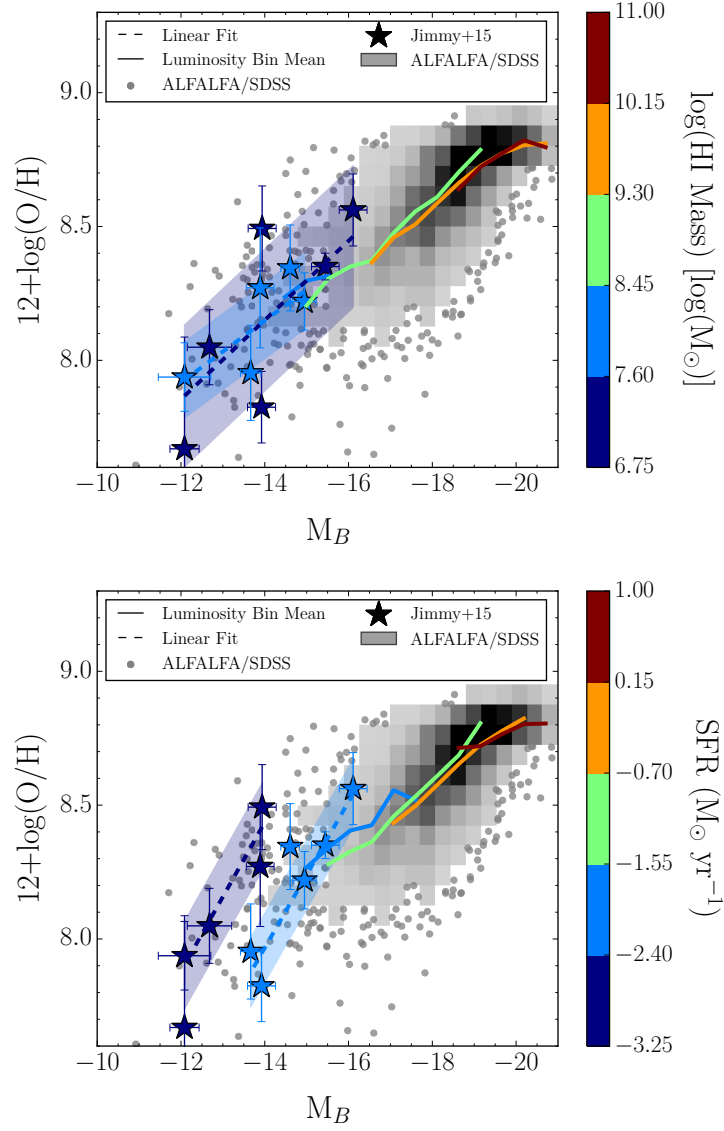


Figure 3.7: Luminosity-Metallicity Relation Binned by HI-Mass and SFR. The luminosity-metallicity relation as seen in Figure 3.5 color-coded by HI-gas mass (top) and SFR (bottom). The stars indicate individual observations within our IFU observed sample of dwarf galaxies. The solid curves indicate the mean values of the ALFALFA/SDSS sample, separated into HI-gas mass bins (top) and SFR bins (bottom). Shown in the background are the ALFALFA/SDSS points which are binned to produce the color-coded means. We find little overlap between the HI-gas mass bins (top) and SFR bins (bottom).

low as $\log(M_*) = 7.75$.

Also shown in Figures 3.6 & 3.7 are the linear least squares fits to the IFU observed dwarf galaxies. The dwarf galaxy sample of this study is not large enough to produce similarly binned mean relationships for dwarf IFU observed data alone, therefore we instead perform least squares optimized linear fits to the dwarf IFU data to demonstrate that it is consistent with the FMR. The numerical values for the linear fits and their 1σ standard deviations can be seen in Table 3.2.

The IFU observed dwarf galaxy sample overlaps with the larger ALFALFA/SDSS sample by ~ 1 dex, providing a valuable consistency check. The added benefit of the IFU observed dwarf galaxy sample is that it is able to test the fundamental metallicity relation down to stellar masses 2 orders of magnitude lower than observed in Mannucci et al. (2010) and Bothwell et al. (2013).

3.5.3 Fundamental Metallicity Relations

In order to test whether the IFU observed dwarf galaxy sample is constant with the offsets in SFR and HI-gas Mass observed for the larger ALFALFA/SDSS cross-matched sample, we examine the fundamental metallicity relationships. We also introduce nomenclature for the luminosity equivalent of the FMR as the fundamental metallicity luminosity (FML) relation, which can be dependent upon SFR (FML_{SFR}) or HI-gas mass (FML_{HI}). The FMR and FML are a projection of three-dimensional parameter space into two dimensions to minimize the scatter observed.

3.5.3.1 MZR SFR Dependence (FMR_{SFR})

Mannucci et al. (2010) define a variable μ_α which combines SFR with stellar mass such that

$$\mu_\alpha = \log(M_*) - \alpha \log(SFR). \quad (3.17)$$

Table 3.2: Linear Fits to Dwarf Galaxy IFU SFR & HI-Mass Bins

SFR Bin	Stellar Mass		1σ Scatter
	Slope	Y-Intercept	
-2.4 to -1.55	0.44 ± 0.01	4.7 ± 0.7	0.15
-3.25 to -2.4	0.5 ± 0.0	4.59 ± 0.22	0.13
HI-gas Mass Bin	Slope	Y-Intercept	1σ Scatter
6.75 to 7.6	0.3 ± 0.01	5.85 ± 0.85	0.22
7.6 to 8.45	0.24 ± 0.0	6.34 ± 0.26	0.1

SFR Bin	Luminosity		1σ Scatter
	Slope	Y-Intercept	
-2.4 to -1.55	-0.27 ± 0.0	4.15 ± 0.64	0.13
-3.25 to -2.4	-0.28 ± 0.0	4.54 ± 0.5	0.16
HI-gas Mass Bin	Slope	Y-Intercept	1σ Scatter
6.75 to 7.6	-0.15 ± 0.0	6.07 ± 0.85	0.24
7.6 to 8.45	-0.13 ± 0.0	6.27 ± 0.32	0.11

Linear fit results for the dotted lines as seen in Figures 3.6 & 3.7. The 1σ scatter is the width of the shaded regions in Figures 3.6 & 3.7.

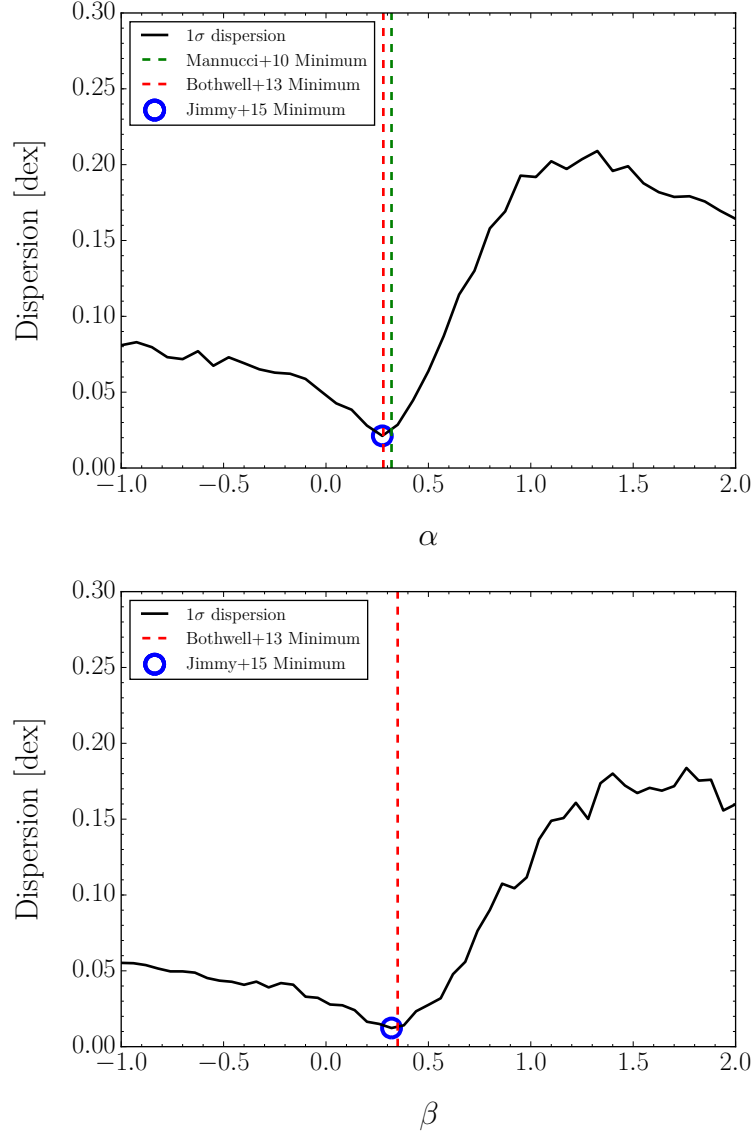


Figure 3.8: Lowest Scatter in FMR_{SFR} and FMR_{HI} Relations. Top: 1σ scatter in the means of the FMR_{SFR} as a function of α . The optimal scatter found by Mannucci et al. (2010) is indicated by the dashed green vertical line, and the optimal alpha value found by Bothwell et al. (2013) is indicated by the dashed red vertical line. We find the lowest scatter in the FMR_{SFR} when $\alpha = 0.28$ Bottom: 1σ scatter in the means of the FMR_{HI} as a function of β . The dashed red vertical line indicates the optimal β value from Bothwell et al. (2013). No β minimum exists from Mannucci et al. (2010) as they did not study the FMR_{HI} . We find the lowest scatter in the FMR_{HI} when $\beta = 0.33$.

They find that $\alpha = 0.32$ minimizes the scatter in the FMR_{SFR} relation, whereas Bothwell et al. (2013) find $\alpha = 0.28$ is the optimal value.

We perform the same tests on our larger crossmatched ALFALFA/SDSS sample in order to find the value of α minimizes the FMR_{SFR} scatter. To find the optimal value of α , we project the ALFALFA/SDSS data onto the μ -metallicity plane and bin our data using the same SFR bins used for Figure 3.6. Each SFR binned dataset is binned a 2nd time in μ space similar to the stellar-mass binning performed in Section 3.5.2 and we once again perform the same cut of 21 galaxies per μ -SFR bin. We take the mean metallicity of each μ -SFR bin and fit a 4th degree polynomial to the binned mean metallicity values. This process is repeated for values of α ranging from -1 to 2.

The dataset used for this procedure includes only the larger ALFALFA/SDSS dataset. We tested using the combined ALFALFA/SDSS and IFU observed dwarf data and found the same scatter per alpha value tested. This is due to the fact that there are only 11 data points in the IFU observed data set being added to the considerably larger ALFALFA/SDSS sample. Also producing the FMR_{SFR} using only the larger ALFALFA/SDSS data means that the test of whether or not the IFU observed dwarf galaxy data fits the same FMR_{SFR} is completely independent.

If $\alpha = 0$ provides the optimal value, that would indicate that the MZR has the lowest scatter obtainable and that taking into account the SFR is unnecessary. Also of note, if $\alpha = 1$ provides the optimal value, that would indicate that the specific star formation rate (M_*/SFR) would be the best projection to use. The scatter obtained for each value of α can be seen in Figure 3.8. We find that a value of $\alpha = 0.28$ provides the lowest scatter for the FMR_{SFR} (Table 3.3). Using this α value we then reproduce the FMR_{SFR} plot using our optimal projections for Figure 3.9.

For the FMR_{SFR} relation seen in Figure 3.9, we find that although the 2nd lowest

(light blue) SFR bin overlaps between the IFU observed dwarf galaxy sample and the larger crossmatched ALFALFA/SDSS sample, the lowest (dark blue) SFR bin is not consistent between the IFU observed dwarf galaxy sample and the crossmatched ALFALFA/SDSS sample. In fact the lowest SFR bin is offset 1σ above the FMR_{SFR} . This is suggestive of a breakdown of the FMR_{SFR} for the lowest SFR galaxies. It is possible that our SFRs are slightly inaccurate in this range considering they are near the limit discussed in Kennicutt and Evans (2012). As star formation rates approach this region, they should be treated as upper limits of the true SFR.

3.5.3.2 MZR HI-Mass Dependence (FMR_{HI})

Bothwell et al. (2013) defines an equation similar to Equation 3.17 for the FMR_{HI} relation:

$$\eta_{\beta} = \log(M_{*}) - \beta(\log(M_{\text{HI}}) - 9.80). \quad (3.18)$$

Wherein they find that a value of $\beta = 0.35$ minimizes the scatter in the gas-phase metallicity- η plane.

To find the optimal value of β , we project the ALFALFA/SDSS data onto the η -metallicity plane and bin our data using the same HI-gas mass bins used for Figure 3.6. Each HI-gas mass binned dataset is binned a 2nd time in η space similar to the stellar-mass binning performed in Section 3.5.2 and we once again perform the same cut of 21 galaxies per η -HI mass bin. We take the mean metallicity of each η -HI mass bin and fit a 4th degree polynomial to the binned mean metallicity values. This process is repeated for values of β ranging from -1 to 2.

If $\beta = 0$ provides the optimal value, that would indicate that taking into account the HI-gas mass is unnecessary. Also of note, if $\beta = 1$ provides the optimal value, then the ratio of HI-gas mass to stellar mass would be the best projection to use. The scatter obtained for each value of β can be seen in Figure 3.8. We find that a

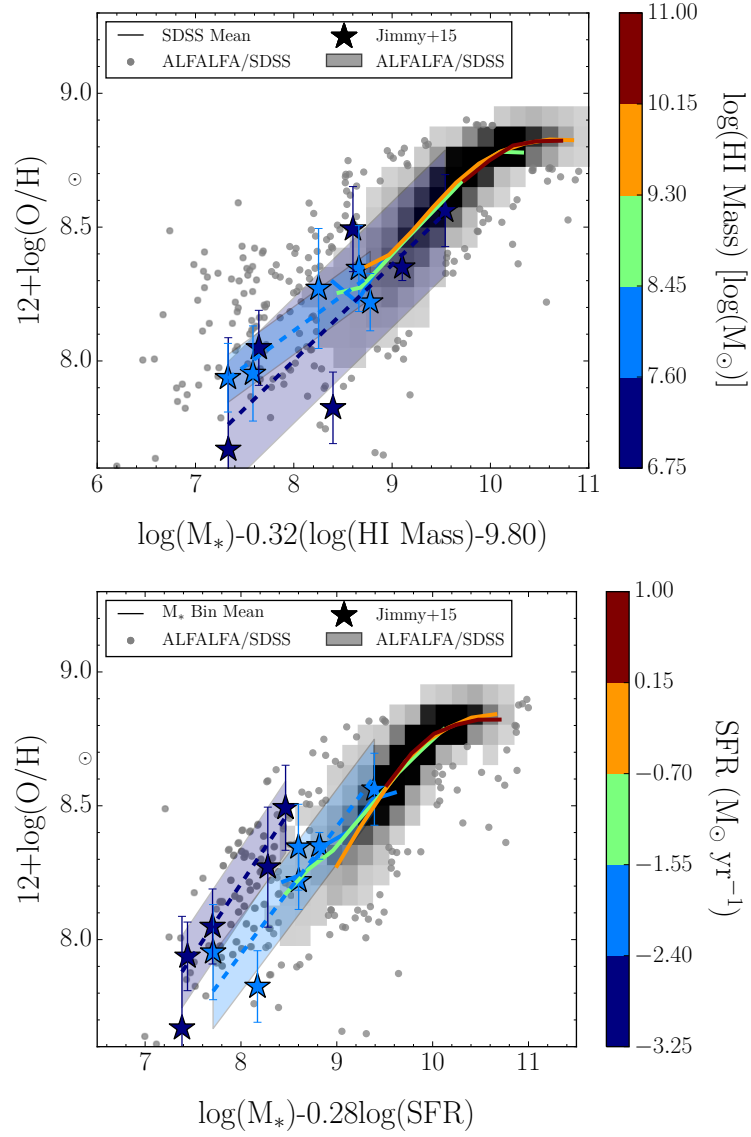


Figure 3.9: FMR_{HI} and FMR_{SFR} Relations. FMR_{HI} (top) and FMR_{SFR} (bottom) as calculated using the α (top) and β (bottom) values found to minimize scatter (Figure 3.8). We find that the FMR_{HI} relation is consistent down to the lowest HI-mass bin, where as the lowest SFR bin in the FMR_{SFR} is offset 1σ above the FMR_{SFR}.

value of $\beta = 0.32$ provides the lowest scatter for the FMR_{HI} (Table 3.3). Using this β value we then produce the FMR_{HI} plot using our optimal projections for Figure 3.9.

For the FMR_{HI} relation, we find that our linear fits to the IFU observed dwarf galaxy sample are, within the 1σ uncertainties, consistent with the binned means of the larger ALFALFA/SDSS crossmatched survey. This suggests that the FMR_{HI} relation is likely to continue down to stellar masses as low as $10^{6.6} M_{\odot}$.

3.5.3.3 LZR SFR Dependence (FML_{SFR})

We define a fundamental luminosity-metallicity relation (FML_{SFR}) using the star formation rate as:

$$\epsilon_{\zeta} = (M_B) - \zeta \log(\text{SFR}) \quad (3.19)$$

To find the optimal value of ζ , we project the ALFALFA/SDSS data onto the ϵ -metallicity plane and bin our data using the same SFR bins used for Figure 3.7. Each SFR binned dataset is binned a 2nd time in ϵ space similar to the luminosity binning performed in Section 3.5.2 and we once again perform the same cut of 21 galaxies per ϵ -SFR bin. We take the mean metallicity of each ϵ -SFR bin and fit a 4th degree polynomial to the binned mean metallicity values. This process is repeated for values of ζ ranging from -2 to 1.

The scatter obtained for each value of ζ can be seen in Figure 3.10. We find that a value of $\zeta = -0.35$ provides the lowest scatter for the FML_{SFR} (Table 3.3). Using this ζ value we then produce the FML_{SFR} plot using our optimal projections for Figure 3.11.

For the FML_{SFR} relation seen in Figure 3.11, we find that although the 2nd lowest (light blue) SFR bin overlaps between the IFU observed dwarf galaxy sample and the larger crossmatched ALFALFA/SDSS sample, the lowest (dark blue) SFR bin is

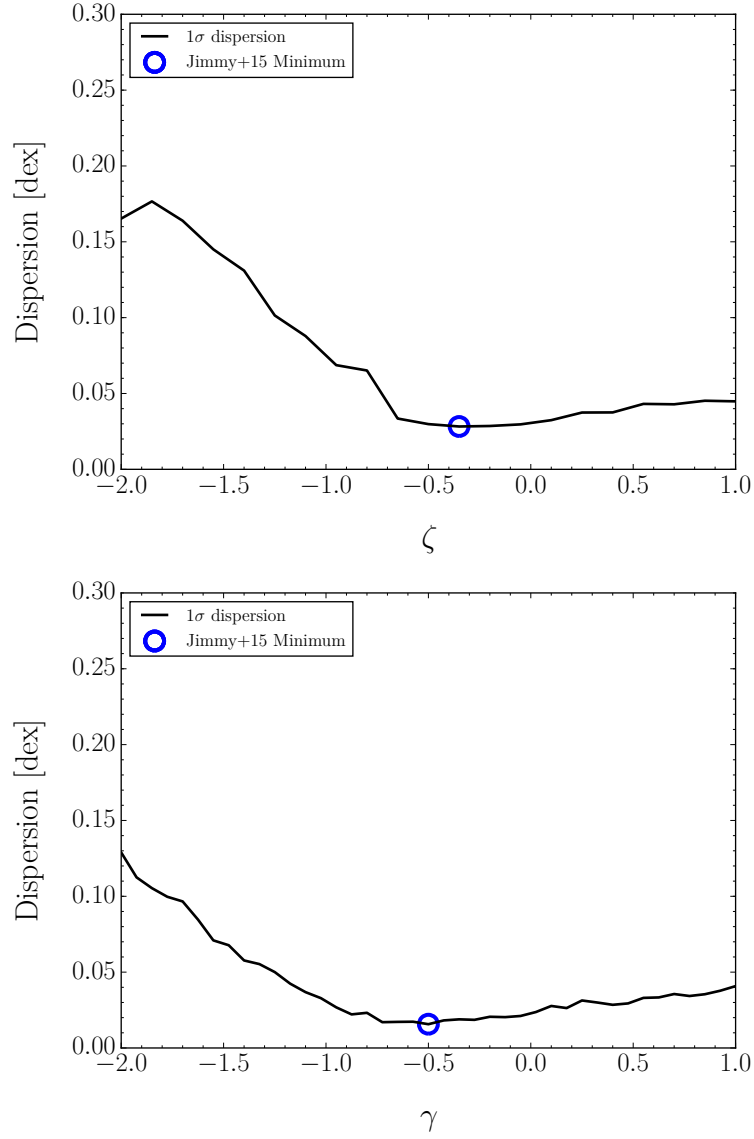


Figure 3.10: Lowest Scatter in FML_{SFR} and FML_{HI} Relations. Top: 1σ scatter in the FML_{SFR} relation as a function of ζ . We find the lowest scatter in the FML_{SFR} relation when $\zeta = -0.35$ Bottom: 1σ scatter in the means of the FML_{HI} as a function of γ . We find the lowest scatter in the FML_{HI} relation when $\gamma = -0.50$.

not consistent between the IFU observed dwarf galaxy sample and the crossmatched ALFALFA/SDSS sample. In fact the lowest SFR bin is offset 1σ above the FML_{SFR} derived from the ALFALFA/SDSS sample. This is suggestive of a breakdown of the FML_{SFR} relation for the lowest SFR galaxies. However, as discussed in Section 3.5.3.1, it is possible that our SFRs are inaccurate in this range considering they are near the limit discussed in Kennicutt and Evans (2012).

3.5.3.4 LZR HI-Mass Dependence (FML_{HI})

We define a fundamental luminosity-metallicity relation (FML_{HI}) using the star formation rate as :

$$\xi_{\gamma} = (M_B) - \gamma(\log(M_{\text{HI}}) - 9.80). \quad (3.20)$$

To find the optimal value of γ , we project the ALFALFA/SDSS data onto the ξ -metallicity plane and bin our data using the same HI-gas mass bins used for Figure 3.7. Each HI-gas mass binned dataset is binned a 2nd time in ξ space similar to the luminosity binning performed in Section 3.5.2 and we once again perform the same cut of 21 galaxies per ξ -HI mass bin. We take the mean metallicity of each ξ -HI mass bin and fit a 4th degree polynomial to the binned mean metallicity values. This process is repeated for values of γ ranging from -2 to 1.

The scatter obtained for each value of γ can be seen in Figure 3.8. We find that a value of $\gamma = -0.50$ provides the lowest scatter for the FML_{HI} (Table 3.3). Using this γ value we then produce the FML_{HI} plot using our optimal projections for Figure 3.11.

For the FML_{HI} relation, we find that our linear fits to the IFU observed dwarf galaxy sample is, within the 1σ uncertainties, consistent with the binned means of the larger ALFALFA/SDSS crossmatched survey, suggesting that the FML_{HI} relation is likely to continue down to luminosities as low as $M_B = -12$.

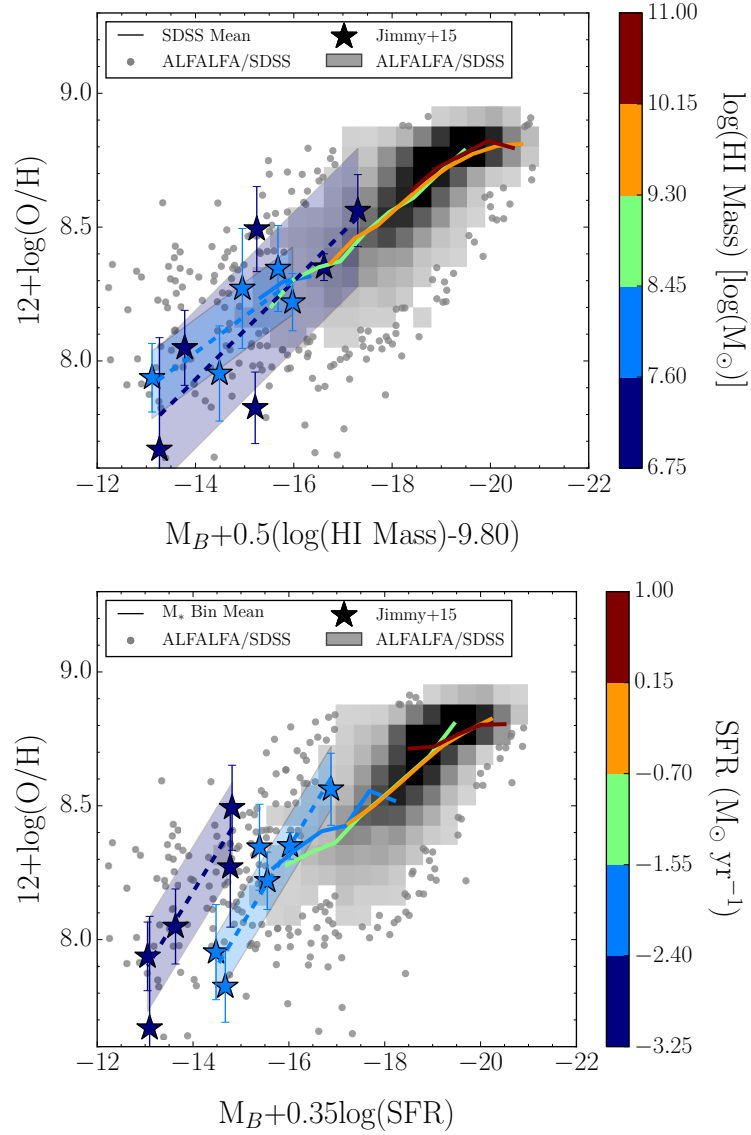


Figure 3.11: FML_{HI} and FML_{SFR} Relations. FML_{HI} (top) and FML_{SFR} (bottom) as calculated using the ζ and γ values found to minimize scatter (Figure 3.10). We find that the FML_{HI} relation is consistent down to the lowest HI-mass bin, where as the lowest SFR bin in the FML_{SFR} is offset 1σ above the FML_{SFR}.

Table 3.3: Best Fitting Fundamental Relation Parameters

μ_α $\log(M_*) - \alpha \log(\text{SFR})$	α 0.28
η_β $\log(M_*) - \beta(\log(M_{HI}) - 9.80)$	β 0.32
ϵ_ζ $(M_B) - \zeta \log(\text{SFR})$	ζ -0.35
ξ_γ $(M_B) - \gamma(\log(M_{HI}) - 9.80)$	γ -0.50

The values that produce the lowest scatter in Figures 3.8 & 3.10.

3.6 Discussion

As can be seen in Figure 3.5, the MZR holds across 5 orders of magnitude in stellar mass, with a 1σ scatter of 0.05 dex. There is an upturn in the MZR around $M_* = 10^8 M_\odot$ which can be explained in the context of the FMR. Galaxies with stellar masses below $10^8 M_\odot$ are likely to have low star formation rates and low HI-gas masses which correlates with higher than average metallicity for a specific stellar mass. For a galaxy with $10^8 M_\odot$, for it to exist in the highest HI-gas mass bin, it would have to have an HI-gas mass 2 orders of magnitude larger than the stellar-mass.

The LZR also holds over 7 magnitudes, with a 1σ scatter of 0.03 dex. A similar upturn can be seen in the LZR around $M_B = -15$. Again this can be explained by the expected low HI-mass and/or low SFR of low luminosity galaxies. The lower scatter in the LZR supports the hypothesis of Berg et al. (2012) that accurately measured

luminosities perform equally as well as stellar-masses.

To provide insight into the most physically motivated components of a fundamental metallicity relation, we examine the 1σ scatter of the means in the larger ALFALFA/SDSS data set for each permutation of mass, luminosity, SFR, and HI-gas mass used to form a possible fundamental relation. Using the scatter of the means around each quartic fit as the evaluation criteria, we find that the lowest scatter of the means is in the combination of stellar mass and HI-gas mass binning (FMR_{HI}) for which we obtain a mean scatter of 0.01 dex, the other three relationships (FMR_{SFR} , FML_{HI} , FML_{SFR}) have mean scatters of 0.02 dex. This suggests that the FMR_{HI} may be the most physically significant fundamental relation.

3.6.1 FMR_{HI}

In examining the FMR_{HI} relation, seen in Figure 3.9 we find that the dwarf IFU sample is consistent within 1 standard deviation with the FMR_{HI} relation observed within the larger ALFALFA/SDSS sample. This suggests that the FMR_{HI} continues to hold down to stellar masses as low as $M_* = 10^{6.5} M_\odot$. Our results suggest that the physical mechanism responsible for the FMR_{HI} must be active across the entire stellar mass range from $10^{6.5}$ to $10^{10} M_\odot$.

Bothwell et al. (2013) reach the conclusion that the FMR_{HI} is more physically motivated due to the reduced scatter and physical motivation of the FMR_{HI} . They also noticed a lack of saturation in the high mass end of the FMR_{HI} . In our analysis, which uses slightly different stellar-mass and HI-mass bins, we do observe saturation in stellar mass bins above $\log(M_*) = 10.0$ in Figure 3.6. We find the FMR_{HI} relation to be more physically motivated due to its behavior on the low mass end ($\log(M_*) < 9.0$) in which the IFU observed dwarf galaxy data is consistent with the larger ALFALFA/SDSS dataset. The 1σ scatter of the FMR_{HI} binned mean metallicities

being the lowest of the 4 permutations supports this hypothesis.

Inflows of pristine gas diluting the metal content would explain why the FMR has an HI-gas mass dependence. Köppen and Edmunds (1999) showed that the gas-phase metallicity of a galaxy can indeed be reduced if the gas infall rate is larger than the rate at which gas is converted into stars. Our results suggest that inflows of pristine gas continue to drive the FMR_{HI} down to stellar masses as low as $10^{6.5} \text{ M}_{\odot}$. This agrees with recent models by Grønnow et al. (2015) which show that pristine gas rich mergers are partially responsible for the scatter in the FMR.

3.6.2 FMR_{SFR}

Unlike the FMR_{HI} , the FMR_{SFR} (Figure 3.9) does not appear to hold across our entire sample. The lowest SFR bin in the IFU observed dwarf galaxy sample is offset 1σ higher than the FMR_{SFR} as determined using the larger ALFALFA/SDSS sample. If our results are accurate near the calibration limits of the SFR and oxygen abundance, they suggest a breakdown in the physical mechanism responsible for the FMR_{SFR} in very low SFR populations.

Possible explanations for the FMR_{SFR} have focused on outflows of metal-enriched gas caused by the intense winds of young star-forming regions within a galaxy. Simulations by Mac Low and Ferrara (1999) have shown that supernova winds are capable of expelling metals efficiently enough to contribute to the MZR. We find that this is likely to be true down to an SFR of $-2.4 \log(\text{M}_{*} \text{ yr}^{-1})$, however, below that it is possible that stellar winds are not sufficiently strong enough to remove metal-enriched gas, and galaxies have a higher gas-phase metallicity than would be expected by the FMR_{SFR} . Although limitations in our measurements could also explain this apparent breakdown.

3.6.3 FML_{HI}

We find that the FMR_{HI} relation, seen in Figure 3.11, is consistent within 1σ between the IFU observed dwarf galaxy population and the larger ALFALFA/SDSS population. These results are similar to those observed for FMR_{HI} however we find that the scatter of the binned $\xi_{-0.5}$ mean metallicities around the quartic fits is larger than the analogous fits for FMR_{HI} suggesting that stellar-mass is the more physically motivated parameter.

3.6.4 FML_{SFR}

The FML_{SFR} relation is inconsistent in both the high ϵ_ζ and low ϵ_ζ regions, as can be seen in Figure 3.9. Similar to the FMR_{SFR} the lowest SFR bin is $> 1\sigma$ offset from the FML_{SFR} relation as determined by the larger ALFALFA/SDSS sample. The highest SFR bin also deviates by as much as 1σ , suggesting that the high mass SFR bin is also poorly fit by the best fitting η in the FML_{SFR} . The inconsistencies observed within the FML_{SFR} relation provide further evidence that HI-gas mass may be the more physically motivated component in a fundamental metallicity relation.

3.6.5 $H\alpha$ Line Flux Limitations

In order to explain the apparent breakdown in the FMR_{SFR} and FML_{SFR} relations for the lowest SFR bins, we consider the possibility that our $H\alpha$ line flux limit may be causing inaccurate SFR estimations. In comparing $H\alpha$ flux measurements between the AoN selected binned spectra and the segmentation map selected binned spectra, we find the segmentation map selection captures approximately 33% more $H\alpha$ flux indicative of low SFR regions being missed. It is also possible that metallicities in the fainter, low SFR, galaxies are over estimated due to limitations in measuring low NII $\lambda 6583$ fluxes, placing them preferentially above the FMR_{SFR} (See Appendix A).

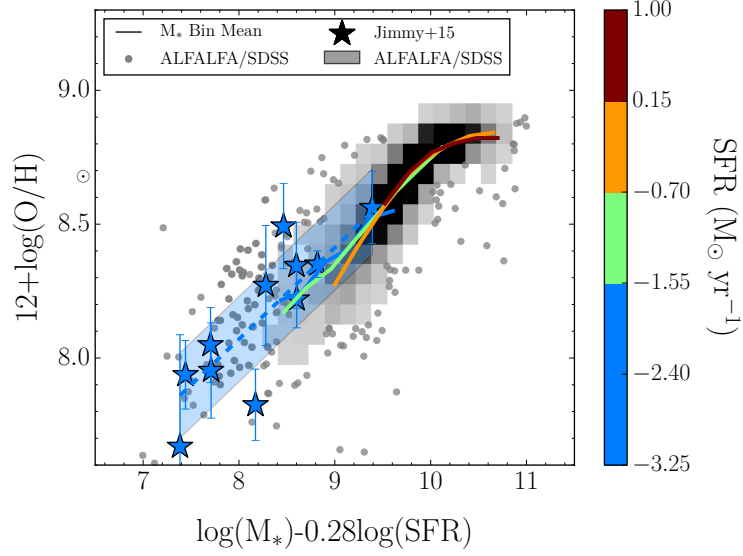


Figure 3.12: FMR_{SFR} With IFU Observed Galaxies in Combined Bin. FMR_{SFR} with the two lowest SFR bins combined into one in order to compensate for the possible underestimation of SFR in the lowest SFR bin of Figure 3.9. We see that in this scenario, the FMR_{SFR} is consistent across the stellar mass range observed.

To test the hypothesis that our lowest SFR bins are underestimated, and our lowest oxygen abundances are overestimated, we re-examine the FMR_{SFR} considering the two lowest SFR bins as one bin. Figure 3.12 demonstrates that the combined bin is consistent with the FMR_{SFR} . Therefore, it is possible that the FMR_{SFR} is indeed valid over the same stellar mass range as the FMR_{HI} however, care must be taken when obtaining IFU observations to ensure that the target depth is sufficient to accurately estimate the SFR and oxygen abundance. To determine whether line flux measurement limitations or physical limitations are the cause of the 1σ offset of the lowest SFR bin, we would require further observations with longer integration times.

3.7 Conclusion

In order to extend the fundamental relations down to stellar masses as low as $10^{6.5} M_{\odot}$ and luminosities as low as -12 mag, we utilize a sample of IFU observed dwarf galaxies in combination with a larger ALFALFA/SDSS crossmatched population of galaxies. Whenever possible, we perform the same analysis on both populations in order to ensure that results are consistent between the two data sets.

When comparing galaxies that overlap between the SDSS and IFU observed samples, we find that IFU observations are necessary to accurately measure the star formation rates of the dwarf irregular galaxies presented here due to the patchy nature of their star forming regions. However, gas-phase metallicities appear to be adequately measured using a single SDSS fiber (Figure 3.4).

Using a sample of galaxies selected from the ALFALFA blind HI survey, in combination with galaxies observed with the VIMOS IFU spectrograph and a selection of long-slit observed galaxies, we investigate the mass-metallicity relation (MZR) with a particular focus on the low stellar mass/low luminosity regime. We find that the MZR continues down to stellar masses as low as $10^{7.25} M_{\odot}$ (Figure 3.5). We find that the MZR has a 1σ scatter in the means around a quartic fit of 0.05 dex.

We find using the ALFALFA/SDSS crossmatched population that the fundamental metallicity relation as a function of SFR (FMR_{SFR}) exhibits its lowest scatter in the means ($1\sigma = 0.02$ dex) when $\alpha = 0.28$. We also find using the IFU observed dwarf galaxy population that the FMR_{SFR} relations appears to break down in the lowest SFR bins (Figure 3.9). However limitations of strong-line metallicity estimations, and $\text{H}\alpha$ based SFRs in low stellar-mass dwarf galaxies may provide an alternative explanation for this apparent breakdown (Section 3.6.5).

We find using the ALFALFA/SDSS crossmatched sample that the fundamental

metallicity relation (FMR_{HI}) exhibits the lowest scatter in the means ($1\sigma = 0.01$ dex) when $\beta = 0.32$. We also find that the FMR_{HI} relations are both consistent between the IFU dwarf population and the ALFALFA/SDSS population across the entire HI-gas mass range.

We find that the luminosity-metallicity relation (LZR) continues down to B-band luminosities as low as -14 mag. We find that the LZR has a 1σ scatter in the means around the quartic fit of 0.03. The lowest scatter in the FML_{HI} is 0.02 dex (for $\zeta = -0.35$). Similarly we find that the lowest scatter in the FML_{SFR} is 0.02 dex for $\gamma = -0.50$.

When comparing our sample of dwarf galaxies to the Mannucci et al. (2010) and Bothwell et al. (2013) analysis, we find that our results are consistent with theirs in that our derived α and β values agree ± 0.04 . In agreement with the conclusions of Bothwell et al. (2013), we find that the FMR_{HI} is more physically motivated than FMR_{SFR} based on the most significant reduction of scatter.

In summary, the FMR_{HI} appears to be the most physically significant driver of the fundamental metallicity relation, suggesting that inflows of pristine gas would be a possible explanation for the fundamental relations observed.

4. SPATIAL CORRELATION BETWEEN DUST AND $H\alpha$ EMISSION IN DWARF IRREGULAR GALAXIES

4.1 Synopsis

Using a sample of dwarf irregular galaxies selected from the ALFALFA blind HI-survey and observed using the VIMOS IFU, we investigate the relationship between $H\alpha$ emission and Balmer optical depth (τ_b). We find a positive correlation between $H\alpha$ luminosity surface density and Balmer optical depth in 8 of 11 galaxies. Our spaxels have physical scales ranging from 30 to 80 pc, demonstrating that the correlation between these two variables continues to hold down to spatial scales as low as 30 pc. Using the Spearman's rank correlation coefficient to test for correlation between $\Sigma_{H\alpha}$ and τ_b in all the galaxies combined, we find $\rho = 0.39$, indicating a positive correlation at 4σ significance. Our low stellar-mass galaxy results are in agreement with observations of emission line regions in larger spiral galaxies, indicating that this relationship is independent of the size of the galaxy hosting the emission line region. The positive correlation between $H\alpha$ luminosity and Balmer optical depth within spaxels is consistent with the hypothesis that young star-forming regions are surrounded by dusty birth-clouds.

4.2 Introduction

$H\alpha$ has many advantages as a Star Formation Rate (SFR) tracer. It does not have the degeneracies that are inherent in Spectral Energy Distribution (SED) fitting techniques, and it is less affected by extinction than SFRs based on the ultraviolet stellar continuum. Finally, $H\alpha$ traces the instantaneous star formation rate, and is relatively insensitive to star formation history. However, dust attenuates the light emerging from star-forming regions (Kennicutt and Evans, 2012). Proper estimations

of galaxy SFRs from $H\alpha$ luminosity rely on our understanding of the quantity, grain-size, and distribution of their dust (Flaherty et al., 2007; Chapman et al., 2009; Shirley et al., 2011).

One must also be careful to make a distinction between attenuation of the stellar continuum and attenuation of ionized gas emission. Throughout this work, we will focus on ionized gas attenuation, as it is most relevant to the Balmer series emission lines that we will be observing. Reddy et al. (2015) found that the divergence between the reddening of the gas emission lines and the stellar continuum increases with increasing SFR. They hypothesize two spatially independent components in galaxies, where stellar attenuation comes from the diffuse Interstellar Medium (ISM), and ionized gas attenuation comes from a higher dust content around localized birth clouds, which increases with increasing SFR.

For galaxies at high redshift ($z > 2$), high spatial-resolution observations are not currently feasible, and therefore assumptions about the distribution of dust, and the dust laws, must be made when estimating the star formation rate. Some studies at intermediate redshift ($z \sim 1-2$) have found good agreement between local dust laws and high redshift dust laws (Scoville et al., 2015; Reddy et al., 2015), although others have suggested geometric or dust grain differences may cause different shapes to the dust law (Kriek and Conroy, 2013; Salmon et al., 2015; Zeimann et al., 2015).

Dwarf galaxies are expected to be Local Universe analogs of the young, gas-rich, star-forming galaxies observed at high redshift. We can use these local galaxies to better understand the high-redshift population as they are both likely to contain little dust and low metallicity. Unfortunately, little is currently known about the dust properties in low-metallicity dwarf galaxies due to the inherent difficulties involved in studying such low-luminosity systems (Walter et al., 2007; Kreckel et al., 2013). ISM dust observations in dwarf galaxies are necessary to build more physically realistic

dust models (Jones, 2015).

The Small Magellanic Cloud (SMC) is similar in mass and star formation rate to the dwarf galaxy population we will be studying, and it is the nearest and well-studied dwarf galaxy. The SMC is known to have a steeper dust law curve than observed in the Milky Way (Gordon and Clayton, 1998; Misselt et al., 1999) or starburst galaxies (Calzetti et al., 2000). Other studies have shown that dwarf irregular galaxies follow a dust law curve more similar to the SMC in their steepness (Walcher et al., 2011). A steeper reddening curve implies that more blue light is preferentially attenuated/extincted.

Starburst galaxies have been shown to exhibit a flatter reddening curve (Calzetti et al., 1994, 2000). Whether the differences between starburst galaxies and the SMC come from clumpy distributions of dust around stars or simply differences in the dust particles themselves (Gordon et al., 1999) is uncertain. Calzetti (1997) supports the hypothesis that younger stars are more strongly attenuated by their birth clouds, while older stars are attenuated by the thin screen of dust in the ISM.

A spatial correlation between SFR and enhanced reddening in ionized regions has been observed in samples of larger spiral and elliptical galaxies (Kreckel et al., 2013; Roche et al., 2015). The dusty birth-clouds that surround star-forming regions have lifetimes comparable to that of the massive stars that dominate $H\alpha$ emission line flux. It is not yet known at which spatial scales this relationship begins to break down.

By combining the spatial distribution of $H\alpha$ and $H\beta$, we can map the influence of dust within each galaxy. Balmer series transitions signify ionized gas regions within star-forming galaxies. These emission line regions are known as HII regions and form near the most massive O stars, and typically have diameters on the scale of 0.1 pc (Wood and Churchwell, 1989). The ionizing photons emitted from HII regions

interact with the surrounding gas and dust to produce the emission lines of interest for this study. The ratio of emission line fluxes for the Balmer series transitions have a known intrinsic value, given reasonable assumptions about the temperature and density of the gas. We can study deviations from this expected value to estimate the influence of dust on light at the wavelengths of $H\alpha$ and $H\beta$. It is typically assumed that $H\alpha/H\beta=2.86$ is the intrinsic ratio, and that this is the lowest physically possible ratio of these two lines.

We present here, for the first time, spatial mapping of the $H\alpha$ emission and the Balmer optical depth in a sample of 11 dwarf irregular galaxies selected from the ALFALFA survey. ALFALFA is a blind HI survey of the local universe (within 250 Mpc; Haynes et al. 2011). The IFU observations of these low stellar-mass objects were taken using the VIMOS IFU spectrograph on the Very Large Telescope (VLT).

The sample of dwarf irregular galaxies was first used in Jimmy et al. (2015) to study the fundamental metallicity relation as a function of HI-gas mass and SFR. We estimated Oxygen abundances of each galaxy using the emission line ratios between $H\alpha$ and [NII]. We found that the dwarf galaxies were all sub-solar metallicity, as would be predicted by the mass-metallicity relation (Jimmy et al., 2015). The median metallicity of all 11 galaxies was $12+\log(O/H) = 8.22$, which is comparable to the metallicity in the SMC ($12+\log(O/H) = 7.98$; Pagel et al. 1978). We also used dust corrected $H\alpha$ emission to estimate the SFR rate for each galaxy, and found a median SFR of $0.005 M_{\odot} \text{ yr}^{-1}$, which is an order of magnitude lower than the SMC ($0.037 M_{\odot} \text{ yr}^{-1}$; Bolatto et al. 2011). The similarities of the dwarf galaxies to the SMC leads us to assume an SMC dust law would be most appropriate for these galaxies.

We test to see if regions as small as $(30 \text{ pc})^2$ exhibit a correlation between higher $H\alpha$ luminosity and enhanced reddening.

4.3 Observations

4.3.1 IFU Spectroscopy

Spectroscopic data of 28 dwarf irregular galaxies were taken using the VIMOS (Le Fèvre et al., 2003) IFU spectrograph on the Very Large Telescope (VLT) located at Paranal Observatory. These galaxies were selected from the ALFALFA survey to be nearby ($D < 20\text{Mpc}$) and low HI-gas mass ($M_{\text{HI}} < 10^{8.2} M_{\odot}$). IFU spectroscopy is necessary to spatially map the reddening and $\text{H}\alpha$ emission throughout each galaxy.

The low stellar-masses and surface-brightnesses of dwarf irregular galaxies makes them difficult to observe. Of the 28 observed galaxies, 11 have Balmer series emission lines greater than our amplitude over noise (AoN) cut of 3 for more than 20 spaxels and therefore are included in this study. Integration times for the remaining 17 galaxies were insufficient to reach our target depth. We find a small HI-gas mass bias between the detected and undetected galaxies in our original sample. The median HI-gas mass for the undetected sample is $10^{7.3} M_{\odot}$ whereas we find an median of $10^{7.6} M_{\odot}$ for the detected sample. The data were obtained starting on April 11, 2008 and ending on May 19, 2010 under program IDs 081.B-0649(A) and 083.B-0662(A). Data were obtained using the VIMOS Low Resolution (LR) Blue Grism which has a wavelength range of 4000-6700 Å and a spectral resolution of 5.3 Å pixel⁻¹ ($R \sim 1000$).

Using the LR Blue grism provides the full 54"x54" field of view possible with VIMOS, which allows us to obtain spectra across the entire stellar disk of each galaxy in a single pointing. Each object was observed using a 3 dither pattern, with each dither being integrated for 20 minutes. Average seeing across all observations is 1.05" FWHM.

The LR blue grism provides both a wider spectral range, and a wider field of view

when compared to the High Resolution blue grism. The LR grism wavelength range allows for simultaneous observations of the emission lines from $H\beta$ ($\lambda = 4861 \text{ \AA}$) to $[NII]$ ($\lambda = 6583 \text{ \AA}$). The major drawback to using the low-resolution spectra ($\sim 5.3 \text{ \AA pixel}^{-1}$) is that we are unable to measure gas kinematics from the emission lines and the instrumental dispersion causes the $H\alpha$ and $[NII] \lambda\lambda = 6549, 6583 \text{ \AA}$ emission lines to blend together.

4.3.2 Data Reduction

The spectroscopic data obtained with the VIMOS IFU is reduced from its raw form using the Reflex environment for ESO pipelines (Freudling et al., 2013). The standard VIMOS template is used within the Reflex environment to produce the master bias and calibration frames containing the fiber traces and wavelength solution. Many of the raw data and calibration frames contain a bright artifact across the surface of the chip, identified to be an internal reflection within the instrument. This contamination interferes with the wavelength calibration routine within Reflex because it is often misidentified as a skyline, causing the spectrum to be shifted incorrectly. To compensate, we disable the skyline shift in the calibration steps. The wavelength solution without using the skyline shift provided by the ESO pipeline proved to be accurate within 5.3 \AA . We also use the flux standardization routine within the Reflex VIMOS pipeline. We then apply the calibration frames to the science frames to produce the fully reduced Row-Stacked Spectra (RSS).

The final output of the Reflex pipeline is four quadrants per observation. We input these individual RSS quadrants into routines written in IDL and Python¹. Further details of the process these scripts follow can be found in Jimmy et al. (2013). After the normalization and sky subtraction steps are completed, the two dimensional RSS are converted into three dimensional data cubes with two spatial

dimensions and the wavelength on the third axis.

Once the data cubes have been built, the individual dithers (typically 3 per galaxy) are stacked using a 5σ clipped mean. We use the AoN to select for spaxels containing sufficient emission line flux for Balmer optical depth measurements. AoN is defined as the amplitude of the emission line divided by the noise after the linear offset is subtracted. An AoN threshold of 3 is used to select spaxels for analysis. Only spaxels which pass the AoN cut in both the $H\alpha$ $\lambda = 6563\text{\AA}$ and $H\beta$ $\lambda = 4861\text{\AA}$ emission lines are included in our analysis.

All spaxels which pass our AoN cut are then fed into Python-based Gaussian fitting routines to measure the emission line fluxes. To obtain the integrated spectrum, we sum the spectra from each spaxel that passes the AoN cut to produce a single spectrum. The procedure that our Python-based Gaussian fitting routines follow is outlined in Jimmy et al. (2015), but we will summarize it here. A linear fit to the continuum is performed in the area immediately surrounding the triplets of emission lines on the blue and red ends of the spectrum (Figure 4.1). We fit 3 Gaussians simultaneously using the `gaussfitter`² routines, fitting the continuum and the Gaussians on the blue end and the red end independently. As described in Jimmy et al. (2015), the Python-based Gaussian fitting routines are able to successfully deblend the $H\alpha$ and $[\text{NII}]$ emission lines.

We do not include a fit to the Balmer absorption in our procedures. Our observations are insufficient to reliably estimate the stellar continuum for accurate absorption measurements. However, it is likely that Balmer absorption effects are negligible and well within our uncertainties (Rosa-González et al., 2002; Reddy et al., 2015). Uncertainties on our flux measurements are estimated using a Monte Carlo technique with 1000 iterations.

²Available publicly: <http://jimmy.pink/#code>

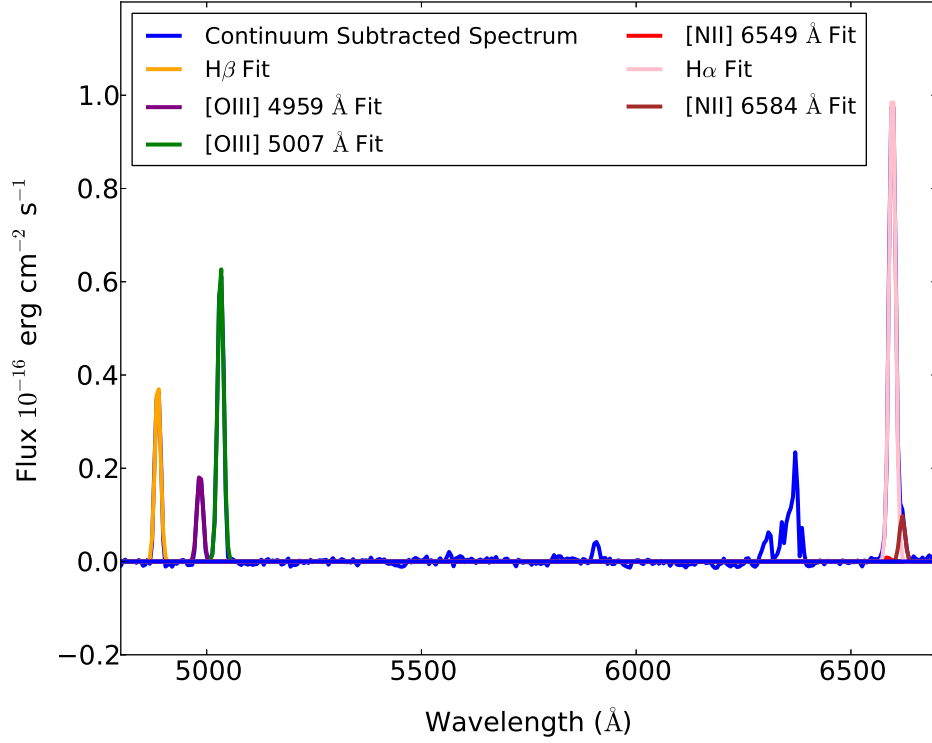


Figure 4.1: Example Result of Python-based Gaussian Fitting Routines. Representative example spectra from a bright spaxel in AGC221000 showing the results of our Python-based Gaussian fitting routines. The [NII] and H α emission lines are blended due to the instrumental resolution (5.3 Å). Our Python-based Gaussian fitting routines are able to deconvolve the three emission lines into their constituent parts, as can be seen by the Gaussian curves plotted. The flux in the red [NII] 6549 Å emission line is negligible. The anomalous feature near 6400 Å is the result of internal reflections within the instrument.

4.3.3 Artificial Galaxy

To ensure that any measured correlation between $H\alpha$ luminosity and enhanced reddening is robust, we have created artificial spectra to represent a galaxy with a constant Balmer optical depth and an exponentially decreasing line flux. This will help us test for possible biases in our data. We test whether or not noise is driving any observed relation between $H\alpha$ and the dust content. Also since we are using the ratio between $H\alpha$ and $H\beta$ as a tracer of the dust, we must ensure that any measured correlation between $H\alpha$ and the dust content is not the result of $H\alpha$ flux also being used to measure the dust content.

The artificial galaxy is created using emission line ratios obtained for NGC 784 A in the Berg et al. (2012) low-luminosity galaxy sample. This galaxy was chosen because the measured Balmer decrement (2.89; Berg et al. 2012) is closest to the range of Balmer decrements in this sample. We scale the brightest central spaxel in the artificial galaxy to have an $H\beta$ emission line flux of $30.0 \times 10^{-16} \text{ erg cm}^{-2} \text{ s}^{-1} \text{ \AA}^{-1}$, which corresponds to the highest $H\beta$ flux in the brightest spaxel of all galaxies in the dwarf IFU sample. Each emission line is given a dispersion equal to the average instrumental dispersion of 7.5 \AA . This galaxy was created to have an exponential decline in both $H\alpha$ flux and $H\beta$ flux with radius, but to keep the $H\alpha/H\beta$ ratio constant throughout.

To create the artificial galaxy, we first take a pipeline reduced data cube from one of the galaxies in our sample that was too faint to be detected by the IFU spectrograph (AGC220261) and find a region of the field of view which contains only sky with little instrumental artifacts. We also check to ensure that none of the galaxy that was originally intended to be observed is located near this region. We

²written by Adam Ginsburg <http://www.adamginsburg.com/pygaussfit.htm>

then generate emission lines to represent an artificial galaxy and place them within this region. The artificial galaxy is then run through the full data analysis procedures described in Jimmy et al. (2015) to measure the recovered emission line ratios.

4.4 Results

Using VIMOS IFU spectroscopy, we are able to produce two-dimensional spatial maps of the physical properties of each galaxy. Using the distances reported from the ALFALFA survey (Table 4.1), we convert the line flux into luminosity measurements to produce spatial mappings of the $H\alpha$ and $H\beta$ luminosities. We also map the Balmer optical depth, defined as

$$\tau_b = \ln \left\{ \frac{H\alpha/H\beta}{2.86} \right\} \quad (4.1)$$

utilizing both the $H\alpha$ and $H\beta$ flux. The $H\alpha$, $H\beta$, and τ_b maps show all the same spaxels, due to the AoN selection criteria that both lines must be detected. Inset within each frame of the spatial distributions is the integrated value, measured by stacking all of the spectra for each spaxel shown. Each figure also shows the artificial spectra created to simulate a galaxy with a constant Balmer optical depth. We have applied the same analysis to the artificial galaxy as the observed galaxies throughout.

Table 4.1: Distance, Mass, and Metallicity Properties of Dwarf Galaxies

Galaxy AGC#	RA (J2000) hh:mm:ss.s	Dec (J2000) ±hh:mm:ss	Distance ^a Mpc (± 2.43)	pc/spaxel (± 8)	HI-Gas Mass ^a log(M _⊙)	Stellar Mass ^b log(M _⊙)	Metallicity ^b 12+log(O/H)	Dust Corrected SFR ^b log(M _⊙ yr ⁻¹)
191702	09:08:36.5	+05:17:32	8.7	28	7.74 ± 0.18	6.67 ± 0.61	7.94 ± 0.13	-2.76 ± 0.34
212838	11:34:53.4	+11:01:10	10.3	33	7.60 ± 0.19	6.94 ± 0.56	8.22 ± 0.11	-2.73 ± 0.32
220755	12:32:47.0	+07:47:58	16.4	52	7.18 ± 1.20	7.76 ± 0.43	8.49 ± 0.16	-2.51 ± 0.64
220837	12:36:34.9	+08:03:17	16.4	52	7.41 ± 0.54	8.78 ± 0.46	8.56 ± 0.13	-2.20 ± 1.28
220860	12:38:15.5	+06:59:40	16.4	52	7.22 ± 1.39	7.57 ± 0.42	7.82 ± 0.13	-2.14 ± 0.14
221000	12:46:04.4	+08:28:34	16.5	53	7.46 ± 0.83	8.35 ± 0.44	8.35 ± 0.05	-1.65 ± 0.08
225852	12:59:41.9	+10:43:40	16.6	53	7.68 ± 0.53	7.57 ± 0.42	8.27 ± 0.22	-2.53 ± 0.38
227897	12:50:04.2	+06:50:51	16.6	53	7.44 ± 0.89	6.58 ± 0.45	7.67 ± 0.42	-2.88 ± 0.24
221004	12:46:15.3	+10:12:20	16.7	53	7.66 ± 0.55	7.98 ± 0.30	8.35 ± 0.16	-2.23 ± 0.22
202218	10:28:55.8	+09:51:47	19.6	63	7.75 ± 0.50	8.12 ± 0.38	8.22 ± 0.11	-1.72 ± 0.29
225882	12:03:26.3	+13:27:34	23.6	76	8.15 ± 0.30	7.06 ± 0.35	7.95 ± 0.18	-2.33 ± 0.05

^a Values obtained from the ALFALFA α .40 catalog (Haynes et al., 2011). Uncertainties in the distances are dominated by the local velocity dispersion measured by Masters et al. 2005.

^b Integrated measurements obtained from Jimmy et al. (2015). These SFR estimations have been corrected for reddening due to dust.

4.4.1 Balmer Line Luminosities

We plot the spatial mapping of the $H\alpha$ luminosity in Figure 4.2. We find integrated $H\alpha$ luminosity values (Table ??) ranging from 38.01 to 39.19 $\log(\text{erg s}^{-1})$, and individual spaxel $H\alpha$ luminosities ranging from 35.27 to 38.02 $\log(\text{erg s}^{-1})$. We find that $H\alpha$ emission is not uniform throughout the ionization regions, but tends to be concentrated within certain sections of the regions. This is consistent with the picture of clumpy star formation within these dwarf irregular galaxies.

If we convert the $H\alpha$ flux using the Hao et al. (2011) calibration between $H\alpha$ luminosity and star formation rate, we would find, without correcting for dust, that the integrated galaxy SFRs are in the range $-3.26 < \log(M_{\odot}\text{yr}^{-1}) < -2.08$. With dust corrections applied, the SFRs range from $-2.88 < \log(M_{\odot}\text{yr}^{-1}) < -1.65$ (Table 4.1). The uncorrected SFRs are near the luminosity limit for this SFR estimation method. Kennicutt and Evans (2012) cautions that below 38 $\log(\text{erg s}^{-1})$ the accuracy of the estimation will degrade as small-number statistics begin to dominate. Therefore, we do not convert our individual spaxel $H\alpha$ luminosities into SFRs, but it is worth noting that our lowest luminosity spaxel, 35.27 $\log(\text{erg s}^{-1})$, is roughly equivalent to the ionizing flux of a single B0V star (Smith et al., 2002).

We also show the $H\beta$ luminosity within each spaxel, calculated from the $H\beta$ line flux and luminosity distance. Once again, no dust corrections have been applied to the luminosity values reported. We observe that $H\beta$ luminosity tends to peak near the center of each individual emission line region. The peak of $H\beta$ flux values are spatially well correlated with the peaks in the $H\alpha$ spatial maps as would be expected. We find integrated $H\beta$ luminosity values (Table ??) ranging from 37.39 to 38.61 $\log(\text{erg s}^{-1})$, and individual spaxel $H\beta$ luminosities ranging from 34.31 to 37.41 $\log(\text{erg s}^{-1})$. We see in Figures 4.2 and 4.3 that the artificial galaxy exhibits

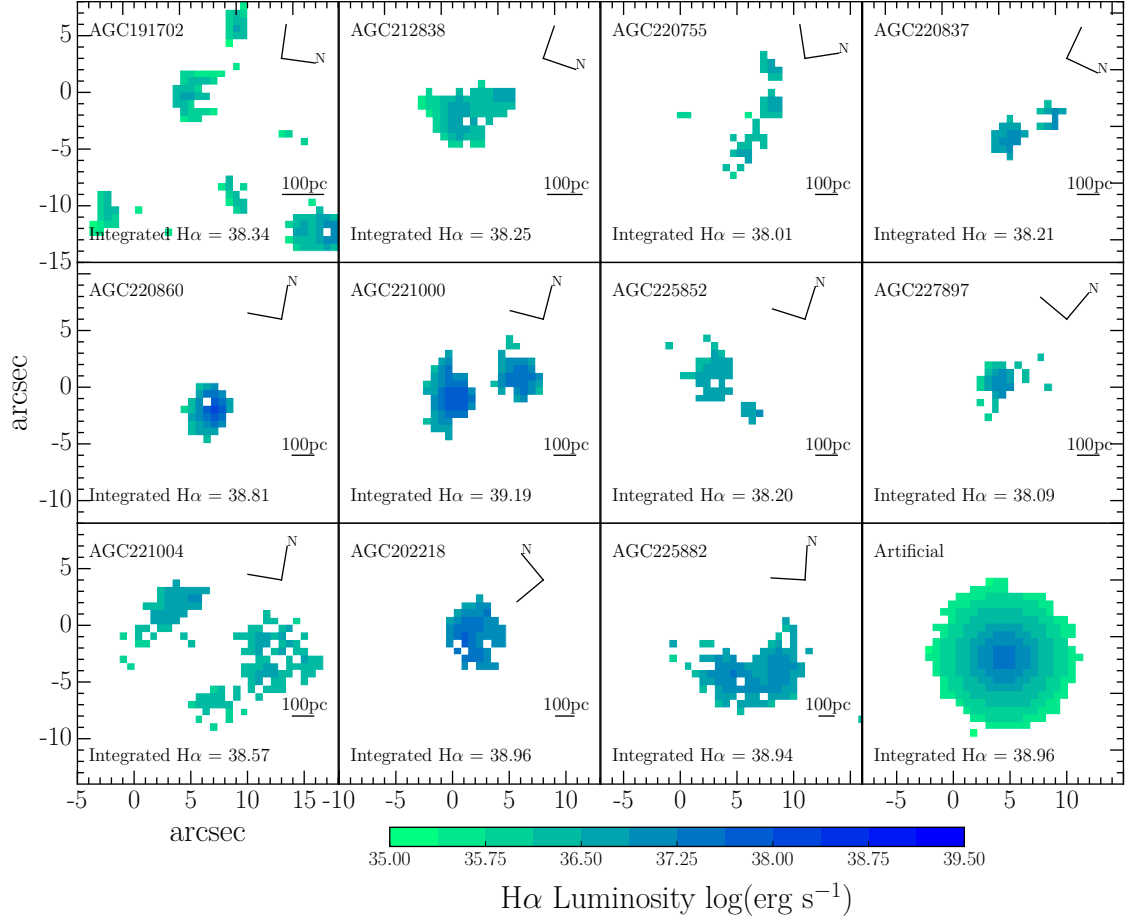


Figure 4.2: Spatial Map of H α Luminosity. Inset within each frame is the log H α flux (erg s^{-1}) measured when summing the spaxels together to form a single effective spectrum. Peaks in the H α flux appear to be spatially correlated with peaks in the Balmer optical depth as seen in Figure 4.4. Also shown in the lower right panel is the artificial galaxy created with an exponential decline in H α flux as a function of radius.

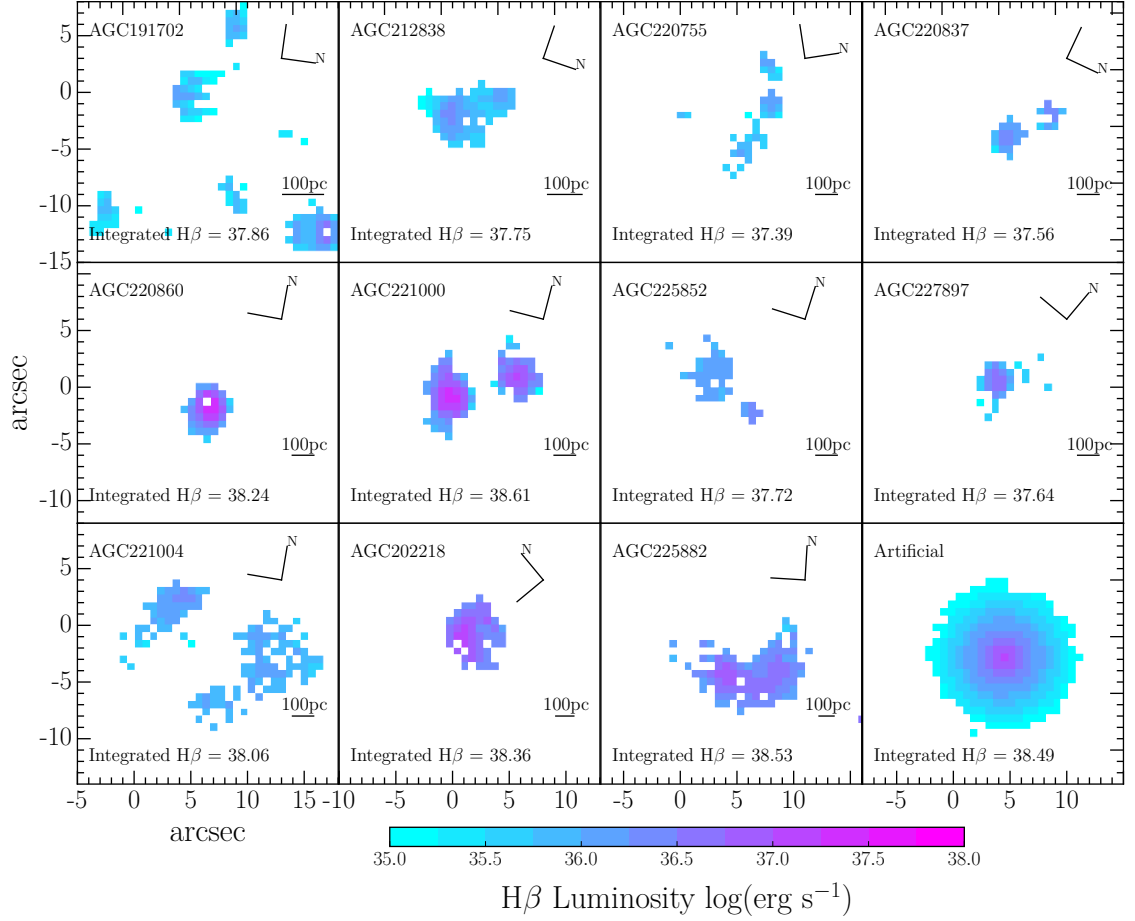


Figure 4.3: Spatial Map of H β Luminosity. Inset within each frame is the \log H β luminosity (erg s^{-1}) measured when summing the spaxels together to form a single effective spectrum. Peaks in the H β emission appear to be preferentially located near the centroids of the emission line regions. Also shown in the lower right panel is the artificial galaxy created with an exponential decline in H β luminosity as a function of radius.

the radial decline in flux that would be expected based on its construction.

4.4.2 *Balmer Optical Depth*

As in Calzetti et al. (1994) and Reddy et al. (2015), we utilize the Balmer optical depth (τ_b) defined in Equation 4.1, which is the difference in optical depths measured at the $H\alpha$ and $H\beta$ wavelengths. Therefore, τ_b is a measurement of the degree of reddening within a region, and is related to the color-excess $E(B-V)$. The theoretical minimum value for Case B recombination at $T = 10^4$ K with an electron density $n_e = 10^2 \text{ cm}^{-3}$ is $\tau_b = 0$ (Osterbrock, 1989).

We use these measurements of the optical depth to spatially map the dust content within each galaxy in Figure 4.4. We also see in Figure 4.4 that the recovered τ_b values for the artificial spaxels produce a dust map that is flat, as it was constructed to be. This is in contrast to the dust distribution in the observed galaxies, which is patchy and irregular. We also provide an integrated τ_b value inset within each image frame, which is obtained by summing the spectra in each spaxel that passes the AoN cut, and measuring the line ratios of the combined effective spectrum. This is roughly equivalent to the Balmer optical depth of the entire galaxy if it were to be observed in a single fiber. It appears that the spaxels with higher $H\alpha$ luminosity correlate with the spaxels containing higher Balmer optical depths (Figures 4.2 & 4.4).

We measure integrated Balmer optical depths ranging from $-0.10 < \tau_b < 0.47$. This range is much smaller than that of observed L^* galaxies at $z = 2$ in Reddy et al. (2015), where they find galaxies in the range $-1.5 < \tau_b < 1.0$. On a spaxel-by-spaxel basis, we find τ_b values ranging from -1.33 to 1.64.

It is apparent that not all emission line regions are the same within dwarf irregular galaxies. If we assume that τ_b can be used as a tracer of the dust content within a

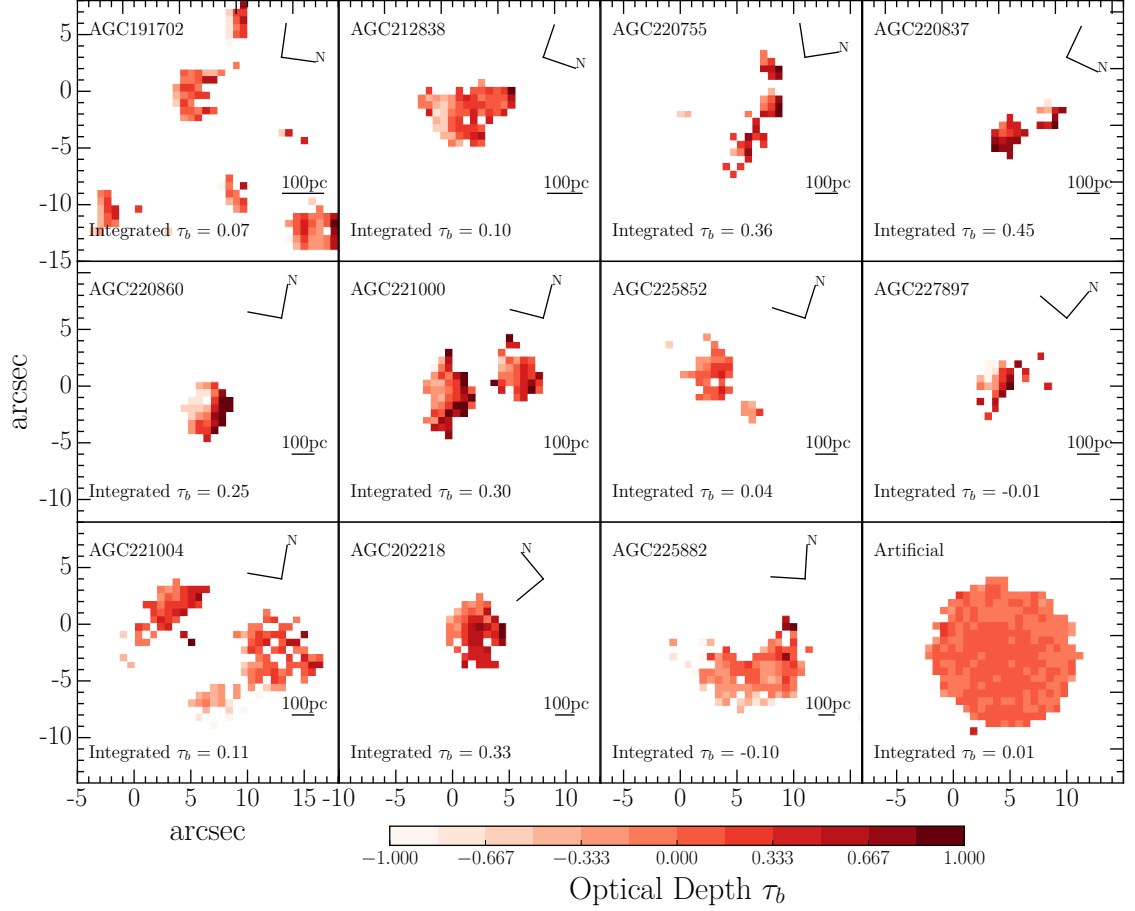


Figure 4.4: Spatial Map of Balmer Optical Depth. Inset within each frame is the Balmer optical depth measured when summing the spaxels together to form a single effective spectrum. Also shown in the lower right panel is the artificial galaxy for which every spaxel was created to have a Balmer optical depth $\tau_b = 0.01$. The observed galaxies show greater variation within their individual spaxels than the artificial galaxy, indicating that the observed scatter is not due to noisy spaxels.

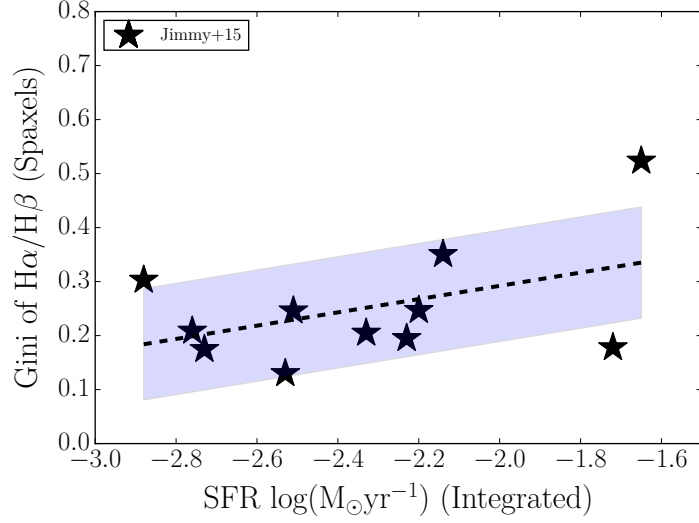


Figure 4.5: Integrated Star Formation Rate vs. Gini Coefficient. The y-axis shows the Gini coefficient of the Balmer ratio ($H\alpha/H\beta$) for the individual spaxels within each galaxy, while the x-axis shows the integrated SFR measured in Jimmy et al. (2015). There is a correlation between the Balmer Gini and total SFR, suggesting that galaxies with higher SFR have less equally distributed dust.

galaxy, we find that the dust is generally not uniformly distributed. Some galaxies exhibit larger internal fluctuations in dust content, whereas others have their dust more uniformly distributed. Galaxies with higher integrated star formation rates, as calculated in Jimmy et al. (2015), tend to have more variability in their internal dust distributions as measured by the Gini coefficient (Figure 4.5). The Gini coefficient is a measurement of the equitability of a distribution ranging from 0 to 1, where 0 represents a flat, perfectly even distribution of dust (Abraham et al., 2003). This positive correlation between SFR and Gini coefficient is consistent with the Reddy et al. (2015) results that higher SFR galaxies have clumpier distributions of dust, which would show preference for a more SMC-like dust law.

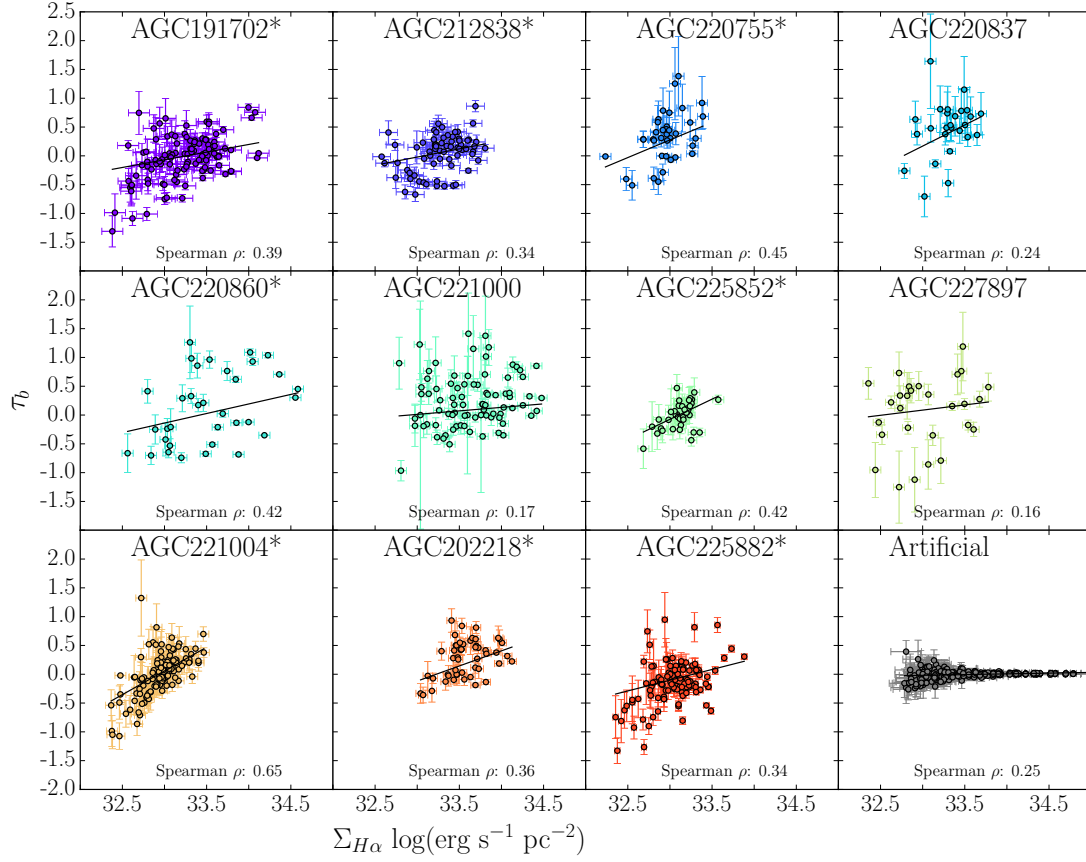


Figure 4.6: $\Sigma_{H\alpha}$ vs. τ_b for Individual Galaxies. There exists a trend between $H\alpha$ luminosity and τ_b for 8 out of 11 galaxies, where asterisks by galaxy names indicate that a positive correlation exists. The artificial galaxy, which was constructed to have a flat τ_b profile, exhibits no correlation.

Table 4.2: Correlation Between $\Sigma_{H\alpha}$ and τ_b in Dwarf Galaxies

Galaxy	Slope	Y-Intercept	ρ	Std Dev from Artificial
191702*	0.27 ± 0.07	-9 ± 2	0.39	1.5
212838*	0.28 ± 0.10	-9 ± 3	0.34	0.8
220755*	0.61 ± 0.24	-20 ± 8	0.45	1.3
220837	0.73 ± 0.35	-24 ± 12	0.24	-0.1
220860*	0.33 ± 0.16	-11 ± 5	0.42	1.0
221000	0.12 ± 0.07	-4 ± 2	0.17	-0.8
225852*	0.70 ± 0.18	-23 ± 6	0.42	1.1
227897	0.18 ± 0.23	-6 ± 8	0.16	-0.5
221004*	0.82 ± 0.10	-27 ± 3	0.65	5.8
202218*	0.52 ± 0.14	-17 ± 5	0.36	0.8
225882*	0.37 ± 0.10	-12 ± 3	0.34	1.0
Artificial	0.03 ± 0.01	-1 ± 1	0.25	0.0
All Spaxels*	0.26 ± 0.03	-8 ± 1	0.39	4.0
Integrated	0.23 ± 0.18	-7 ± 6	0.20	-0.2

Galaxies with an asterisk by their name indicate those for which the correlation between $\Sigma_{H\alpha}$ and τ_b is significant.

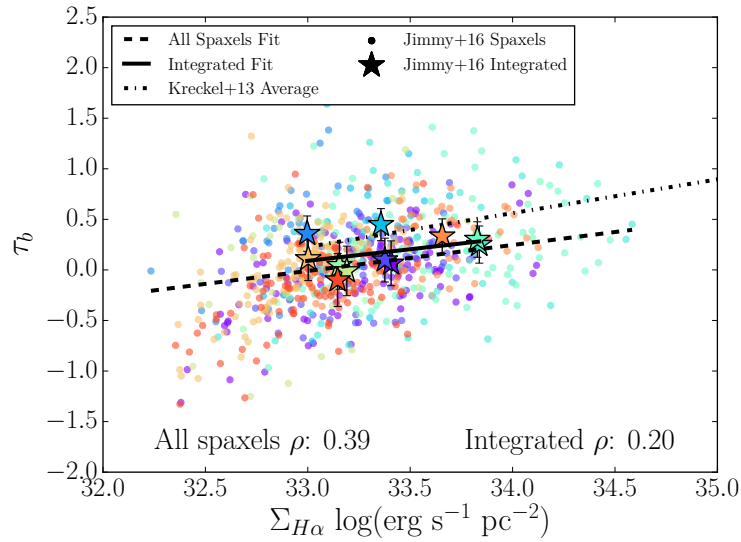


Figure 4.7: $\Sigma_{H\alpha}$ vs. τ_b All Spaxels Fit. $H\alpha$ surface density and Balmer optical depth for the individual spaxels (dots) using the same color scheme as Figure 4.6. Also plotted is the mean of the relations found in Kreckel et al. (2013, dot-dash) which has a larger spatial scale, and shows a very similar slope. For comparison, we have included the integrated values of each galaxy (stars). The slope of the integrated values fit is similar to that of the fit to the individual spaxels.

4.4.3 Correlation Between $H\alpha$ and τ_b

We test to see if $H\alpha$ luminosity and the Balmer optical depth are correlated on a per-spaxel basis, as well as (using the integrated fluxes) a galaxy-by-galaxy basis. To account for the effects of observing galaxies at varying distances with varying spatial resolution scales, we divide each measurement by the surface area to show the $H\alpha$ luminosity surface density ($\Sigma_{H\alpha}$) in Figure 4.6. The $H\alpha$ surface density is defined as $\Sigma_{H\alpha} = L_{H\alpha}/(s^2 \cdot n)$ where $L_{H\alpha}$ is the $H\alpha$ luminosity, s is the physical size of the spaxel in pc, and n is the number of spaxels in the bin. We find that there is a general trend towards spaxels with higher $\Sigma_{H\alpha}$ having higher τ_b values. We fit the spaxels using the `curve_fit` routine from SciPy to perform a weighted least-squares linear fit to the individual spaxels in Figure 4.6 and report our results in Table 4.2. The `curve_fit` routine determines the best fit by minimizing the sum $\sum ((f(x) - y)/w)^2$ where $f(x)$ is the function being fit, y is the y-axis values, and w is the uncertainties in the y-axis values. Using a linear function as $f(x)$, all galaxies exhibit either a flat or positive slope. In Figures 4.6 and Table 4.2, the slope of the artificial galaxy differs significantly from the slopes of the observed galaxies, indicating that low S/N spaxels are not primarily driving the apparent relation between $\Sigma_{H\alpha}$ and τ_b .

We test for correlation using Spearman's rank correlation coefficient (ρ), as provided by the SciPy routine `spearmanr`. Similar to the Pearson correlation coefficient, the Spearman coefficient can range in value from -1 to 1. We use the Spearman coefficient because it does not require that the distribution of the data be Gaussian in nature, like the Pearson correlation coefficient does. Our x-axis values are not Gaussian in that there are generally more low luminosity spaxels than high luminosity spaxels.

Typically, the following criteria are used to determine the significance of ρ values:

$0.10 < \rho < 0.29$ is a weak association, $0.30 < \rho < 0.49$ is a moderate association, $\rho > 0.50$ is a strong association (Cohen, 1988). The artificial galaxy was constructed to have no correlation between the two values, and exhibits a $\rho = 0.25$, consistent with a weak correlation, and indicative that these significance thresholds are accurate. Based on the low Spearman rank coefficient in the Artificial galaxy, we conclude that using $H\alpha$ to calculate τ_b is not the primary driver of the relation between $H\alpha$ and τ_b . Therefore, we consider any ρ value above 0.29 to be indicative of a positive association.

In addition, we use the ρ value found for the Artificial galaxy to perform a null-hypothesis test, where we use the Spearman coefficient of the Artificial galaxy as our null value, and determine the number of standard deviations each galaxy's ρ measurement is from the Artificial galaxy. Performing a Fisher z-transformation on both the control data and the observed data allows us to determine the significance of the separation as $\sigma = z(\rho) - z(\rho_0) * \sqrt{n - 3}$. We report these standard deviations from the null hypothesis as the final column in Table 4.2. The factor of $\sqrt{n - 3}$ in the numerator indicates that the statistical significance of the deviation from the control is dependent upon the number of spaxels (n) for a given galaxy.

Based on this criteria, we find for 8 out of 11 galaxies that the spaxels have a statistically significant correlation between the observed $H\alpha$ luminosity surface density and the Balmer optical depth. These galaxies are indicated with an asterisk in Table 4.2. There does not appear to be any correlation between galaxy distance and ρ , indicating that our results are not dependent upon spatial resolution. The 3 galaxies that do not appear to follow the positive correlation between $\Sigma_{H\alpha}$ and τ_b (AGC221000, AGC220837, and AGC227897) do not appear to have any particular commonalities. They vary widely in stellar mass and metallicity as can be seen in Table 4.1. They have 3 of the 5 lowest HI-gas masses, however, both AGC220860

and AGC220755 have lower HI-gas mass than those 3 galaxies (Table 4.1) and do appear to follow the $\Sigma_{\text{H}\alpha}$ and τ_{b} correlation.

The number of spaxels for each galaxy ranges from 26 to 130, so in some galaxies such as AGC220837 and AGC227897 there may not be enough spaxels to reliably derive a slope to this relation, as is evident by the low significance of the deviation from the Artificial galaxy. Therefore, we combine all spaxels from all of the galaxies to form Figure 4.7. When performing a linear fit we find a statistically significant correlation between the two values with a slope of 0.26 ± 0.03 (Table 4.2). The Spearman rank coefficient of the aggregate spaxels is 0.39, higher than the Artificial galaxy, indicating a moderate correlation at the 4σ level when averaging over all spaxels within our sample.

We also provide the results of a linear fit to the integrated values. The slope found for the linear fit to the integrated values for each galaxy is similar to that of the individual spaxels. With only 11 points in the integrated values fit, it is difficult to draw any robust conclusions, as is indicated by the low significance (0.2σ) for the integrated spaxels. Although we must caution that the low sigma value does not indicate that the relation itself is insignificant, rather that the number of data points we're using to calculate the Spearman coefficient is low, and therefore the factor of $\sqrt{n-3}$ will be low.

4.5 Discussion

4.5.1 Increasing Attenuation with Increasing $\text{H}\alpha$ Luminosity

The correlation between enhanced reddening and higher $\text{H}\alpha$ luminosity within individual spaxels indicates that dustier regions correlate with higher SFR regions. This correlation has been observed in larger galaxies (Kreckel et al., 2013), but we have shown for the first time that it holds true for gas-rich dwarf galaxies (Figure

4.6). Our slope is within 2σ of the mean of the Kreckel et al. (2013) data (0.32, Figure 4.7), which was focused on emission line regions within more massive spiral galaxies.

Kreckel et al. (2013) predicted, based on the lack of high Σ_{SFR} regions having low A_V , that HII regions are likely to be correlated with the dust on 20-120 pc scales, but the physical resolution of their data was limited to 100 pc. Using our 30-80 pc resolution IFU spectroscopy, we are able to confirm their hypothesis that emission line regions and dust are well correlated on those scales for 8 of 11 galaxies. It is unclear at which physical scale this relation will break down. Kreckel et al. (2013) also compared emission line regions to stellar continuum as dust tracers and concluded that emission line regions were a better tracer. We are able to investigate effects smaller than 100pc in diameter, the nominal size of the giant molecular clouds that form small clusters of stars. However, we are unable to probe down to sizes of ~ 10 pc, the size of cores that form individual stars (Tan, 2015).

It is likely that the correlation between $\Sigma_{H\alpha}$ and τ_b is caused by the young stars within these emission line regions being surrounded by the dusty birth-cloud in which they formed. If dust obscuration traces instantaneous star formation, then the physical effect causing this must be acting on similar time-scales. The cloud of gas and dust that the young star formed from will not be entirely consumed in the formation of the star, and it takes time (approximately 30 Myrs, on par with the lifetime of an O or B type star) for the dust cloud to dissipate (Charlot and Fall, 2000).

We have also shown that galaxies with higher star formation rate have more internal dispersion in their dust measurements (Figure 4.5). This is consistent with the physical conditions thought to create a steeper SMC-like reddening curve (Reddy et al., 2015). This fact is important for high-redshift galaxies ($z > 2$), for which we are unable to measure the spatial distribution of the dust content. If the highest $H\alpha$

flux regions also have the clumpiest dust distributions, then in high redshift galaxy surveys, we may be over-estimating the galaxy-wide dust obscuration.

We observe that the slope is similar, within the uncertainties, between the spaxel-by-spaxel relation and the integrated values relation. The Spearman ρ for the integrated galaxies is not significantly different from the Artificial galaxy we used to formulate our null hypothesis. Other studies (e.g. Reddy et al. 2015) have shown that dustier galaxies have higher $H\alpha$ luminosity on integrated galaxy-wide scales.

Our results agree with the conclusions of Kreckel et al. (2013) that emission line sources are preferentially located within dusty birth clouds. Similarly Reddy et al. (2015) found that their results were consistent with a two population model. Firstly a modestly reddened underlying stellar population, with a second dustier stellar population that begins to dominate the nebular line luminosity with increasing SFR. Our results align with this view, although it would be advantageous to compare our emission line measurements to stellar continuum measurements, we do not have the UV observations that would be necessary to properly constrain our data. Based on the spatial agreement between the peaks in the Balmer optical depths and the $H\alpha$ luminosity, it is likely that the star formation rates within our dwarf irregular galaxy population are not powerful enough to have a well-mixed ISM for the majority of our sample. We note that galaxies with super strong outflows, like NGC 2146 from Kreckel et al. (2013) exhibit spatial offsets in their dustiest regions and their highest $H\alpha$ regions. NGC 2146 also shows near agreement between stellar continuum reddening and gas emission line reddening, suggesting that stellar winds have blown away the clouds of gas and dust and the emission lines experience a grayer dust attenuation.

4.5.2 Negative τ_b Values

As can be seen in Figures 4.4, 4.6 & 4.7, a large number of the spaxels within each galaxy exhibit τ_b values that are seemingly unphysical. It would appear that either $H\alpha$ is being over-estimated or $H\beta$ is being underestimated. The following possibilities were considered as the cause of the negative τ_b values observed:

- **Poor Gaussian Fits:** We have checked all of the fits to each spaxel spectrum to verify that the Gaussians do indeed provide a reasonable fit to the data, and find no obvious source of error from mis-measurement of the flux values. We also checked to ensure that our de-convolution of the blended $H\alpha$ and [NII] emission lines was not a cause by fixing the ratio of the three lines to the integrated value and re-measuring all of the spaxels with no significant difference in our results. Even if that were a factor, it would only serve to increase the $H\alpha$ flux with any corrections, and that would further exacerbate the issue.
- **Shocks of the ionized gas** would cause a change in the [NII]/ $H\alpha$ ratio, however our Python-based Gaussian fitting routines allow the ratio between $H\alpha$ and [NII] to vary on a spaxel-by-spaxel basis.
- **Line Sensitivity:** We have also observed in our artificial galaxy that low flux spaxels are not significantly lower in τ_b (Figure 4.6) so it is unlikely that this is a line-sensitivity effect.
- **Instrumental Effects:** We created a field of random emission lines within a blank data cube to confirm that there are not issues with certain spaxels, or gradients across the field-of-view or CCD.

- Balmer Absorption: We also considered that our assumption of Balmer absorption being negligible was at fault, however, Balmer absorption more strongly affects $H\alpha$ than $H\beta$, so any corrections we apply to account for absorption will create only lower τ_b values.

We are therefore reasonably confident that the τ_b values we are measuring are accurate representations of the observations.

Typically studies will assume that a ratio of $H\alpha/H\beta < 2.86$ is indicative of little to no dust within a galaxy, and for the purpose of their analysis treat negative Balmer optical depths as 0 (e.g. Reddy et al. 2015). Another typical approach is to state that the intrinsic ratio between $H\alpha$ and $H\beta$ varies as a function of electron temperature and density (e.g Battisti et al. 2016). However, as we will show, this is typically a small effect, and insufficient to explain all negative τ_b values. Due to the large number of individual spaxels within our sample with $\tau_b < 0$, we cannot ignore, or make the “no dust” assumption, for all of negative τ_b spaxels. This then leads us to speculate on the cause of the negative τ_b values.

The minimum value of 2.86 for the ratio of $H\alpha$ to $H\beta$ from Osterbrock (1989) assumes three important factors, Case B recombination (meaning that the gas is optically thick to Lyman alpha photons), electron temperature $T_e = 10,000\text{K}$, and electron density $n_e = 10^2 \text{ cm}^{-3}$. Changing our assumption to Case A recombination, in which Lyman alpha photons can readily escape, is likely not a solution as such a galaxy would be very low surface brightness and difficult to observe (Aller, 1984). If we continue to assume Case B recombination and allow the temperature to vary, we find that increasing the assumed temperature can lower the ratio, such that if we double the temperature to $T_e = 20,000\text{K}$, we find $H\alpha/H\beta = 2.76$. This is not sufficient to explain the negative τ_b values. If we were to additionally alter our

assumption and increase the density of electrons to $n_e = 10^6 \text{ cm}^{-3}$ we would find again only a marginal effect, with the new theoretical minimum $H\alpha/H\beta = 2.72$. With the Balmer decrement being relatively insensitive to the assumptions we are making, we conclude that the negative τ_b values are not likely caused by incorrect assumptions of the emitting gas.

We then speculate that the possible cause of our negative τ_b values may be due to scattering of blue light from within the dusty birth clouds to regions of the galaxy that have less dust, and also fewer young O and B type stars capable of producing the ionizing radiation to induce the Balmer series of emission lines. Regions that have less Balmer series emission overall would be more sensitive to even small increases of scattered $H\beta$ flux originating from within the very active and dusty regions.

4.6 Conclusion

We have continued of our study of 11 IFU observed dwarf galaxies first reported on in Jimmy et al. (2015), where we studied the fundamental metallicity relation as a function of HI-gas mass and star formation rate. This sample was selected to have low HI-gas mass ($M_{HI} < 10^{8.15} M_\odot$), and as such exhibits low stellar-mass, low metallicity, and low SFR (Table 4.1). We continued our observations within this work by studying the $H\alpha$ and $H\beta$ luminosity, in addition to the Balmer optical depth (τ_b). We measured integrated $H\alpha$ luminosities ranging from $38.01 < \log(H\alpha) < 39.19$ erg s^{-1} and integrated τ_b values in the range $-0.10 < \tau_b < 0.47$ (Table ??).

Dust curves are used to correct for the attenuation of light when determining star formation rates. This attenuation is affected by the distribution of dust within the ISM of galaxies, as well as the composition and size of the dust grains themselves. Gas-rich star forming galaxies are likely to have their bluest star-forming regions surrounded by dusty birth clouds, which will preferentially scatter and absorb the

blue light, causing a steeper dust attenuation law of the ionized gas emission, as observed in the Small Magellanic Cloud.

Utilizing the spatial information provided by IFU spectroscopy, we mapped the reddening properties of these dwarf irregular galaxies (Figure 4.4). We found that the regions of the galaxy with more reddening positively correlate with regions of enhanced $H\alpha$ emission. This correlation has been demonstrated before in larger spiral galaxies (Kreckel et al., 2013), however, we have shown that the correlation between SFR and dust in emission line regions likely continues to hold even in gas-rich dwarf galaxies. Using Spearman’s coefficient, we quantified the degree of correlation between $\Sigma_{H\alpha}$ and τ_b . We found 8 out of 11 galaxies showed a positive correlation between these two values. If we test for a correlation within all spaxels from all galaxies at once, we find $\rho = 0.39$ with 4σ significance in deviation from our null hypothesis derived from the Artificial galaxy (Table 4.2). We demonstrated that this correlation continues to hold in low mass galaxies, down to physical scales as low as 30pc. Higher spatial resolution observations of similar dwarf galaxies would help determine the physical resolution at which this relationship breaks down.

We also discussed the possibility that the negative τ_b values we measured may be indicative of low-luminosity regions having blue light scattered into them, causing seemingly unphysical τ_b measurements within some of our spaxels.

This is the first study to specifically target local universe, gas rich, dwarf irregular galaxies for a correlation between $\Sigma_{H\alpha}$ and τ_b . Because these galaxies are local analogs to the high-redshift galaxies currently being observed, we have shown that assuming a simple uniform dust distribution within high-redshift star forming galaxies is likely to be inaccurate. The degree of clumpiness within a galaxy can likely be estimated by the dust content within a galaxy. As predicted by Reddy et al. (2015), galaxies with larger SFRs exhibit a higher dispersion in their Balmer

decrements as the dust obscuration becomes more patchy with the rise of a second, dustier, population (Figure 4.5). The clumpiness of our observations would suggest an SMC type reddening curve is most appropriate for low-metallicity dwarf irregular galaxies. Additionally our dwarf irregular galaxies have similar SFRs, stellar-masses, and metallicity as the SMC. Although it is important to note that we are unable to resolve individual stars with our observations, so it is possible that other physical effects such as grain size or composition that we are unable to explore may reproduce these same conclusions.

Assuming that young star forming galaxies at high redshift also have their star forming regions surrounded by dusty birth-clouds, we would argue for a steeper SMC-like dust law for those galaxies as well.

5. SUMMARY

We endeavor to better understand galaxy formation and evolution by focusing on the behavior of baryons within galaxies on either extreme end of the stellar-mass spectrum. The grand scale of galaxies, containing literally billions and billions of particles, makes it impossible to study the individual baryons themselves, which is why we turn to the scaling relations of observable properties within galaxies that allow us to better understand the various phases of galaxy evolution. Because we cannot study a single galaxy evolving, we must examine galaxies at various phases of their evolution to understand the life of a galaxy. We examine the formation and evolution of galaxies using IFU derived absorption-line spectra to study the stellar continuum of brightest cluster galaxies, and emission-line spectra from the ionized gas of dwarf irregular galaxies.

We have demonstrated the validity of scaling relations acting on extreme populations such as the angular momentum and stellar mass relation (Chapter 2), the stellar mass and metallicity relation (Chapter 3), and the star formation and dust relation (Chapter 4). Many scaling relations are initially developed using “typical” galaxies which are the most abundant, easily observed, and well-behaved galaxies. However, we show that these relationships are consistent even in the most extreme conditions.

We utilize integral field unit (IFU) spectroscopy to obtain our observations. We focus our attention on two distinct galaxy populations, brightest cluster galaxies (BCGs) which are some of the most massive galaxies in the universe, and dwarf irregular galaxies, which are very low stellar-mass galaxies. The added benefit of IFU spectroscopy is that we are able to obtain two-dimensional spatial maps of the

observed properties for both populations of galaxies. This allows us to spectrally observe the entire surface of a galaxy using a single pointing, whereas other observational techniques would either have to sacrifice information or use an inordinate amount of telescope time.

Three large-scale IFU surveys are currently in progress, SAMI, MANGA, and CALIFA. Each survey has its own strengths and weaknesses for legacy value, as they are all focused on slightly different scientific goals. SAMI is focusing on the role of environment in galaxy evolution, MANGA is focusing on obtaining a statistically robust sample of IFU observations of Local Universe galaxies, and CALIFA is focusing on the star formation histories and gas flows within galaxies. However none of them specifically target BCGs which are rare in the universe and likely to constitute only a small portion of the sample (e.g. only 1 BCG is in the ATLAS^{3D} sample). Dwarf galaxies will also be largely absent in these surveys due to the difficulties inherent in observing low-luminosity galaxies. Even with the relatively low mass selection of SAMI, they will still only be able to detect the largest of the dwarf galaxy population.

We choose to specifically target these galaxies because they are generally under-represented in galaxy surveys. For instance, ATLAS^{3D} has only 1 BCG in their sample of 260 early-type galaxies, so by adding complimentary observations of 10 addition galaxies, we overwhelmingly increase the sample size of BCG kinematics being studied with IFU spectroscopy. BCGs are a population of interest because of their unique formation history and extremely large masses. Despite their large mass, they are often difficult to observe because of their low surface-brightness at large radii. Due to the rarity of BCGs, a large volume of space is necessary to observe a representative samples of BCGs. Large scale surveys such as those discussed above are likely to target the easiest to observe galaxies, which are also more likely to guarantee high signal-to-noise observations without an inordinate amount of observing

time. A similar problem exists for dwarf irregular galaxies, they are also low surface-brightness due to their diffuseness and low stellar-mass. Dwarf irregular galaxies are uniquely gas-rich and metal-poor, making them an interesting population because they represent the local universe equivalent of young, high-redshift galaxies.

5.1 Brightest Cluster Galaxy Mergers and Kinematics

To understand the role that mergers play in galaxy formation and evolution, we study the objects which are likely to have undergone the largest number of mergers. Brightest cluster galaxies (BCGs) are the largest galaxies in the universe, and sit at the bottom of their host cluster’s potential well. The extreme environment of BCGs makes them crucial to understanding galaxy formation. Using VLT/VIMOS high resolution IFU observations of 10 BCGs, located within 400 Mpc, and selected to have nearby companion galaxies, we analyze their stellar kinematics and search for galactic scale rotation, as observed recently in early-type galaxies (Emsellem et al., 2007, 2011). We compare our observations to the SAURON and ATLAS^{3D} surveys, two of the recently completed IFU surveys. ATLAS^{3D} reported that a surprising percentage (86%) of early-type galaxies were fast rotating (Emsellem et al., 2011). For comparison, in our sample of 10 BCGs we find that 30% are fast rotating, which is considerably lower, however our sample is biased towards higher masses. When we select only galaxies in the same stellar mass range ($M_{dyn} > 11.5M_{\odot}$), we find no statistical difference between the number of fast rotating galaxies between the two samples.

To better quantify the merger status of brightest cluster galaxies, we investigate the photometry of our galaxies using SDSS imaging and the G-M₂₀ selection criteria (Lotz et al., 2008) to search for abnormalities in the distribution of light which signals a merger. We hypothesized that the rotation observed within our sample of

BCGs may be due to current or very recent mergers causing the appearance of a rotating galaxy. In our sample of BCGs there is no connection between the angular momentum and the $G-M_{20}$ merger selection criteria. The lack of correlation between angular momentum and recent mergers, as well as the similarities between the BCG and early-type galaxy samples leads us to conclude that mergers are not the primary driver of the angular momentum loss observed in BCGs. This is consistent with simulations by Naab et al. (2014) and observational results of Oliva-Altamirano et al. (2015) that BCGs have very diverse formation histories that produce their present day kinematical structures.

5.2 Dwarf Galaxy Fundamental Metallicity Relation

We then shift to the opposite end of the mass spectrum and focus on the baryon cycle of dwarf irregular galaxies. We utilize a sample of 11 IFU observed dwarf galaxies in the stellar mass range $10^{6.6}$ to $10^{8.8} M_{\odot}$, with metallicities as low as $12+\log(O/H) = 7.67$. All of these galaxies are located within 25 Mpc, and were selected to be gas-rich ($10^{7.2} M_{\odot} < M_{HI} < 10^{8.2} M_{\odot}$) star-forming galaxies. We rely upon strong-line emission from $H\alpha$ and $[NII]$ to estimate the oxygen abundance of the dwarf irregular galaxies. Using these data, in combination with data taken from SDSS and the literature, we are able to examine the mass-metallicity relation in a sample of extremely low stellar-mass galaxies (as low as $10^{6.5} M_{\odot}$). The advantage of having IFU data over the spectroscopy provided by the SDSS pipeline is that we are able to integrate the light over the entire surface of a galaxy, whereas SDSS is only able to spectroscopically observe a small $3''$ portion of each galaxy, usually the brightest region. This observation bias is likely to significantly influence results in patchy galaxies such as the dwarf irregular galaxies of interest to this study.

The mass-metallicity relation is known to exhibit increased scatter beyond the 1σ

uncertainties of the data (Tremonti et al., 2004), suggesting that some other physical process may be relevant to the inflows and outflows that produce the mass-metallicity relation. By incorporating a 3rd parameter into the mass-metallicity relation we are able to observe a three-dimensional fundamental metallicity relation (FMR). By finding the optimal projection of the FMR into 2D space (i.e. the projection with the lowest residual scatter) we can determine whether inflows of pristine gas or outflows from high star forming regions are driving the scatter in the mass-metallicity relation. We find that HI-gas mass is a more physically motivated tracer of the FMR based on the reduced scatter, and consistency across a wide range of HI-gas masses, whereas SFR exhibits a possible breakdown for galaxies with SFRs $< 10^{-2.4} \text{ M}_{\odot} \text{ yr}^{-1}$. We show that the HI-gas fundamental metallicity relation is likely valid down to small, metal-poor dwarf irregular galaxies with stellar masses as low as $10^{6.5} \text{ M}_{\odot}$ which are analogs of the early universe galaxies that were consumed by BCGs. This is compatible with recent evidence that infall of pristine gas is the more dominant component at high redshift (Agertz et al., 2009; Bournaud and Elmegreen, 2009; Brooks et al., 2009; Dekel et al., 2009).

5.3 Dust Distribution within Dwarf Irregular Galaxies

Using the same sample of IFU observed dwarf galaxies from the mass-metallicity relation study, we map the dust content within these galaxies by measuring the Balmer optical depth which is defined as the natural log of the ratio between $\text{H}\alpha$ and $\text{H}\beta$ emission line fluxes. The IFU observations allow us to map the dust content and the star formation simultaneously. It has been shown in much larger galaxies that the HII regions exhibit a correlation between the Balmer decrement and the $\text{H}\alpha$ luminosity (Kreckel et al., 2013). Regions with higher star formation appear to have enhanced reddening due to dust. We have confirmed that this correlation

between $H\alpha$ surface density and Balmer optical depth continues even down to masses as low as those observed the irregular dwarf galaxy population ($10^{6.6} M_{\odot} < M_{*} < 10^{8.8} M_{\odot}$), and that the trend can be seen on physical scales as small as 30 pc. The positive correlation between $\Sigma_{H\alpha}$ and τ_b is consistent with the hypothesis that young star-forming regions are surrounded by dusty birth-clouds and in agreement with recent results by Reddy et al. (2015) of an empirical scaling relation between the star formation rate and the dust mass in the ISM of galaxies. If this effect is not taken into account, star formation rates in highly star forming galaxies may be underestimated.

5.4 Future Prospects

5.4.1 Angular Momentum of Clusters Vs. BCGs

In reducing the data for our original dataset of 10 BCGs, we notice that for the BCGs in which we were able to measure the angular momentum of the companions, it appears that the angular momentum of the companions moving around the cluster match the angular momentum of the BCGs. This suggests that the angular momentum of the BCG may be preferentially aligned to the angular momentum of the cluster. If the companion galaxies in this configuration merge with the BCG, it would serve to increase the net angular momentum of the BCG as the angular momenta are aligned. This may explain the fast rotating BCGs observed in our galaxy sample. It would be worthwhile to continue investigating the connection between BCG angular momentum and the angular momentum of other cluster members to test the formation theories proposed by Naab et al. (2014). This would require a large survey of high-mass galaxies using IFU spectroscopy such as MASSIVE, which is currently scheduled to target over 100 early-type galaxies above $10^{11.5} M_{\odot}$.

5.4.2 *Upper Mass Limit to Fast Rotating Galaxies*

Current results suggest that above $10^{11.5} M_{\odot}$, the number of fast rotating galaxies drops off significantly. A targeted search of high dispersion BCGs using IFU spectroscopy would allow us to test whether or not this ceiling continues to hold, or if it is merely an artifact of the small number of massive galaxies with angular momentum measurements. If one were to find examples of fast rotating very massive galaxies, we could search for evidence of recent major mergers despite their already large mass. If however the low ratio of fast rotating galaxies with extremely high masses remains after studying a larger sample, that would be further evidence that mergers are not primarily responsible for the loss of angular momentum as observed in Jimmy et al. (2013)

5.4.3 *Dwarf Galaxy Metallicity Gradients*

Building on the work done with metallicity gradients in brightest cluster galaxies in Oliva-Altamirano et al. (2015), it would be beneficial to continue such studies at the very low-mass end of the spectrum. Within our sample of IFU observed dwarf galaxies, there is evidence to suggest that there are positive metallicity gradients within our sample, however limitations of the depths and spectral range of our observations make it impossible to make strong conclusions. Once again, we must turn to the extremes in order to understand galaxy formation as a whole. By studying the metallicity gradients in extremely low-mass dwarf irregular galaxies, we can better understand the effects of inflows and outflows on the mass-metallicity relation. Gas inflows are likely to result in a buildup of pristine gas on the outer edges of the dwarf irregular galaxies, resulting in a negative metallicity gradient, whereas outflows would have the opposite effect, causing outflowing metals to build up on the outer edges of the galaxy, and resulting in a positive metallicity gradient.

By combining several measurements and several projects together, we are able to achieve a more complete understanding of the validity of the following empirical scaling relations. We use photometric imaging to estimate stellar masses, measure effective radii, and search for evidence of recent mergers and find that BCG angular momentum is seemingly independent of the recent merger history. We utilize IFU spectroscopy to study ISM oxygen abundances using emission line flux ratios and find that pristine inflows of HI-gas were likely to be a primary driver of the mass-metallicity relation. We also use IFU spectroscopy to study the spatial distribution of dust in dwarf irregular galaxies and find that star forming regions are preferentially surrounded by thicker dust clouds. In the future, by obtaining a larger sample of IFU observed Brightest Cluster Galaxies, we could observe their present day kinematics in comparison to theoretical models in order to obtain insight into the fossil record of their assembly histories. Similarly, with deeper and higher resolution observations of dwarf irregular galaxies, we can better understand the inflows and outflows that regulate the mass-metallicity relation. In general, we find that these scaling relations observed are based on fundamental physics that act across an extraordinary range of galaxy mass scales.

REFERENCES

- R. G. Abraham, S. van den Bergh, and P. Nair. A New Approach to Galaxy Morphology. I. Analysis of the Sloan Digital Sky Survey Early Data Release. *ApJ*, 588:218–229, May 2003. doi: 10.1086/373919.
- O. Agertz, R. Teyssier, and B. Moore. Disc formation and the origin of clumpy galaxies at high redshift. *MNRAS*, 397:L64–L68, July 2009. doi: 10.1111/j.1745-3933.2009.00685.x.
- S. Alam, F. D. Albareti, C. Allende Prieto, et al. The Eleventh and Twelfth Data Releases of the Sloan Digital Sky Survey: Final Data from SDSS-III. *ArXiv e-prints*, January 2015.
- L. H. Aller, editor. *Physics of thermal gaseous nebulae*, volume 112 of *Astrophysics and Space Science Library*, 1984.
- B. H. Andrews and P. Martini. The Mass-Metallicity Relation with the Direct Method on Stacked Spectra of SDSS Galaxies. *ApJ*, 765:140, March 2013. doi: 10.1088/0004-637X/765/2/140.
- R. Bacon, G. Adam, A. Baranne, et al. The Integral Field Spectrograph TIGER. In M.-H. Ulrich, editor, *European Southern Observatory Conference and Workshop Proceedings*, volume 30 of *European Southern Observatory Conference and Workshop Proceedings*, page 1185, 1988.
- R. Bacon, Y. Copin, G. Monnet, et al. The SAURON project - I. The panoramic integral-field spectrograph. *MNRAS*, 326:23–35, September 2001. doi: 10.1046/j.1365-8711.2001.04612.x.
- A. J. Battisti, D. Calzetti, and R.-R. Chary. Characterizing Dust Attenuation in Local Star Forming Galaxies: UV and Optical Reddening. *ArXiv e-prints*, January

- 2016.
- T. C. Beers, M. J. Geller, and J. P. Huchra. Galaxy clusters with multiple components. I - The dynamics of Abell 98. *ApJ*, 257:23–32, June 1982. doi: 10.1086/159958.
- E. F. Bell and R. S. de Jong. Stellar Mass-to-Light Ratios and the Tully-Fisher Relation. *ApJ*, 550:212–229, March 2001. doi: 10.1086/319728.
- E. F. Bell, D. H. McIntosh, N. Katz, and M. D. Weinberg. The Optical and Near-Infrared Properties of Galaxies. I. Luminosity and Stellar Mass Functions. *ApJS*, 149:289–312, December 2003. doi: 10.1086/378847.
- R. Bender, D. Burstein, and S. M. Faber. Dynamically hot galaxies. I - Structural properties. *ApJ*, 399:462–477, November 1992. doi: 10.1086/171940.
- D. A. Berg, E. D. Skillman, A. R. Marble, et al. Direct Oxygen Abundances for Low-luminosity LVL Galaxies. *ApJ*, 754:98, August 2012. doi: 10.1088/0004-637X/754/2/98.
- M. Bernardi. Evolution in the structural properties of early-type brightest cluster galaxies at small lookback time and dependence on the environment. *MNRAS*, 395:1491–1506, May 2009. doi: 10.1111/j.1365-2966.2009.14601.x.
- E. Bertin and S. Arnouts. SExtractor: Software for source extraction. *A&AS*, 117: 393–404, June 1996.
- M. Bois, F. Bournaud, E. Emsellem, et al. Formation of slowly rotating early-type galaxies via major mergers: a resolution study. *MNRAS*, 406:2405–2420, August 2010. doi: 10.1111/j.1365-2966.2010.16885.x.
- M. Bois, E. Emsellem, F. Bournaud, et al. The ATLAS^{3D} project - VI. Simulations of binary galaxy mergers and the link with fast rotators, slow rotators and kinematically distinct cores. *MNRAS*, 416:1654–1679, September 2011. doi: 10.1111/j.1365-2966.2011.19113.x.

- A. D. Bolatto, A. K. Leroy, K. Jameson, et al. The State of the Gas and the Relation between Gas and Star Formation at Low Metallicity: The Small Magellanic Cloud. *ApJ*, 741:12, November 2011. doi: 10.1088/0004-637X/741/1/12.
- M. S. Bothwell, R. Maiolino, R. Kennicutt, et al. A fundamental relation between the metallicity, gas content and stellar mass of local galaxies. *MNRAS*, 433:1425–1435, August 2013. doi: 10.1093/mnras/stt817.
- F. Bournaud and B. G. Elmegreen. Unstable Disks at High Redshift: Evidence for Smooth Accretion in Galaxy Formation. *ApJ*, 694:L158–L161, April 2009. doi: 10.1088/0004-637X/694/2/L158.
- F. Bournaud, F. Combes, and C. J. Jog. Unequal-mass galaxy merger remnants: Spiral-like morphology but elliptical-like kinematics. *A&A*, 418:L27–L30, April 2004. doi: 10.1051/0004-6361:20040114.
- F. Bournaud, C. J. Jog, and F. Combes. Multiple minor mergers: formation of elliptical galaxies and constraints for the growth of spiral disks. *A&A*, 476:1179–1190, December 2007. doi: 10.1051/0004-6361:20078010.
- M. Boylan-Kolchin, C.-P. Ma, and E. Quataert. Red mergers and the assembly of massive elliptical galaxies: the fundamental plane and its projections. *MNRAS*, 369:1081–1089, July 2006. doi: 10.1111/j.1365-2966.2006.10379.x.
- J. Brinchmann, S. Charlot, S. D. M. White, et al. The physical properties of star-forming galaxies in the low-redshift Universe. *MNRAS*, 351:1151–1179, July 2004. doi: 10.1111/j.1365-2966.2004.07881.x.
- A. M. Brooks, F. Governato, T. Quinn, C. B. Brook, and J. Wadsley. The Role of Cold Flows in the Assembly of Galaxy Disks. *ApJ*, 694:396–410, March 2009. doi: 10.1088/0004-637X/694/1/396.
- S. Brough, C. A. Collins, D. J. Burke, P. D. Lynam, and R. G. Mann. Environmental dependence of the structure of brightest cluster galaxies. *MNRAS*, 364:1354–1362,

- December 2005. doi: 10.1111/j.1365-2966.2005.09679.x.
- S. Brough, K.-V. Tran, R. G. Sharp, A. von der Linden, and W. J. Couch. Spatial kinematics of Brightest Cluster Galaxies and their close companions from Integral Field Unit spectroscopy. *MNRAS*, 414:L80–L84, June 2011. doi: 10.1111/j.1745-3933.2011.01060.x.
- G. Bruzual and S. Charlot. Stellar population synthesis at the resolution of 2003. *MNRAS*, 344:1000–1028, October 2003. doi: 10.1046/j.1365-8711.2003.06897.x.
- J. J. Bryant, M. S. Owers, A. S. G. Robotham, et al. The SAMI Galaxy Survey: instrument specification and target selection. *MNRAS*, 447:2857–2879, March 2015. doi: 10.1093/mnras/stu2635.
- K. Bundy, M. A. Bershad, D. R. Law, et al. Overview of the SDSS-IV MaNGA Survey: Mapping nearby Galaxies at Apache Point Observatory. *ApJ*, 798:7, January 2015. doi: 10.1088/0004-637X/798/1/7.
- D. Calzetti. Reddening and Star Formation in Starburst Galaxies. *AJ*, 113:162–184, January 1997. doi: 10.1086/118242.
- D. Calzetti, A. L. Kinney, and T. Storchi-Bergmann. Dust extinction of the stellar continua in starburst galaxies: The ultraviolet and optical extinction law. *ApJ*, 429:582–601, July 1994. doi: 10.1086/174346.
- D. Calzetti, L. Armus, R. C. Bohlin, et al. The Dust Content and Opacity of Actively Star-forming Galaxies. *ApJ*, 533:682–695, April 2000. doi: 10.1086/308692.
- M. Cappellari and Y. Copin. Adaptive spatial binning of integral-field spectroscopic data using Voronoi tessellations. *MNRAS*, 342:345–354, June 2003. doi: 10.1046/j.1365-8711.2003.06541.x.
- M. Cappellari and E. Emsellem. Parametric Recovery of Line-of-Sight Velocity Distributions from Absorption-Line Spectra of Galaxies via Penalized Likelihood. *PASP*, 116:138–147, February 2004. doi: 10.1086/381875.

- M. Cappellari, R. Bacon, M. Bureau, et al. The SAURON project - IV. The mass-to-light ratio, the virial mass estimator and the Fundamental Plane of elliptical and lenticular galaxies. *MNRAS*, 366:1126–1150, March 2006. doi: 10.1111/j.1365-2966.2005.09981.x.
- M. Cappellari, E. Emsellem, D. Krajnović, et al. The ATLAS^{3D} project - I. A volume-limited sample of 260 nearby early-type galaxies: science goals and selection criteria. *MNRAS*, 413:813–836, May 2011. doi: 10.1111/j.1365-2966.2010.18174.x.
- M. Cappellari, N. Scott, K. Alatalo, et al. The ATLAS^{3D} project - XV. Benchmark for early-type galaxies scaling relations from 260 dynamical models: mass-to-light ratio, dark matter, Fundamental Plane and Mass Plane. *MNRAS*, 432:1709–1741, July 2013. doi: 10.1093/mnras/stt562.
- N. L. Chapman, L. G. Mundy, S.-P. Lai, and N. J. Evans, II. The Mid-Infrared Extinction Law in the Ophiuchus, Perseus, and Serpens Molecular Clouds. *ApJ*, 690:496–511, January 2009. doi: 10.1088/0004-637X/690/1/496.
- S. Charlot and S. M. Fall. A Simple Model for the Absorption of Starlight by Dust in Galaxies. *ApJ*, 539:718–731, August 2000. doi: 10.1086/309250.
- J. Cohen. *Statistical Power Analysis for the Behavioral Sciences*. L. Erlbaum Associates, 1988. ISBN 9780805802832. URL <https://books.google.com/books?id=T10N21RA09oC>.
- L. L. Cowie and A. J. Barger. An Integrated Picture of Star Formation, Metallicity Evolution, and Galactic Stellar Mass Assembly. *ApJ*, 686:72–116, October 2008. doi: 10.1086/591176.
- T. J. Cox, S. N. Dutta, T. Di Matteo, et al. The Kinematic Structure of Merger Remnants. *ApJ*, 650:791–811, October 2006. doi: 10.1086/507474.
- G. Cresci, F. Mannucci, V. Sommariva, et al. The metallicity properties of zCOSMOS galaxies at $0.2 < z < 0.8$. *MNRAS*, 421:262–269, March 2012. doi: 10.1111/j.1365-

2966.2011.20299.x.

- S. M. Croom, J. S. Lawrence, J. Bland-Hawthorn, et al. The Sydney-AAO Multi-object Integral field spectrograph. *MNRAS*, 421:872–893, March 2012. doi: 10.1111/j.1365-2966.2011.20365.x.
- R. Davé, K. Finlator, B. D. Oppenheimer, et al. The nature of submillimetre galaxies in cosmological hydrodynamic simulations. *MNRAS*, 404:1355–1368, May 2010. doi: 10.1111/j.1365-2966.2010.16395.x.
- R. S. de Jong, S. Kassin, E. F. Bell, and S. Courteau. Properties of Dark Matter Halos in Disk Galaxies. In S. Ryder, D. Pisano, M. Walker, and K. Freeman, editors, *Dark Matter in Galaxies*, volume 220 of *IAU Symposium*, page 281, July 2004.
- G. De Lucia and J. Blaizot. The hierarchical formation of the brightest cluster galaxies. *MNRAS*, 375:2–14, February 2007. doi: 10.1111/j.1365-2966.2006.11287.x.
- G. De Lucia, S. Weinmann, B. M. Poggianti, A. Aragón-Salamanca, and D. Zaritsky. The environmental history of group and cluster galaxies in a Λ cold dark matter universe. *MNRAS*, 423:1277–1292, June 2012. doi: 10.1111/j.1365-2966.2012.20983.x.
- A. Dekel, R. Sari, and D. Ceverino. Formation of Massive Galaxies at High Redshift: Cold Streams, Clumpy Disks, and Compact Spheroids. *ApJ*, 703:785–801, September 2009. doi: 10.1088/0004-637X/703/1/785.
- G. Denicoló, R. Terlevich, and E. Terlevich. New light on the search for low-metallicity galaxies - I. The N2 calibrator. *MNRAS*, 330:69–74, February 2002. doi: 10.1046/j.1365-8711.2002.05041.x.
- L.-B. Desroches, E. Quataert, C.-P. Ma, and A. A. West. Luminosity dependence in the Fundamental Plane projections of elliptical galaxies. *MNRAS*, 377:402–414, May 2007. doi: 10.1111/j.1365-2966.2007.11612.x.

- E. D’Onghia and A. Burkert. Bulgeless Galaxies and Their Angular Momentum Problem. *ApJ*, 612:L13–L16, September 2004. doi: 10.1086/424444.
- A. G. Doroshkevich. Spatial structure of perturbations and origin of galactic rotation in fluctuation theory. *Astrophysics*, 6:320–330, October 1970. doi: 10.1007/BF01001625.
- M. G. Edmunds. General Constraints on the Effect of Gas Flows in the Chemical Evolution of Galaxies. *MNRAS*, 246:678, October 1990.
- D. J. Eisenstein, D. H. Weinberg, E. Agol, et al. SDSS-III: Massive Spectroscopic Surveys of the Distant Universe, the Milky Way, and Extra-Solar Planetary Systems. *AJ*, 142:72, September 2011. doi: 10.1088/0004-6256/142/3/72.
- E. Emsellem, M. Cappellari, D. Krajnović, et al. The SAURON project - IX. A kinematic classification for early-type galaxies. *MNRAS*, 379:401–417, August 2007. doi: 10.1111/j.1365-2966.2007.11752.x.
- E. Emsellem, M. Cappellari, D. Krajnović, et al. The ATLAS^{3D} project - III. A census of the stellar angular momentum within the effective radius of early-type galaxies: unveiling the distribution of fast and slow rotators. *MNRAS*, 414:888–912, June 2011. doi: 10.1111/j.1365-2966.2011.18496.x.
- D. K. Erb, A. E. Shapley, M. Pettini, et al. The Mass-Metallicity Relation at $z \gtrsim 2$. *ApJ*, 644:813–828, June 2006. doi: 10.1086/503623.
- M. Eskew, D. Zaritsky, and S. Meidt. Converting from 3.6 and 4.5 μm Fluxes to Stellar Mass. *AJ*, 143:139, June 2012. doi: 10.1088/0004-6256/143/6/139.
- S. M. Faber, S. Tremaine, E. A. Ajhar, et al. The Centers of Early-Type Galaxies with HST. IV. Central Parameter Relations. *AJ*, 114:1771, November 1997. doi: 10.1086/118606.
- K. Finlator and R. Davé. The origin of the galaxy mass-metallicity relation and implications for galactic outflows. *MNRAS*, 385:2181–2204, April 2008. doi:

- 10.1111/j.1365-2966.2008.12991.x.
- K. M. Flaherty, J. L. Pipher, S. T. Megeath, et al. Infrared Extinction toward Nearby Star-forming Regions. *ApJ*, 663:1069–1082, July 2007. doi: 10.1086/518411.
- W. Freudling, M. Romaniello, D. M. Bramich, et al. Automated data reduction workflows for astronomy. The ESO Reflex environment. *A&A*, 559:A96, November 2013. doi: 10.1051/0004-6361/201322494.
- D. R. Garnett. The Luminosity-Metallicity Relation, Effective Yields, and Metal Loss in Spiral and Irregular Galaxies. *ApJ*, 581:1019–1031, December 2002. doi: 10.1086/344301.
- K. D. Gordon and G. C. Clayton. Starburst-like Dust Extinction in the Small Magellanic Cloud. *ApJ*, 500:816–824, June 1998. doi: 10.1086/305774.
- K. D. Gordon, M. M. Hanson, G. C. Clayton, G. H. Rieke, and K. A. Misselt. The Dusty Starburst Nucleus of M33. *ApJ*, 519:165–176, July 1999. doi: 10.1086/307350.
- A. Grønnow, K. Finlator, and L. Christensen. Merging galaxies produce outliers from the Fundamental Metallicity Relation. *ArXiv e-prints*, June 2015.
- C.-N. Hao, R. C. Kennicutt, B. D. Johnson, et al. Dust-corrected Star Formation Rates of Galaxies. II. Combinations of Ultraviolet and Infrared Tracers. *ApJ*, 741:124, November 2011. doi: 10.1088/0004-637X/741/2/124.
- N. C. Haurberg, J. J. Salzer, J. M. Cannon, and M. V. Marshall. Oxygen Abundance Measurements of SHIELD Galaxies. *ApJ*, 800:121, February 2015. doi: 10.1088/0004-637X/800/2/121.
- M. Hayashi, K. Motohara, K. Shimasaku, et al. Star Formation Rates and Metallicities of K-Selected Star-Forming Galaxies at $z \sim 2$. *ApJ*, 691:140–151, January 2009. doi: 10.1088/0004-637X/691/1/140.
- M. P. Haynes, R. Giovanelli, A. M. Martin, et al. The Arecibo Legacy Fast ALFA

- Survey: The α 40 H I Source Catalog, Its Characteristics and Their Impact on the Derivation of the H I Mass Function. *AJ*, 142:170, November 2011. doi: 10.1088/0004-6256/142/5/170.
- A. M. Hopkins, C. J. Miller, R. C. Nichol, et al. Star Formation Rate Indicators in the Sloan Digital Sky Survey. *ApJ*, 599:971–991, December 2003. doi: 10.1086/379608.
- C. Izzo, N. Kornweibel, D. McKay, et al. Gasgano & ESO VIMOS Pipeline released. *The Messenger*, 117:33–35, September 2004.
- B. L. James, S. Koposov, D. P. Stark, et al. Uncovering blue diffuse dwarf galaxies. *MNRAS*, 448:2687–2703, April 2015. doi: 10.1093/mnras/stv175.
- R. Jesseit, M. Cappellari, T. Naab, E. Emsellem, and A. Burkert. Specific angular momentum of disc merger remnants and the λ_R -parameter. *MNRAS*, 397:1202–1214, August 2009. doi: 10.1111/j.1365-2966.2009.14984.x.
- Jimmy, K.-V. Tran, S. Brough, et al. Angular Momenta, Dynamical Masses, and Mergers of Brightest Cluster Galaxies. *ApJ*, 778:171, December 2013. doi: 10.1088/0004-637X/778/2/171.
- Jimmy, K.-V. Tran, A. Saintonge, et al. The Gas Phase Mass Metallicity Relation for Dwarf Galaxies: Dependence on Star Formation Rate and H I Gas Mass. *ApJ*, 812:98, October 2015. doi: 10.1088/0004-637X/812/2/98.
- A. Jones. Interstellar dust modelling: Interfacing laboratory, theoretical and observational studies (The THEMIS model). *ArXiv e-prints*, November 2015.
- I. D. Karachentsev, V. E. Karachentseva, W. K. Huchtmeier, and D. I. Makarov. A Catalog of Neighboring Galaxies. *AJ*, 127:2031–2068, April 2004. doi: 10.1086/382905.
- G. Kauffmann, T. M. Heckman, C. Tremonti, et al. The host galaxies of active galactic nuclei. *MNRAS*, 346:1055–1077, December 2003. doi: 10.1111/j.1365-2966.2003.07154.x.

- R. C. Kennicutt and N. J. Evans. Star Formation in the Milky Way and Nearby Galaxies. *ARA&A*, 50:531–608, September 2012. doi: 10.1146/annurev-astro-081811-125610.
- L. J. Kewley and S. L. Ellison. Metallicity Calibrations and the Mass-Metallicity Relation for Star-forming Galaxies. *ApJ*, 681:1183–1204, July 2008. doi: 10.1086/587500.
- T. D. Kinman and K. Davidson. Spectroscopic observations of 10 emission-line dwarf galaxies. *ApJ*, 243:127–139, January 1981. doi: 10.1086/158575.
- C. Kobayashi, V. Springel, and S. D. M. White. Simulations of Cosmic Chemical Enrichment. *MNRAS*, 376:1465–1479, April 2007. doi: 10.1111/j.1365-2966.2007.11555.x.
- J. Köppen and M. G. Edmunds. Gas flows and the chemical evolution of galaxies - III. Graphical analysis and secondary elements. *MNRAS*, 306:317–326, June 1999. doi: 10.1046/j.1365-8711.1999.02584.x.
- J. Kormendy and R. Bender. A Proposed Revision of the Hubble Sequence for Elliptical Galaxies. *ApJ*, 464:L119, June 1996. doi: 10.1086/310095.
- K. Kreckel, B. Groves, E. Schinnerer, et al. Mapping Dust through Emission and Absorption in Nearby Galaxies. *ApJ*, 771:62, July 2013. doi: 10.1088/0004-637X/771/1/62.
- M. Kriek and C. Conroy. The Dust Attenuation Law in Distant Galaxies: Evidence for Variation with Spectral Type. *ApJ*, 775:L16, September 2013. doi: 10.1088/2041-8205/775/1/L16.
- M. A. Lara-López, J. Cepa, A. Bongiovanni, et al. A fundamental plane for field star-forming galaxies. *A&A*, 521:L53, October 2010. doi: 10.1051/0004-6361/201014803.
- M. A. Lara-López, Á. R. López-Sánchez, and A. M. Hopkins. On the Three-

- dimensional Structure of the Mass, Metallicity, and Star Formation Rate Space for Star-forming Galaxies. *ApJ*, 764:178, February 2013. doi: 10.1088/0004-637X/764/2/178.
- T. R. Lauer. Cores and the Kinematics of Early-type Galaxies. *ApJ*, 759:64, November 2012. doi: 10.1088/0004-637X/759/1/64.
- T. R. Lauer, S. M. Faber, D. Richstone, et al. The Masses of Nuclear Black Holes in Luminous Elliptical Galaxies and Implications for the Space Density of the Most Massive Black Holes. *ApJ*, 662:808–834, June 2007. doi: 10.1086/518223.
- O. Le Fèvre, M. Saisse, D. Mancini, et al. Commissioning and performances of the VLT-VIMOS instrument. In M. Iye and A. F. M. Moorwood, editors, *Society of Photo-Optical Instrumentation Engineers (SPIE) Conference Series*, volume 4841 of *Society of Photo-Optical Instrumentation Engineers (SPIE) Conference Series*, pages 1670–1681, March 2003. doi: 10.1117/12.460959.
- H. Lee, E. D. Skillman, J. M. Cannon, et al. On Extending the Mass-Metallicity Relation of Galaxies by 2.5 Decades in Stellar Mass. *ApJ*, 647:970–983, August 2006. doi: 10.1086/505573.
- M. D. Lehnert and T. M. Heckman. Ionized Gas in the Halos of Edge-on Starburst Galaxies: Evidence for Supernova-driven Superwinds. *ApJ*, 462:651, May 1996. doi: 10.1086/177180.
- J. Lequeux, M. Peimbert, J. F. Rayo, A. Serrano, and S. Torres-Peimbert. Chemical composition and evolution of irregular and blue compact galaxies. *A&A*, 80:155–166, December 1979.
- C. Lidman, J. Suherli, A. Muzzin, et al. Evidence for significant growth in the stellar mass of brightest cluster galaxies over the past 10 billion years. *MNRAS*, 427:550–568, November 2012. doi: 10.1111/j.1365-2966.2012.21984.x.
- F. S. Liu, S. Mao, Z. G. Deng, X. Y. Xia, and Z. L. Wen. Major dry mergers in

- early-type brightest cluster galaxies. MNRAS, 396:2003–2010, July 2009. doi: 10.1111/j.1365-2966.2009.14907.x.
- X. Liu, A. E. Shapley, A. L. Coil, J. Brinchmann, and C.-P. Ma. Metallicities and Physical Conditions in Star-forming Galaxies at $z \sim 1.0$ -1.5. ApJ, 678:758–779, May 2008. doi: 10.1086/529030.
- J. M. Lotz, P. Jonsson, T. J. Cox, and J. R. Primack. Galaxy merger morphologies and time-scales from simulations of equal-mass gas-rich disc mergers. MNRAS, 391:1137–1162, December 2008. doi: 10.1111/j.1365-2966.2008.14004.x.
- J. M. Lotz, P. Jonsson, T. J. Cox, et al. The Major and Minor Galaxy Merger Rates at $z < 1.5$. ApJ, 742:103, December 2011. doi: 10.1088/0004-637X/742/2/103.
- R. Lupton. Transformations between sdss magnitudes and ubvri. <http://classic.sdss.org/dr4/algorithms/sdssUBVRITransform.html>, 2005. Accessed: 2015-03-17.
- R. H. Lupton, Z. Ivezić, J. E. Gunn, et al. SDSS Imaging Pipelines. In J. A. Tyson and S. Wolff, editors, *Survey and Other Telescope Technologies and Discoveries*, volume 4836 of *Society of Photo-Optical Instrumentation Engineers (SPIE) Conference Series*, pages 350–356, December 2002. doi: 10.1117/12.457307.
- M.-M. Mac Low and A. Ferrara. Starburst-driven Mass Loss from Dwarf Galaxies: Efficiency and Metal Ejection. ApJ, 513:142–155, March 1999. doi: 10.1086/306832.
- R. Maiolino, T. Nagao, A. Grazian, et al. AMAZE. I. The evolution of the mass-metallicity relation at $z > 3$. A&A, 488:463–479, September 2008. doi: 10.1051/0004-6361:200809678.
- F. Mannucci, G. Cresci, R. Maiolino, et al. LSD: Lyman-break galaxies Stellar populations and Dynamics - I. Mass, metallicity and gas at $z \sim 3.1$. MNRAS, 398:1915–1931, October 2009. doi: 10.1111/j.1365-2966.2009.15185.x.

- F. Mannucci, G. Cresci, R. Maiolino, A. Marconi, and A. Gnerucci. A fundamental relation between mass, star formation rate and metallicity in local and high-redshift galaxies. *MNRAS*, 408:2115–2127, November 2010. doi: 10.1111/j.1365-2966.2010.17291.x.
- D. Martizzi, R. Teyssier, and B. Moore. The formation of the brightest cluster galaxies in cosmological simulations: the case for active galactic nucleus feedback. *MNRAS*, 420:2859–2873, March 2012. doi: 10.1111/j.1365-2966.2011.19950.x.
- K. L. Masters, M. P. Haynes, and R. Giovanelli. The Impact of Distance Uncertainties on Local Luminosity and Mass Functions. *ApJ*, 607:L115–L118, June 2004. doi: 10.1086/422100.
- K. L. Masters, C. M. Springob, M. P. Haynes, R. Giovanelli, and J. P. Huchra. Mapping Mass in the Local Universe with SFI++ and 2MASS. In *American Astronomical Society Meeting Abstracts*, volume 37 of *Bulletin of the American Astronomical Society*, page 170.01, December 2005.
- K. B. W. McQuinn, J. M. Cannon, A. E. Dolphin, et al. Characterizing the Star Formation of the Low-Mass SHIELD Galaxies from Hubble Space Telescope Imaging. *ArXiv e-prints*, January 2015.
- L. Michel-Dansac, D. G. Lambas, M. S. Alonso, and P. Tissera. The mass-metallicity relation of interacting galaxies. *MNRAS*, 386:L82–L86, May 2008. doi: 10.1111/j.1745-3933.2008.00466.x.
- C. J. Miller, R. C. Nichol, D. Reichart, et al. The C4 Clustering Algorithm: Clusters of Galaxies in the Sloan Digital Sky Survey. *AJ*, 130:968–1001, September 2005. doi: 10.1086/431357.
- K. A. Misselt, G. C. Clayton, and K. D. Gordon. A Reanalysis of the Ultraviolet Extinction from Interstellar Dust in the Large Magellanic Cloud. *ApJ*, 515:128–139, April 1999. doi: 10.1086/307010.

- A. B. Morales-Luis, E. Pérez-Montero, J. Sánchez Almeida, and C. Muñoz-Tuñón. On the Use of the Index N2 to Derive the Metallicity in Metal-poor Galaxies. *ApJ*, 797:81, December 2014. doi: 10.1088/0004-637X/797/2/81.
- T. Naab, R. Jesseit, and A. Burkert. The influence of gas on the structure of merger remnants. *MNRAS*, 372:839–852, October 2006. doi: 10.1111/j.1365-2966.2006.10902.x.
- T. Naab, L. Oser, E. Emsellem, et al. The ATLAS^{3D} project - XXV. Two-dimensional kinematic analysis of simulated galaxies and the cosmological origin of fast and slow rotators. *MNRAS*, 444:3357–3387, November 2014. doi: 10.1093/mnras/stt1919.
- D. C. Nicholls, M. A. Dopita, R. S. Sutherland, et al. Metal-poor Dwarf Galaxies in the SIGRID Galaxy Sample. I. H II Region Observations and Chemical Abundances. *ApJ*, 786:155, May 2014. doi: 10.1088/0004-637X/786/2/155.
- W. R. Oegerle and J. G. Hoessel. Fundamental parameters of brightest cluster galaxies. *ApJ*, 375:15–24, July 1991. doi: 10.1086/170165.
- P. Oliva-Altamirano, S. Brough, T. Jimmy, Kim-Vy, et al. The accretion histories of brightest cluster galaxies from their stellar population gradients. *MNRAS*, 449: 3347–3359, June 2015. doi: 10.1093/mnras/stv475.
- D. E. Osterbrock. *Astrophysics of gaseous nebulae and active galactic nuclei*. 1989.
- B. E. J. Pagel, M. G. Edmunds, R. A. E. Fosbury, and B. L. Webster. A survey of chemical compositions of H II regions in the Magellanic Clouds. *MNRAS*, 184: 569–592, August 1978. doi: 10.1093/mnras/184.3.569.
- B. Panter, R. Jimenez, A. F. Heavens, and S. Charlot. The cosmic evolution of metallicity from the SDSS fossil record. *MNRAS*, 391:1117–1126, December 2008. doi: 10.1111/j.1365-2966.2008.13981.x.
- P. J. E. Peebles. Origin of the Angular Momentum of Galaxies. *ApJ*, 155:393, February 1969. doi: 10.1086/149876.

- C. Y. Peng, L. C. Ho, C. D. Impey, and H.-W. Rix. Detailed Structural Decomposition of Galaxy Images. *AJ*, 124:266–293, July 2002. doi: 10.1086/340952.
- Y.-j. Peng, S. J. Lilly, K. Kovač, et al. Mass and Environment as Drivers of Galaxy Evolution in SDSS and zCOSMOS and the Origin of the Schechter Function. *ApJ*, 721:193–221, September 2010. doi: 10.1088/0004-637X/721/1/193.
- P. G. Pérez-González, J. Gallego, J. Zamorano, et al. Luminosity and Stellar Mass Functions of Local Star-forming Galaxies. *ApJ*, 587:L27–L30, April 2003. doi: 10.1086/375123.
- E. Pérez-Montero, T. Contini, F. Lamareille, et al. Physical properties of galaxies and their evolution in the VIMOS VLT Deep Survey. II. Extending the mass-metallicity relation to the range $z \sim 0.89$ -1.24. *A&A*, 495:73–81, February 2009. doi: 10.1051/0004-6361:200810558.
- M. Pettini and B. E. J. Pagel. [OIII]/[NII] as an abundance indicator at high redshift. *MNRAS*, 348:L59–L63, March 2004. doi: 10.1111/j.1365-2966.2004.07591.x.
- L. S. Pilyugin, J. M. Vílchez, and T. Contini. Oxygen and nitrogen abundances in nearby galaxies. Correlations between oxygen abundance and macroscopic properties. *A&A*, 425:849–869, October 2004. doi: 10.1051/0004-6361:20034522.
- N. A. Reddy, M. Kriek, A. E. Shapley, et al. The MOSDEF Survey: Measurements of Balmer Decrements and the Dust Attenuation Curve at Redshifts $z \sim 1.4$ -2.6. *ApJ*, 806:259, June 2015. doi: 10.1088/0004-637X/806/2/259.
- S. N. Richards, A. L. Schaefer, Á. R. López-Sánchez, et al. The SAMI Galaxy Survey: the discovery of a luminous, low-metallicity H II complex in the dwarf galaxy GAMA J141103.98-003242.3. *MNRAS*, 445:1104–1113, December 2014. doi: 10.1093/mnras/stu1820.
- B. Robertson, T. J. Cox, L. Hernquist, et al. The Fundamental Scaling Relations of Elliptical Galaxies. *ApJ*, 641:21–40, April 2006. doi: 10.1086/500360.

- N. Roche, A. Humphrey, J. M. Gomes, et al. CALIFA spectroscopy of the interacting galaxy NGC 5394 (Arp 84): starbursts, enhanced [N II]6584 and signs of outflows and shocks. *MNRAS*, 453:2349–2363, November 2015. doi: 10.1093/mnras/stv1669.
- M. Rodrigues, F. Hammer, H. Flores, et al. IMAGES IV: strong evolution of the oxygen abundance in gaseous phases of intermediate mass galaxies from $z \sim 0.8$. *A&A*, 492:371–388, December 2008. doi: 10.1051/0004-6361/200810435.
- D. Rosa-González, E. Terlevich, and R. Terlevich. An empirical calibration of star formation rate estimators. *MNRAS*, 332:283–295, May 2002. doi: 10.1046/j.1365-8711.2002.05285.x.
- A. Saintonge. *Properties of low mass dwarf galaxies in the ALFALFA survey*. PhD thesis, Cornell University, 2007.
- S. Salim, J. C. Lee, C. Ly, et al. A Critical Look at the Mass-Metallicity-Star Formation Rate Relation in the Local Universe. I. An Improved Analysis Framework and Confounding Systematics. *ApJ*, 797:126, December 2014. doi: 10.1088/0004-637X/797/2/126.
- B. Salmon, C. Papovich, J. Long, et al. Breaking the Curve with CANDELS: A Bayesian Approach to Reveal the Non-Universality of the Dust-Attenuation Law at High Redshift. *ArXiv e-prints*, December 2015.
- J. J. Salzer, J. C. Lee, J. Melbourne, et al. Metal Abundances of KISS Galaxies. IV. Galaxian Luminosity-Metallicity Relations in the Optical and Near-Infrared. *ApJ*, 624:661–679, May 2005. doi: 10.1086/429386.
- S. F. Sánchez. IFUs surveys, a panoramic view of galaxy evolution. In B. L. Ziegler, F. Combes, H. Dannerbauer, and M. Verdugo, editors, *IAU Symposium*, volume 309 of *IAU Symposium*, pages 85–92, February 2015. doi: 10.1017/S1743921314009375.

- S. F. Sánchez, R. C. Kennicutt, A. Gil de Paz, et al. CALIFA, the Calar Alto Legacy Integral Field Area survey. I. Survey presentation. *A&A*, 538:A8, February 2012. doi: 10.1051/0004-6361/201117353.
- P. Sánchez-Blázquez, R. F. Peletier, J. Jiménez-Vicente, et al. Medium-resolution Isaac Newton Telescope library of empirical spectra. *MNRAS*, 371:703–718, September 2006. doi: 10.1111/j.1365-2966.2006.10699.x.
- M. Sarzi, J. Falcón-Barroso, R. L. Davies, et al. The SAURON project - V. Integral-field emission-line kinematics of 48 elliptical and lenticular galaxies. *MNRAS*, 366: 1151–1200, March 2006. doi: 10.1111/j.1365-2966.2005.09839.x.
- S. Savaglio, K. Glazebrook, D. Le Borgne, et al. The Gemini Deep Deep Survey. VII. The Redshift Evolution of the Mass-Metallicity Relation. *ApJ*, 635:260–279, December 2005. doi: 10.1086/497331.
- C. Scannapieco, P. B. Tissera, S. D. M. White, and V. Springel. Effects of supernova feedback on the formation of galaxy discs. *MNRAS*, 389:1137–1149, September 2008. doi: 10.1111/j.1365-2966.2008.13678.x.
- N. Scoville, A. Faisst, P. Capak, et al. Dust Attenuation in High Redshift Galaxies: "Diamonds in the Sky". *ApJ*, 800:108, February 2015. doi: 10.1088/0004-637X/800/2/108.
- Y. L. Shirley, T. L. Huard, K. M. Pontoppidan, et al. Observational Constraints on Submillimeter Dust Opacity. *ApJ*, 728:143, February 2011. doi: 10.1088/0004-637X/728/2/143.
- E. D. Skillman, R. C. Kennicutt, and P. W. Hodge. Oxygen abundances in nearby dwarf irregular galaxies. *ApJ*, 347:875–882, December 1989. doi: 10.1086/168178.
- L. J. Smith, R. P. F. Norris, and P. A. Crowther. Realistic ionizing fluxes for young stellar populations from 0.05 to $2 Z_{\text{solar}}$. *MNRAS*, 337:1309–1328, December 2002. doi: 10.1046/j.1365-8711.2002.06042.x.

- L. S. Sparke and J. S. Gallagher, III. *Galaxies in the universe : an introduction*. August 2000.
- E. Spitoni, S. Recchi, and F. Matteucci. Galactic fountains and their connection with high and intermediate velocity clouds. *A&A*, 484:743–753, June 2008. doi: 10.1051/0004-6361:200809403.
- C. M. Springob, K. L. Masters, M. P. Haynes, R. Giovanelli, and C. Marinoni. SFI++. II. A New I-Band Tully-Fisher Catalog, Derivation of Peculiar Velocities, and Data Set Properties. *ApJS*, 172:599–614, October 2007. doi: 10.1086/519527.
- J. P. Stott, C. A. Collins, C. Burke, V. Hamilton-Morris, and G. P. Smith. Little change in the sizes of the most massive galaxies since $z = 1$. *MNRAS*, 414:445–457, June 2011. doi: 10.1111/j.1365-2966.2011.18404.x.
- L. J. Tacconi, R. Genzel, R. Neri, et al. High molecular gas fractions in normal massive star-forming galaxies in the young Universe. *Nature*, 463:781–784, February 2010. doi: 10.1038/nature08773.
- J. C. Tan. Comparison of Low-Mass and High-Mass Star Formation. *ArXiv e-prints*, October 2015.
- K.-V. H. Tran, J. Moustakas, A. H. Gonzalez, et al. The Late Stellar Assembly of Massive Cluster Galaxies via Major Merging. *ApJ*, 683:L17–L20, August 2008. doi: 10.1086/591422.
- C. A. Tremonti, T. M. Heckman, G. Kauffmann, et al. The Origin of the Mass-Metallicity Relation: Insights from 53,000 Star-forming Galaxies in the Sloan Digital Sky Survey. *ApJ*, 613:898–913, October 2004. doi: 10.1086/423264.
- F. C. van den Bosch, T. Abel, R. A. C. Croft, L. Hernquist, and S. D. M. White. The Angular Momentum of Gas in Protogalaxies. I. Implications for the Formation of Disk Galaxies. *ApJ*, 576:21–35, September 2002. doi: 10.1086/341619.
- V. Vikram, Y. Wadadekar, A. K. Kembhavi, and G. V. Vijayagovindan. PYMORPH:

- automated galaxy structural parameter estimation using PYTHON. *MNRAS*, 409: 1379–1392, December 2010. doi: 10.1111/j.1365-2966.2010.17426.x.
- M. Vitvitska, A. A. Klypin, A. V. Kravtsov, et al. The Origin of Angular Momentum in Dark Matter Halos. *ApJ*, 581:799–809, December 2002. doi: 10.1086/344361.
- A. von der Linden, P. N. Best, G. Kauffmann, and S. D. M. White. How special are brightest group and cluster galaxies? *MNRAS*, 379:867–893, August 2007. doi: 10.1111/j.1365-2966.2007.11940.x.
- J. Walcher, B. Groves, T. Budavári, and D. Dale. Fitting the integrated spectral energy distributions of galaxies. *Ap&SS*, 331:1–52, January 2011. doi: 10.1007/s10509-010-0458-z.
- F. Walter, J. M. Cannon, H. Roussel, et al. Dust and Atomic Gas in Dwarf Irregular Galaxies of the M81 Group: The SINGS and THINGS View. *ApJ*, 661:102–114, May 2007. doi: 10.1086/514807.
- A. A. West, D. A. Garcia-Appadoo, J. J. Dalcanton, et al. H I-Selected Galaxies in the Sloan Digital Sky Survey. I. Optical Data. *AJ*, 139:315–328, February 2010. doi: 10.1088/0004-6256/139/2/315.
- S. D. M. White. Angular momentum growth in protogalaxies. *ApJ*, 286:38–41, November 1984. doi: 10.1086/162573.
- D. O. S. Wood and E. Churchwell. The morphologies and physical properties of ultracompact H II regions. *ApJS*, 69:831–895, April 1989. doi: 10.1086/191329.
- D. G. York, J. Adelman, J. E. Anderson, Jr., et al. The Sloan Digital Sky Survey: Technical Summary. *AJ*, 120:1579–1587, September 2000. doi: 10.1086/301513.
- D. Zaritsky, R. C. Kennicutt, Jr., and J. P. Huchra. H II regions and the abundance properties of spiral galaxies. *ApJ*, 420:87–109, January 1994. doi: 10.1086/173544.
- G. R. Zeimann, R. Ciardullo, C. Gronwall, et al. The Dust Attenuation Curve versus Stellar Mass for Emission Line Galaxies at $z \sim 2$. *ApJ*, 814:162, December 2015.

doi: 10.1088/0004-637X/814/2/162.

APPENDIX A

ABILITY TO RECOVER METALLICITY

Due to the spectral resolution and instrumental dispersion of the VIMOS LR Blue grism, some emission lines are severely blended together, as can be seen in Figure 4.1. Our science results depend on the [NII] and H α emission lines which are separated by ~ 20 Å. To test our ability to recover the emission line fluxes of the blended [NII] and H α emission lines within our spectra, we create a simulated galaxy with known emission line ratios and test our ability to recover them using our Python-based Gaussian fitting routines.

To create the simulated galaxy, we first take a pipeline reduced data cube from one of the galaxies in our sample that was too faint to be detected by the IFU spectrograph (AGC220261) and find a region of the field of view which contains only sky with little instrumental artifacts to interfere. We also check to ensure that none of the galaxy that was originally intended to be observed is located near this region. We then generate a simulated galaxy and place it within this region. This simulated galaxy is then run through our full data reduction pipeline to measure the recovered emission line ratios. This process is repeated several times to test for metallicity dependence of our ability to recover emission line ratios.

To ensure that we generate physically realistic simulated galaxies, we draw our input emission line ratios from the Berg et al. (2012) survey of low-luminosity galaxies. For every galaxy in the Berg et al. (2012) sample, we use the long slit measured emission line ratios to create a simulated galaxy with the same emission line ratios. We scale the brightest central spaxel in the simulated galaxy to have an H β emission line flux of 3.0×10^{-16} erg cm $^{-2}$ s $^{-1}$ Å $^{-1}$, which corresponds to the average H β

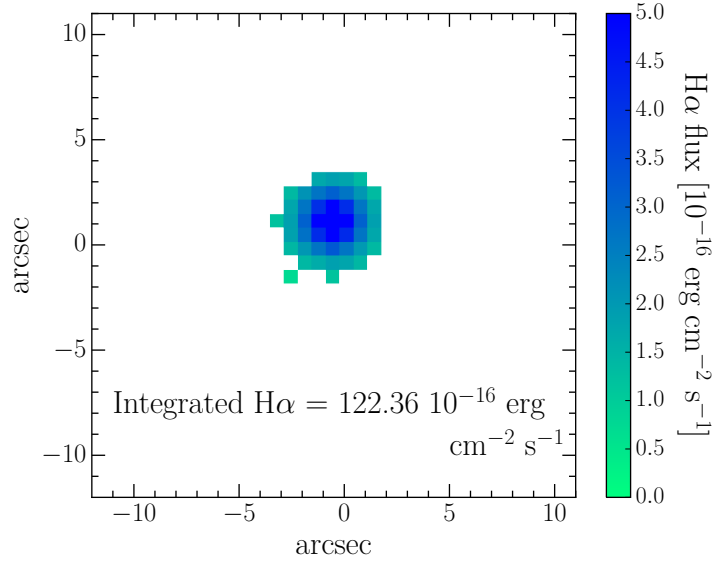


Figure A.1: Example $\text{H}\alpha$ emission of a Simulated Galaxy. $\text{H}\alpha$ emission observed in a simulated galaxy as recovered by our Python-based Gaussian fitting routines. Also shown is the recovered $\text{H}\alpha$ flux after integrating the spectra of each spaxel shown.

flux in the brightest spaxel of each galaxy in the dwarf IFU sample. The flux of the simulated galaxy decreases exponentially with radius. Each emission line is given a dispersion equal to the average instrumental dispersion of 7.5 \AA .

An example of the $\text{H}\alpha$ emission map for one of our simulated galaxies can be seen in Figure A.1. Emission lines for a sample fiber of our simulated galaxy can be seen in Figure A.2 which can be compared to Figure 4.1 visually to confirm that the simulated galaxies being created are physically realistic.

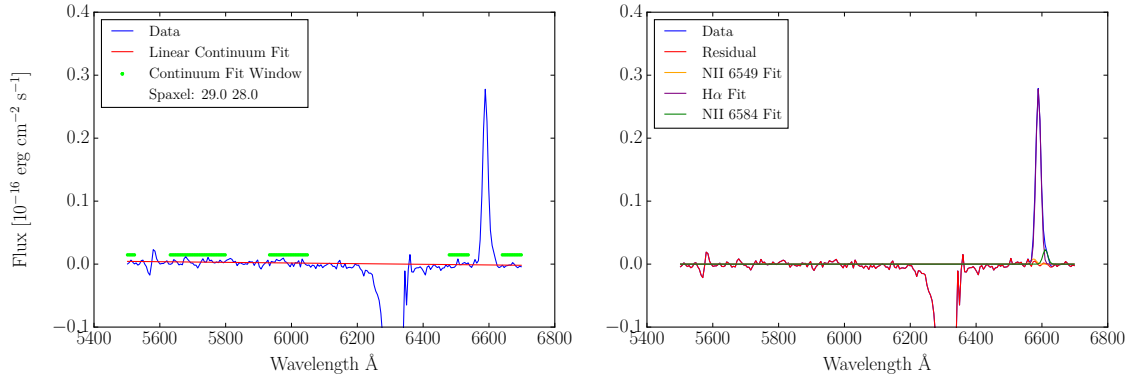


Figure A.2: Details of Python Based Gaussian Fitting Routines. Left: Input simulated spaxel for our simulated galaxy. Blue curves indicate the simulated spectral data, red lines indicates the linear continuum fit done in the first stage of our Python-based Gaussian fitting routines, and green points indicate the fitting window that was used to determine the linear fit. The fitting window excludes residuals from skylines and the large internal reflection feature at $\sim 6300\text{\AA}$. Right: Three Gaussian fits of the H α and [NII] emission lines as found by our routines. The routines are able to successfully resolve the 3 blended emission lines.

APPENDIX B

COMPARISON BETWEEN N2 AND O3N2 BASED CALIBRATIONS

We simulate every galaxy in the Berg et al. (2012) sample using the method outlined in Appendix A to test both our ability to recover input strong-line emission ratios, and to compare our recovered metallicity estimations to direct metallicity measurements. The top row of Figure B.1 shows the comparison between input and recovered metallicities in each of the three calibrations: PP04 O3N2, PP04 N2, and D02 N2. We find that our Python-based Gaussian fitting routines are able to successfully recover line fluxes within 1 standard deviation down to the lowest metallicity simulated. The larger error bars in N2 line ratios of the low-metallicity simulated galaxies measured are due to the amplitude of the [NII] lines being comparable to the noise of the spectra.

The bottom row of Figure B.1 shows the gas-phase metallicity measured directly along with the recovered gas-phase metallicity. Although the O3N2 based estimation has smaller error bars due to the increased information from the [OIII] and $H\beta$ emission line information, it is less accurate than the N2 based estimations due to the saturation of the [OIII]/ $H\beta$ ratio known to occur in O3N2 based oxygen abundance estimations at low gas-phase metallicity (Pettini and Pagel, 2004).

We find based on the bottom row of Figure B.1 that D02 N2 oxygen abundance estimations are better correlated with direct metallicity measurements than PP04 O3N2 estimations for low-metallicity galaxies such as those presented in this study. We find that PP04 O3N2 provides more precise, but less accurate observations, whereas D02 N2 provides more accurate, but less precise observations for the lowest metallicity galaxies.

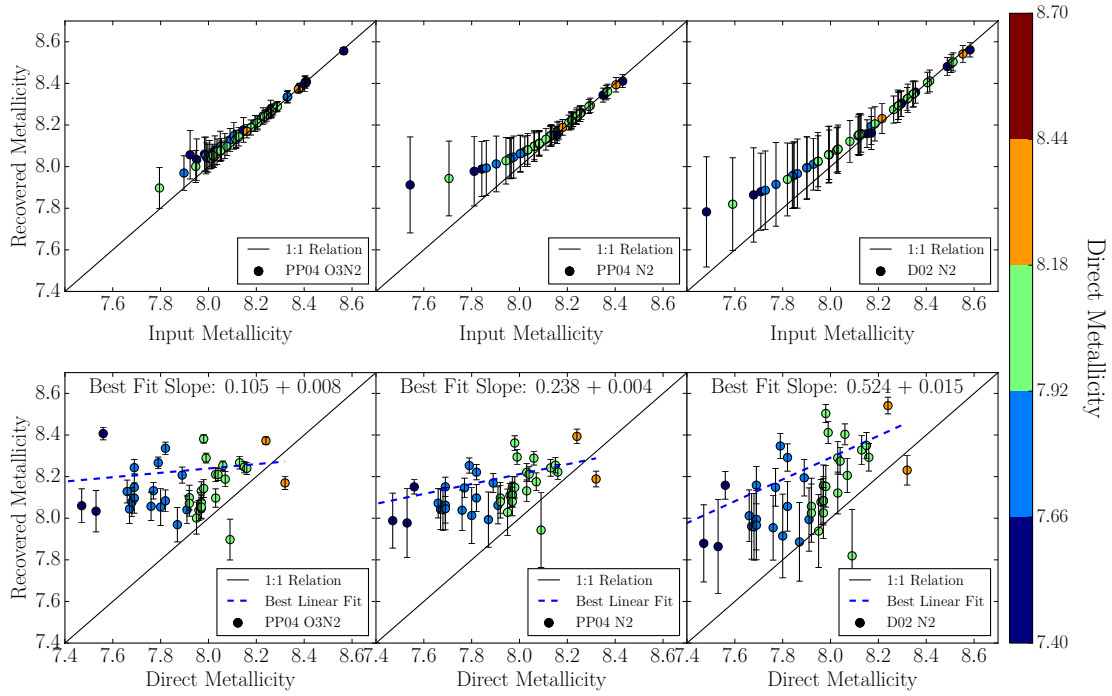


Figure B.1: Ability to Recover Metallicities. Showing the ability of our Python-based Gaussian fitting routines to recover metallicities in various systems after creating a simulated galaxy. In the top row, the x-axis shows the input gas-phase metallicity based on the input line flux ratios, and the y-axis shows the result measured using our routines. In the bottom row, the x-axis shows the direct metallicity that was used to create the simulated galaxy, and the y-axis shows the gas-phase metallicity measured using our routines. We find that the D02 oxygen abundance calibration is more accurate than the PP04 based systems, however PP04 O3N2 is more precise than the D02 based systems.

For the sake of completeness, we have reproduced all of the figures from the main text which contain oxygen abundance estimations using the O3N2 based oxygen abundance estimation from Pettini and Pagel (2004):

$$12 + \log(\text{O}/\text{H}) = 8.73 - 0.32 \times \text{O3N2} \quad (\text{B.1})$$

where

$$\text{O3N2} = \log \left\{ \frac{[\text{OIII}]\lambda 5007 / \text{H}\beta}{[\text{NII}]\lambda 6583 / \text{H}\alpha} \right\}. \quad (\text{B.2})$$

We find that in general, the trends observed in the paper and the conclusions of the paper continue to hold, especially on the high-metallicity end, however the oxygen abundance floor of the O3N2 based estimations cause the conclusions to be less solid than as observed in the N2 based results of the main text.

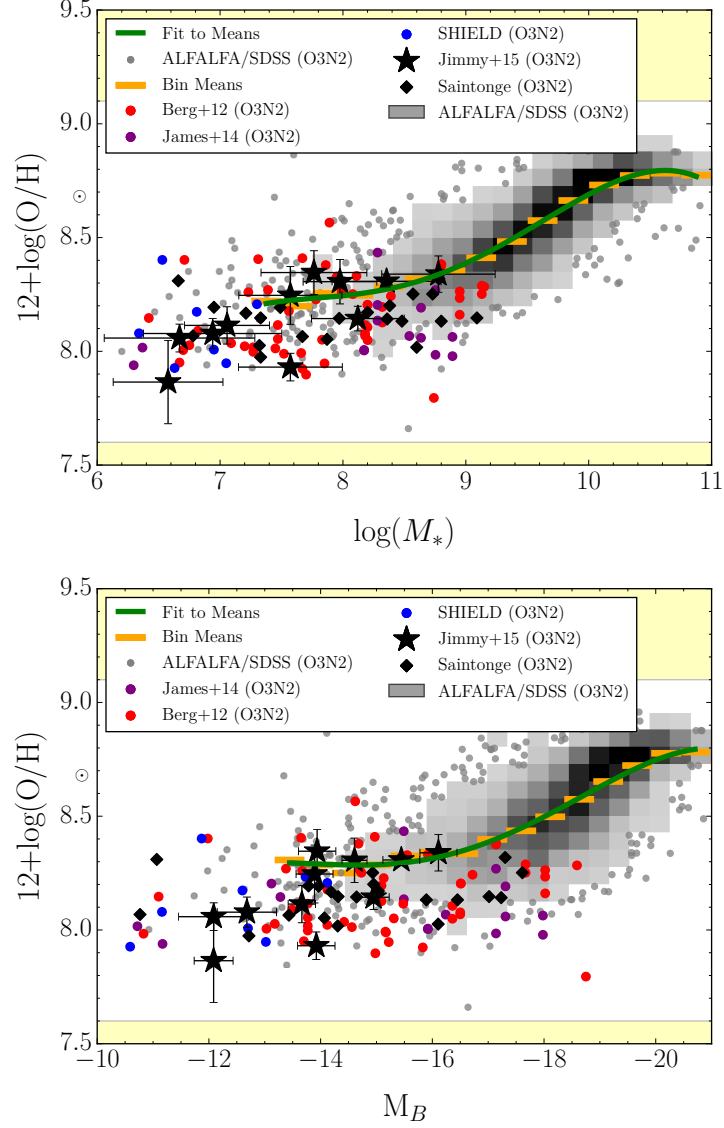


Figure B.2: Figure 3.5 Using the PP04 O3N2 Oxygen Abundance Calibration. Top: The mass-metallicity relation for the IFU observed dwarf galaxy sample, along with several low stellar mass galaxy observations and the ALFALFA/SDSS sample. Bottom: The luminosity-metallicity relation for the IFU observed dwarf galaxy sample, along with several low stellar mass galaxy observations and the ALFALFA/SDSS sample. The scatter in both the MZR and the LZR fit around the bin means is 0.05 dex. For reference we plot a sun symbol at solar metallicity, showing that all of the IFU observed dwarf galaxy oxygen abundances are below solar. The yellow regions indicate the calibration limits of the D02 N2 oxygen abundance estimation. We have used the published emission line fluxes from other authors to estimate the oxygen abundance in the same PP04 O3N2 system. The mass-metallicity relation appears to flatten out in the low stellar-mass/low luminosity regime.

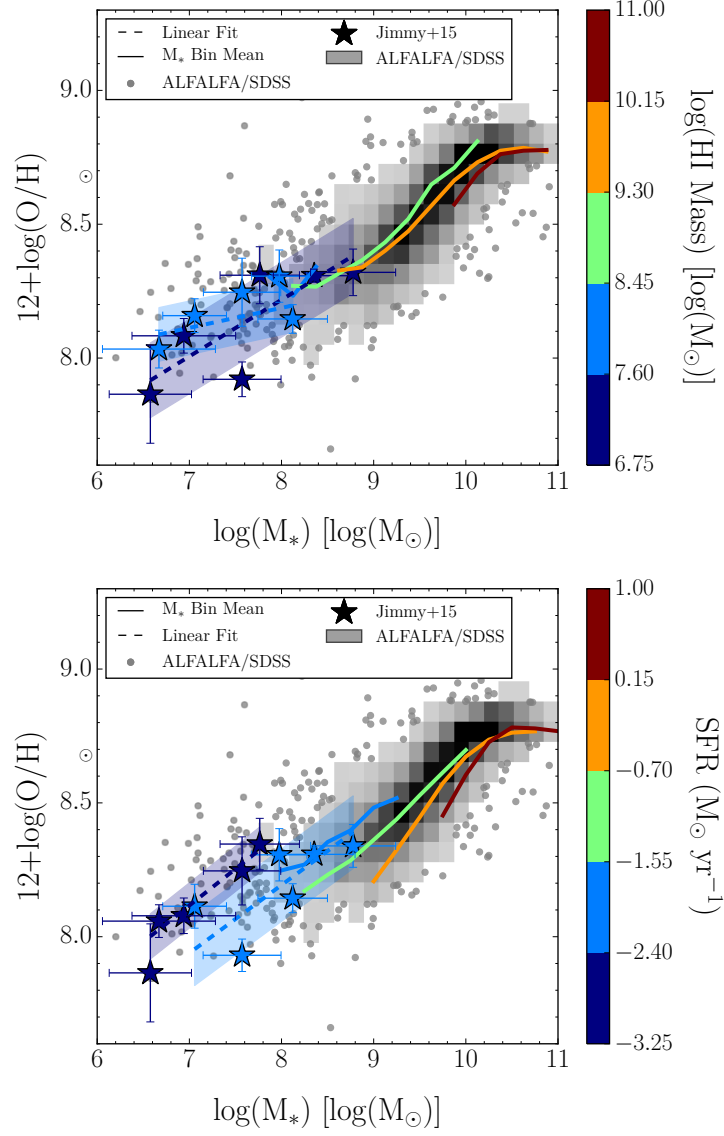


Figure B.3: Figure 3.6 Using the PP04 O3N2 Oxygen Abundance Calibration. The mass-metallicity relation as seen in Figure B.2 color-coded by HI mass (top) and SFR (bottom). The stars indicate individual observations within our IFU observed sample of dwarf galaxies. The dashed lines indicate linear least squares fits to these points, and the shaded regions indicate the 1σ standard deviations to these fits. The solid curves indicate the mean values of the ALFALFA/SDSS sample, separated into HI mass bins. Shown in the background are the ALFALFA/SDSS points which are binned to produce the color-coded means. We find little overlap between the SFR bins (bottom).

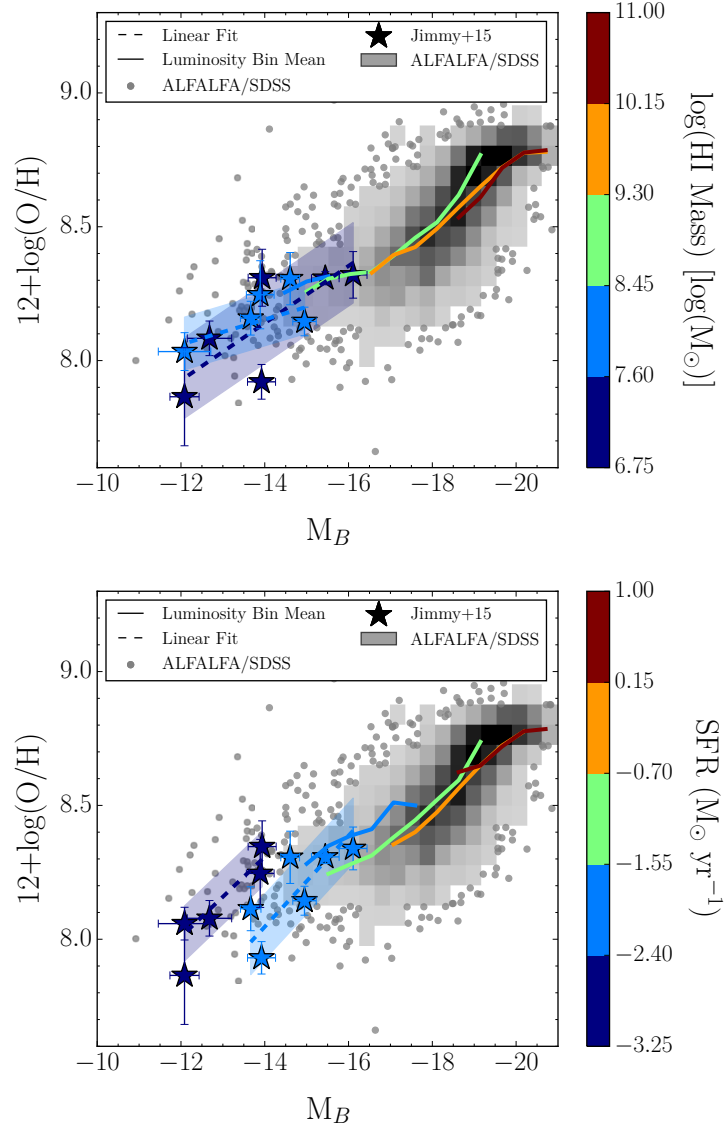


Figure B.4: Figure 3.7 Using the PP04 O3N2 Oxygen Abundance Calibration. The luminosity-metallicity relation as seen in Figure B.2 color-coded by HI mass (top) and SFR (bottom). The stars indicate individual observations within our IFU observed sample of dwarf galaxies. The solid curves indicate the mean values of the ALFALFA/SDSS sample, separated into HI mass bins. Shown in the background are the ALFALFA/SDSS points which are binned to produce the color-coded means. We find little overlap between the SFR bins (bottom).

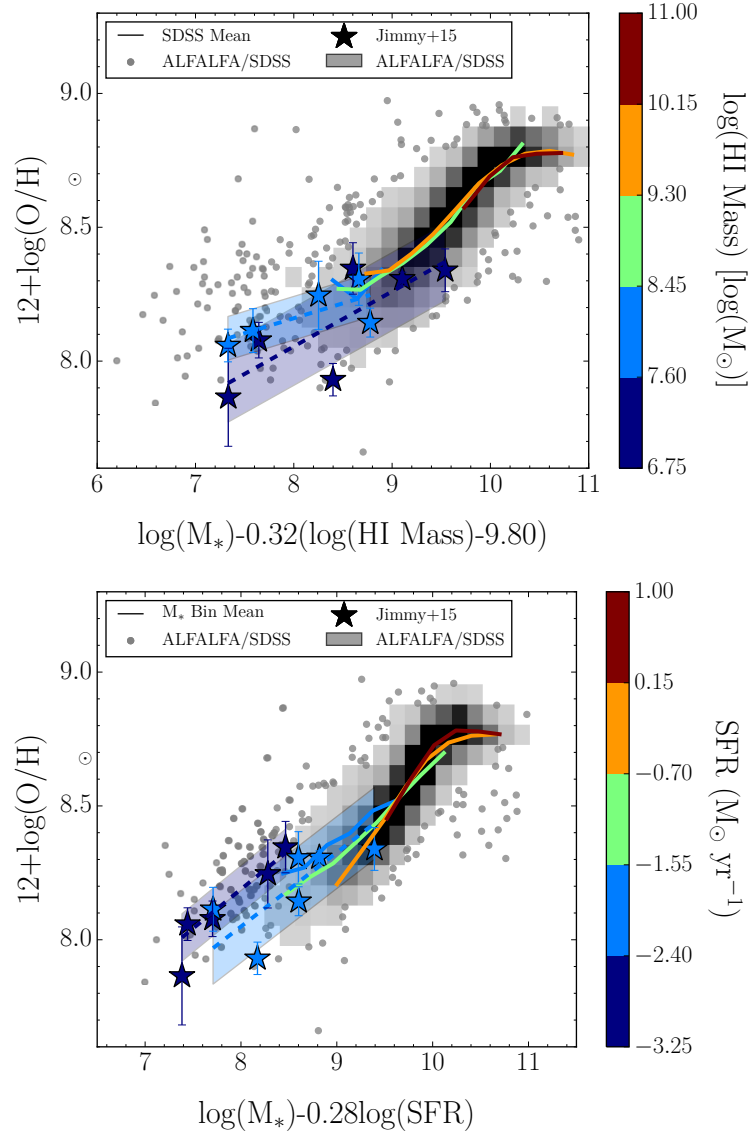


Figure B.5: Figure 3.9 Using the PP04 O3N2 Oxygen Abundance Calibration. FMR_{HI} (top) and FMR_{SFR} (bottom) as calculated using the α and β values found to minimize scatter (Figure 3.8). We find that the FMR_{HI} relation is consistent down to the lowest HI-mass bin, whereas the lowest SFR bin in the FMR_{SFR} is offset 1σ above the ALFALFA/SDSS derived FMR_{SFR} .

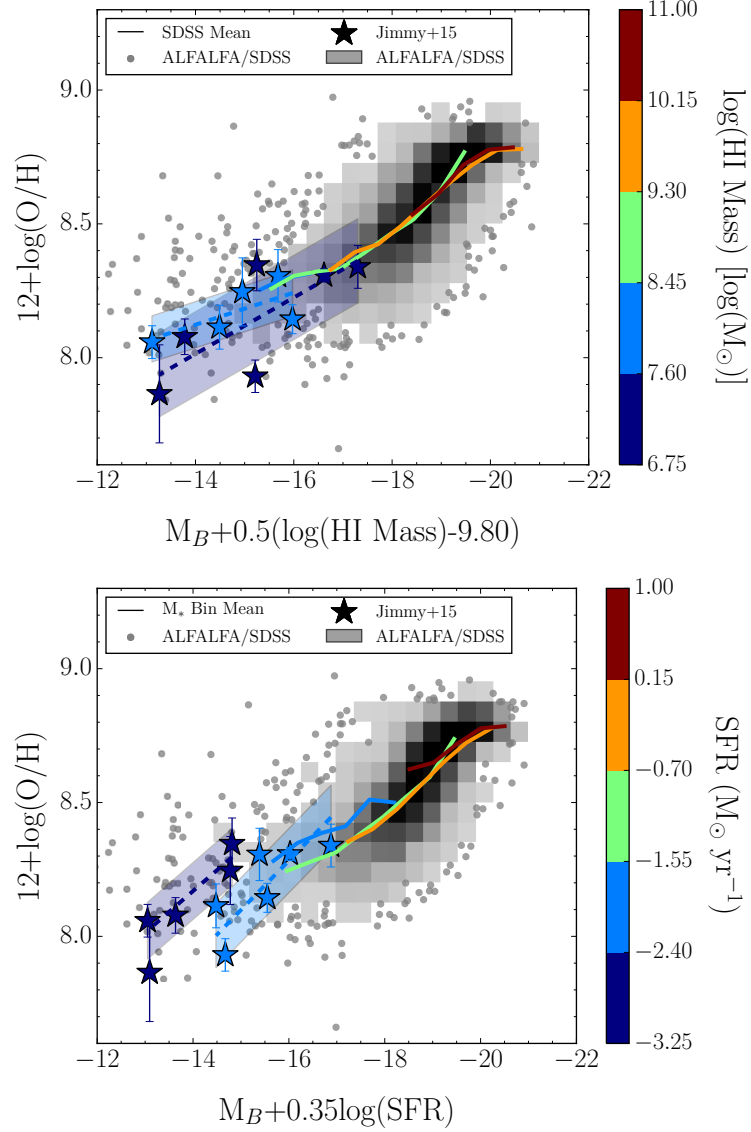


Figure B.6: Figure 3.11 Using the PP04 O3N2 Oxygen Abundance Calibration. FML_{HI} (top) and FML_{SFR} (bottom) as calculated using the ζ and γ values found to minimize scatter (Figure 3.10). We find that the FML_{HI} relation is consistent down to the lowest HI-mass bin, where as the lowest SFR bin in the FML_{SFR} is offset 1σ above the FML_{SFR} .

APPENDIX C

SFR AND HI MASS MEAN BINS

To correspond to the linear fits, we provide a set of tables showing the mean metallicity values in each one of the SFR and HI mass binned data for both the MZR and LZR. These values could be used to reproduce the solid curves of the SFR or HI-mass bins in Figures 3.6 & 3.7.

Table C.1: ALFALFA/SDSS FMR Binned Mean Metallicity Values

Stellar Mass Bin Range	12+log(O/H) Unbinned SFR	12+log(O/H) SFR -2.6 to -1.7	12+log(O/H) SFR -1.7 to -0.8	12+log(O/H) SFR -0.8 to 0.1	12+log(O/H) SFR 0.1 to 1.0
7.75 to 8.0	8.22	8.22	-	-	-
8.0 to 8.25	8.23	8.25	8.17	-	-
8.25 to 8.5	8.29	8.36	8.26	-	-
8.5 to 8.75	8.35	8.41	8.33	-	-
8.75 to 9.0	8.42	8.52	8.43	8.28	-
9.0 to 9.25	8.5	-	8.53	8.42	-
9.25 to 9.5	8.58	-	8.62	8.55	-
9.5 to 9.75	8.67	-	8.70	8.67	8.58
9.75 to 10.0	8.74	-	8.79	8.74	8.70
10.0 to 10.25	8.78	-	-	8.79	8.77
10.25 to 10.5	8.81	-	-	8.83	8.80
10.5 to 10.75	8.83	-	-	8.84	8.82
10.75 to 11.0	8.82	-	-	-	8.82

Stellar Mass Bin Range	12+log(O/H) Unbinned HI Mass	12+log(O/H) HI Mass 7.6 to 8.45	12+log(O/H) HI Mass 8.45 to 9.3	12+log(O/H) HI Mass 9.3 to 10.15	12+log(O/H) HI Mass 10.15 to 11.0
7.75 to 8.0	8.22	8.30	-	-	-
8.0 to 8.25	8.23	8.22	8.25	-	-
8.25 to 8.5	8.29	8.37	8.27	-	-
8.5 to 8.75	8.35	-	8.35	8.35	-
8.75 to 9.0	8.42	-	8.44	8.40	-
9.0 to 9.25	8.5	-	8.53	8.48	-
9.25 to 9.5	8.58	-	8.63	8.57	-
9.5 to 9.75	8.67	-	8.72	8.67	-
9.75 to 10.0	8.74	-	8.78	8.74	8.67
10.0 to 10.25	8.78	-	8.78	8.78	8.75
10.25 to 10.5	8.81	-	-	8.81	8.80
10.5 to 10.75	8.83	-	-	8.83	8.82
10.75 to 11.0	8.82	-	-	8.82	8.82

Binned means used to produce the solid lines observed in Figure 3.6.

Table C.2: ALFALFA/SDSS FML Binned Mean Metallicity Values

Luminosity Bin Range	12+log(O/H) Unbinned SFR	12+log(O/H) SFR -2.6 to -1.7	12+log(O/H) SFR -1.7 to -0.8	12+log(O/H) SFR -0.8 to 0.1	12+log(O/H) SFR 0.1 to 1.0
-15.26 to -14.74	8.29	8.27	-	-	-
-15.78 to -15.26	8.33	8.34	8.28	-	-
-16.3 to -15.78	8.37	8.40	8.33	-	-
-16.81 to -16.3	8.38	8.43	8.36	-	-
-17.33 to -16.81	8.47	8.56	8.46	8.43	-
-17.85 to -17.33	8.52	8.52	8.53	8.50	-
-18.37 to -17.85	8.59	-	8.61	8.57	-
-18.89 to -18.37	8.66	-	8.69	8.65	8.71
-19.41 to -18.89	8.73	-	8.81	8.73	8.72
-19.93 to -19.41	8.77	-	-	8.78	8.77
-20.44 to -19.93	8.81	-	-	8.82	8.80
-20.96 to -20.44	8.81	-	-	-	8.80

Luminosity Bin Range	12+log(O/H) Unbinned HI Mass	12+log(O/H) HI Mass 7.6 to 8.45	12+log(O/H) HI Mass 8.45 to 9.3	12+log(O/H) HI Mass 9.3 to 10.15	12+log(O/H) HI Mass 10.15 to 11.0
-14.74 to -14.22	8.24	8.24	-	-	-
-15.26 to -14.74	8.29	8.30	8.20	-	-
-15.78 to -15.26	8.33	8.32	8.31	-	-
-16.3 to -15.78	8.37	-	8.35	-	-
-16.81 to -16.3	8.38	-	8.37	8.37	-
-17.33 to -16.81	8.47	-	8.48	8.46	-
-17.85 to -17.33	8.52	-	8.56	8.51	-
-18.37 to -17.85	8.59	-	8.61	8.59	-
-18.89 to -18.37	8.66	-	8.70	8.66	8.64
-19.41 to -18.89	8.73	-	8.79	8.73	8.72
-19.93 to -19.41	8.77	-	-	8.77	8.77
-20.44 to -19.93	8.81	-	-	8.80	8.82
-20.96 to -20.44	8.81	-	-	8.81	8.80

Binned means used to produce the solid lines observed in Figure 3.7.

APPENDIX D

TABLE OF FLUX VALUES

We provide our emission line measurements for the integrated spectra from each galaxy's IFU observations so that others may use them for their own analysis.

Table D.1: Observed Emission Line Fluxes of Dwarf Galaxies

Galaxy AGC#	H β 4861 Å	[OIII] 5007 Å	H α 6563 Å	[NII] 6583 Å
AGC191702	82.1 \pm 11.3	247.4 \pm 25.5	249.6 \pm 31.8	6.0 \pm 2.3
AGC202218	56.3 \pm 8.3	223.4 \pm 28.0	223.7 \pm 31.1	13.1 \pm 4.0
AGC212838	47.0 \pm 6.3	174.3 \pm 21.3	151.1 \pm 20.5	5.2 \pm 2.2
AGC220755	10.7 \pm 3.7	23.4 \pm 7.7	43.0 \pm 13.9	5.9 \pm 2.3
AGC220837	12.3 \pm 3.3	35.1 \pm 9.8	65.1 \pm 15.9	11.2 \pm 3.9
AGC220860	60.7 \pm 5.1	321.2 \pm 23.3	212.2 \pm 14.9	3.6 \pm 1.5
AGC221000	125.1 \pm 7.2	230.6 \pm 12.5	492.5 \pm 29.3	43.5 \pm 6.3
AGC221004	38.1 \pm 13.5	69.9 \pm 23.4	126.2 \pm 43.0	11.0 \pm 4.1
AGC225852	21.8 \pm 9.4	48.8 \pm 19.1	66.5 \pm 28.3	4.6 \pm 2.6
AGC225882	52.4 \pm 7.5	111.2 \pm 12.8	142.0 \pm 21.4	3.6 \pm 1.9
AGC227897	14.3 \pm 0.6	74.2 \pm 1.3	41.7 \pm 1.0	0.4 \pm 0.6

All line fluxes measurements are in units of 10^{-16} erg cm $^{-2}$ s $^{-1}$ Å $^{-1}$. These are the line fluxes used to calculate oxygen abundance estimations throughout this work.